



Delft University of Technology

Physical and Computational Approaches to Aberration Correction In Fluorescence Microscopy

Wilding, Dean

DOI

[10.4233/uuid:d8f88824-40cc-4358-b7a0-a2d932eb65f5](https://doi.org/10.4233/uuid:d8f88824-40cc-4358-b7a0-a2d932eb65f5)

Publication date

2018

Document Version

Final published version

Citation (APA)

Wilding, D. (2018). *Physical and Computational Approaches to Aberration Correction In Fluorescence Microscopy*. [Dissertation (TU Delft), Delft University of Technology]. <https://doi.org/10.4233/uuid:d8f88824-40cc-4358-b7a0-a2d932eb65f5>

Important note

To cite this publication, please use the final published version (if applicable). Please check the document version above.

Copyright

Other than for strictly personal use, it is not permitted to download, forward or distribute the text or part of it, without the consent of the author(s) and/or copyright holder(s), unless the work is under an open content license such as Creative Commons.

Takedown policy

Please contact us and provide details if you believe this document breaches copyrights. We will remove access to the work immediately and investigate your claim.

Physical and Computational Approaches to Aberration Correction In Fluorescence Microscopy



Physical and Computational Approaches to Aberration Correction In Fluorescence Microscopy

Proefschrift

ter verkrijging van de graad van doctor
aan de Technische Universiteit Delft,
op gezag van de Rector Magnificus Prof. Dr. Ir. T.H.J.J. van der Hagen,
voorzitter van het College voor Promoties,
in het openbaar te verdedigen op woensdag 12 september 2018 om 12:30 uur

door

Dean WILDING

Master of Research,
Imperial College London, Londen, Verenigd Koninkrijk,
geboren te Wigan, Verenigd Koninkrijk.

Dit proefschrift is goedgekeurd door de promotoren.

Samenstelling promotiecommissie bestaat uit:

Rector Magnificus,	voorzitter
Prof. Dr. M. Verhaegen,	Technische Universiteit Delft, promotor
Dr. Ing. R. Van de Plas,	Technische Universiteit Delft, copromotor

Onafhankelijke leden:

Prof. Dr. B. Rieger,	Technische Universiteit Delft
Prof. Dr. M. Booth,	University of Oxford, Verenigd Koninkrijk
Prof. Dr. H.C. Gerritsen,	Utrecht Universiteit
Prof. Dr. G.V. Vdovin,	Technische Universiteit Delft, reservelid
Dr. E.C.M. Carroll,	Technische Universiteit Delft



European Research Council
Established by the European Commission

Keywords: adaptive optics, microscopy, deconvolution

Printed by: Gildeprint Drukkerijen, NL

Front: A colour-encoded three-dimensional image of the blood vessels in a zebrafish produced in the course of this research.

Back: The Siemens test star.

Copyright © 2018 by D. Wilding

ISBN 978-94-6233-996-5

An electronic version of this dissertation is available at
<http://repository.tudelft.nl/>.

*Science is like unrequited love,
most of the time she makes you miserable,
but all she has to do is look once in your direction,
and you fall in love all over again.*

Paolo Pozzi



Acknowledgements

Finally, the end of the road. A PhD is a journey that at times you do not really see going by until you look back at the things that have happened: I have moved three times, I have gotten married, I have become a father, I have been on more aeroplanes than I would like to count, I have spoken at numerous conferences, I have seen new places and many more faces, I have been overjoyed, I have been frustrated, and there has not been too many dull moments.

Naturally, I have many people to give thanks to and for. Firstly, to my promotor, copromotor and supervisors: Michel, Raf, Gleb and Oleg. Thank you for placing your trust in me to work for you and I am thankful for the input, guidance and encouragement throughout this time. Next, I would also like to thank my family, especially, my wife Tamar for her near constant encouragement and gentle mocking. Our parents, Mike & Gill and Herman & Gèrita, for always having open home for us. To the rest of the Wilding family and Het Wilde Gezin and I am thankful for times with you of rest and fun. I also want to thank our wider Christian family for their love and support throughout this time. Especially, those who have been involved with our adventure with the church plant Redeemer Delft and whose love and prayers have helped us through.

To my colleagues who have walked this road with me too I want to thank you for being on this journey with me. I have really appreciated the group of people that have been with me day in and day out, I have found the DCSC a great environment to work in and everyone past and present had a part to play in that.

I have a few special thanks to give. Firstly to Paolo, who introduced me to sim-racing, *real* pasta, new levels of stupidity, road trips and an extremely efficient way of storing headphones. I am thankful for the time we have spent together and the company on those longer trips (Tamar is still jealous!). Secondly, to Hans, who showed me I was an amateur at watching Netflix, gave me a place to live which really helped us save for the wedding. Thirdly, to the rest of the "*Burning Owl Society*": to Elisabeth for being genuine, authentic and kind (and helping me choose an engagement ring for Tamar); to Reinier for being "uncool" and unashamed (and for polishing the translation in this thesis); to Pieter (said: Peter) for forcing me to constantly re-evaluate the depths of the depravity of man, *i.e.* making me laugh; and to Peter (said: *Pæter*) for his deep witticisms. To my first office mate Hai and Tijmen for making me feel welcome right at the start.

To the Master's students whose labour has profited our work: Gijs, Guillermo (only me and his grandmother calls him this), Barbara (said: Barba-*roo*), Abhimanyu & Iurie (with an *I* not a *!*). To those colleagues that have left for greener pastures: Sachin, Subu, Edwin, Bart, Hilko, Chengpu, Yasin, Nico & Vishal. To all those who are still

here: Laurens, Baptiste, Tope, Thao, Shrinivas and the rest I may have forgotten in this moment.

There are so many others that this would not have been possible without: Will and Kees for helping make my ideas into reality, the DCSC secretariat of Marieke, Heleen, Kiran and formerly Kitty; Mascha the Graduate School coordinator, the Coffeestar team past and present; the logistics point; people from ImPhys; the valorisation centre; and M. Schaaf from Leiden University for providing me with the samples I have used in my publications.

Finally, the whole of the work in this thesis has been funded through the European Research Council (ERC) through the ICON project of whom I have been a participant. I guess the final thing to say is to give thanks to the people of Europe for funding my research, I hope I have given something back.

*Dean Wilding
Delft, September 2018*

Summary

The goal of this thesis, called *Physical and Computational Approaches to Aberration Correction In Fluorescence Microscopy*, concerns itself with the development of new techniques to control adaptive fluorescence microscopes, so that they can adapt and image with increased resolution, contrast and speed inside complex three-dimensional biological samples.

The fluorescence microscope is currently one of the most important tool for the investigation of biological functions. This is due to the fact that it is non-invasive and most biological processes happen on a spatio-temporal scale that is nicely balanced with the resolution and speed of optical microscopes. Furthermore, in our current era, due to advances in genetic engineering there is now the possibility of investigating biology *in vivo* through the fluorescent labelling and imaging of cellular processes on the whole organism level.

Whilst there is great potential in these techniques to increase human understanding of disease and biology, the optical tools for the investigation of processes inside and behind biological tissue are still very much in development. It is not possible to see into most biological tissues further than approximately a hundred microns using visible light. The reason for this is that biological tissues essentially have an inhomogeneous composition, which means that when light travels through them, it is deflected in an unpredictable way from the path it would have taken in empty space. These deviations are called *phase aberrations* and when this light is collected and imaged onto a sensor, a blurred image is acquired.

Adaptive optical elements are optical components that can change their shape to allow compensation of these aberrations. Over the last three decades, the development of such elements for laboratory use has made it possible to incorporate them in fluorescence microscopes. Whilst these elements alone cannot correct for aberrations, when they are connected to a suitable control system they can increase the signal-to-noise ratio, resolution and contrast of the acquired images. This is only possible, however, if the system is able to sense the particular aberration, a non-trivial task in fluorescence microscopy.

Every biological sample is different. Furthermore, every position in that sample will affect the light propagation to the sensor in a unique way. To truly see in and through the tissue, it would be necessary to compute the unique correction for every point in the image. This is something that with the current techniques and technology takes far longer than is practically viable and therefore, compromises must be made to balance the time taken with the quality of the correction. Generally, as will be considered in this thesis, one assumes there is one correction for the whole field-of-view.

In this thesis, the modality of fluorescence microscopy that has been focused on is

light-sheet fluorescence microscopy (LSFM). LSFM is a relatively recently developed three-dimensional imaging technique that is commonly used to image larger microscopic samples such as embryos, whole tissues or organs at high speeds. It works by orthogonal excitation and detection of fluorescence to give optically sectioned wide-field images. Since three-dimensional biological samples always have aberrations, many techniques have been developed in LSFM to circumvent the problem of aberrations without actually correcting them. Furthermore, LSFM's system design also causes degradation in the quality of the images that could be produced. The resolution and signal level over the field-of-view are non-uniform due to the shape of the excitation light.

The thesis begins by looking at redesigning the illumination system in a LSFM and looking at how it can be improved by adaptive element in the absence of a sample. A liquid crystal spatial light modulator was included in the optical path and used to shape the incident light to compensate for the non-uniformity of Gaussian illumination through the design and application of optimised binary pupil filters. These binary filters give rise to a real pupil function and as a result give axially symmetric depth-of-field extension. The result of an enhanced depth-of-field in excitation gives rise to a wider field-of-view in detection due to the orthogonality of the optical paths.

The quality of the illumination in this system is a crucial parameter for the final image quality. The excitation light must travel through the entire sample to illuminate a plane so that the fluorescence from this plane can be detected. If aberrations are present the light-sheet becomes thicker and distorted leading to a misrepresentation of the three-dimensional fluorophore distribution, increased background and loss of contrast. With the system design corrected, the next step in the research was to correct both system and sample-induced aberrations in the illumination path. A Shack-Hartmann wavefront sensor was used for this purpose on the normally discarded epifluorescent light to sense the incident aberration. By applying this correction with the spatial light modulator, it was found to improve the illumination beam and the final three-dimensional image quality.

The next stage of the research was to look at the aberrations present in the detected fluorescence light. The challenge here is that the images acquired by the LSFM are wide-field images. The image sensor records the convolution of the object with the aberration affected point-spread function, both of which are unknown. It was found that the existing adaptive optics techniques did not work particularly effectively in LSFM. The aberration changes across the different depth planes, meaning one correction was not sufficient to give improved three-dimensional images, therefore, it was deemed that a computational approach would be faster and more effective.

It was known, however, that a computational approach alone would not be able to correct aberrations that by their nature remove information from the collected images. Inverse problems such as deconvolution techniques tend to produce non-physical results even if the information about the aberration is well-known because information has been lost in the image. An algorithm for the blind multi-frame deconvolution was designed to extract the aberration by acquiring several images while intentionally perturbing

the point-spread function with an active pupil mask. This technique was found to provide a significant image quality improvement and aberration correction inside three-dimensional samples.



Samenvatting

Het doel van dit proefschrift, *Physical and Computational Approaches to Aberration Correction In Fluorescence Microscopy*, is gericht op de ontwikkeling van nieuwe technieken om adaptieve fluorescentiemicroscopen te besturen, zodat deze zich kunnen aanpassen en beelden kunnen maken met een hogere resolutie, contrast en snelheid binnen complexe drie-dimensionele biologische monsters.

De fluorescentiemicroscopie is momenteel een van de belangrijkste instrumenten voor het onderzoeken van biologische functies. Dit komt door het feit dat de microscopie niet-invasief is en doordat de meeste biologische processen plaatsvinden op een vergelijkbare spatio-temporele schaal die in goede balans staat met de resolutie en werksnelheid van de optische microscopen. Bovendien, in onze huidige tijd en door vooruitgang in gentechnologie is er nu de mogelijkheid om de biologie *in vivo* te onderzoeken via fluoriserende markering en de beeldvorming van cellulaire processen over de gehele strekking van het organisme.

Hoewel er in deze technieken veel potentieel zit om het menselijke begrip van ziekte en biologie te verbeteren, zijn de optische methoden voor het onderzoeken van processen binnenin en achter biologisch weefsel nog steeds sterk in ontwikkeling. Bij nagenoeg alle biologische weefsels is het niet mogelijk om met zichtbaar licht verder dan ongeveer 100 micron te kunnen zien. De reden hiervoor is dat biologische weefsels een inhomogene samenstelling hebben, wat betekent dat wanneer het licht door weefsel gaat er onvoorspelbare afwijkingen ontstaan van het pad dat het licht in lege ruimte zou afleggen. Deze afwijkingen worden *fase-aberraties* genoemd en wanneer dit licht verzameld wordt op een sensor, vormt er een wazig beeld.

Adaptieve optische elementen zijn optische componenten die van vorm kunnen veranderen ter compensatie van deze aberraties. In de afgelopen drie decennia heeft de ontwikkeling van deze elementen voor laboratoriumgebruik het mogelijk gemaakt om ze in fluorescentiemicroscopen op te nemen. Hoewel deze elementen alleen aberraties niet kunnen verwijderen, kunnen ze, wanneer ze verbonden zijn met een geschikt regelsysteem, de signaal-ruisverhouding, resolutie en het contrast van de verkregen beelden vergroten. Dit is echter alleen mogelijk als het systeem de specifieke aberratie kan opvangen, een niet-triviale taak in fluorescentiemicroscopie.

Elke biologisch monster is anders. Bovendien zal elke positie in het monster het pad van het licht naar de sensor op een unieke manier beïnvloeden. Om echt in en door het biologische weefsel te kunnen zien, zou het nodig zijn de unieke correctie voor elk punt in het beeld te berekenen. Dit is iets wat met de huidige technieken en technologie erg lang duurt en daardoor niet praktisch uitvoerbaar is. Daarom moeten er compromissen worden gesloten om tijd en de kwaliteit van de correctie in evenwicht te brengen. Over het algemeen, zal er in dit proefschrift één correctie gebruikt worden voor de gehele *field-of-view*.

In dit proefschrift ligt de focus op *light-sheet* fluorescentie-microscopie (LSFM), een vorm van fluorescentiemicroscopie. LSFM is een relatief recent ontwikkelde driedimensionale beeldvormingstechniek die gewoonlijk wordt gebruikt om grotere microscopische monsters zoals embryo's, volledig biologisch weefsel, of organen bij hoge snelheden af te beelden. Door loodrechte excitatie en detectie van fluorescentie ontstaan optisch gescheiden breedveldbeelden. Aangezien driedimensionale biologische monsters altijd aberraties hebben, zijn er veel technieken ontwikkeld in LSFM om het probleem van aberraties te omzeilen zonder ze daadwerkelijk te corrigeren. Bovendien veroorzaakt het systeemontwerp van LSFM ook een verslechtering in kwaliteit van de beelden die worden geproduceerd. De resolutie en het signaalniveau op het *field-of-view* zijn niet-uniform vanwege de vorm van het excitatielicht.

Het proefschrift begint met het herontwerpen van het verlichtingssysteem in een LSFM en onderzoekt hoe het kan worden verbeterd door een adaptief element in de afwezigheid van een monster. Een vloeibaar-kristal ruimtelijke lichtmodulator werd opgenomen in de optische route en gebruikt om het invallende licht te vormen, en zodoende te compenseren voor de niet-uniformiteit van Gauss-verlichting door het ontwerp en het toepassen van geoptimaliseerde binaire pupilfilters. Deze binaire filters creëren een reële pupilfunctie en geven daardoor een axiaal symmetrische uitbreiding van het *depth-of-field*. Het resultaat van een verbeterde *depth-of-field* door excitatie geeft ruimte voor een breder *field-of-view* bij detectie vanwege de orthogonaliteit van de optische paden.

De kwaliteit van de verlichting in dit systeem is een cruciale parameter voor de uiteindelijke beeldkwaliteit. Het excitatielicht moet door het gehele monster om een vlak te verlichten zodat de fluorescentie van dit vlak kan worden gedetecteerd. Als er aberraties aanwezig zijn, wordt het lichtvlak dikker en vervormd, wat leidt tot een verkeerde weergave van de driedimensionale fluorofoorverdeling, verhoogd achtergrondlicht en verlies van contrast. Nadat het systeemontwerp was gecorrigeerd, was het corrigeren van zowel systeem- als monster-geïnduceerde afwijkingen in het belichtingspad de volgende stap. Hiervoor werd een *Shack-Hartmaan wavefront-sensor* gebruikt op het normaliter ongebruikte epi-fluorescerende licht om de incidentafwijking op te vangen. Door deze correctie toe te passen met de *spatial light modulator*, bleek het de belichtingsbundel en de uiteindelijke driedimensionale beeldkwaliteit te verbeteren.

In de volgende fase van het onderzoek werd er gekeken naar de aberraties aanwezig in het gedetecteerde fluorescentielicht. De uitdaging hierbij is dat de beelden verkregen door de LSFM breedveldbeelden zijn. De beeldsensor registreert de convolutie van het object met de door aberratie beïnvloede punt-spreidingsfunctie, welke beide niet bekend zijn. Het bleek dat de bestaande adaptieve optische technieken niet bijzonder effectief werkten bij LSFM. De aberratie verandert in de verschillende dieptevlakken, wat betekende dat één correctie niet voldoende was om verbeterde driedimensionale beelden te creëren. Daarom werd aangenomen dat een computationele benadering sneller en effectiever zou zijn.

Het was echter bekend dat alleen een computationele benadering niet genoeg zou zijn om aberraties, die door hun aard informatie uit de verzamelde beelden verwijderden,

te corrigeren. Inverse problemen zoals deconvolutietechnieken hebben de neiging om niet-fysieke resultaten te produceren, zelfs als de informatie over de aberratie bekend is door informatie die verloren is gegaan in het beeld. Een algoritme voor de *blind multi-frame deconvolution* is ontworpen om de aberratie te extraheren door verschillende afbeeldingen te verwerven, terwijl de punt-spreidingsfunctie opzettelijk wordt verstoord met een actief pupilmasker. Deze techniek blijkt een significante verbetering van de beeldkwaliteit en aberratiecorrectie binnen driedimensionele monsters te geven.



Contents

Acknowledgements	vii
Summary	ix
Samenvatting	xiii
1 Introduction	1
1.1 The Wave Theory of Light	2
1.2 The Imaging Equation	4
1.3 The Generalised Pupil Function (GPF).	5
1.4 Wavefronts & Phase	6
1.5 The Effect of Wavefront Aberrations	8
1.6 Microscopy	10
1.6.1 Wide-field Fluorescence Microscopy (WFFM)	11
1.6.2 Scanning Microscopy (SM)	11
1.6.3 Light Sheet Fluorescence Microscopy (LSFM)	13
1.7 Adaptive Optics in Microscopy	14
1.7.1 Introduction	14
1.7.2 Key Considerations.	17
1.7.3 The Source of Aberrations in Microscopy	17
1.7.4 Wavefront Sensing	20
1.7.5 Controllers	26
1.8 The Motivation & Outline of this Thesis.	32
1.8.1 Motivation	32
1.8.2 Outline	33
References	35
2 Shaping the Illumination	43
2.1 Introduction.	44
2.2 Binary pupil filters	44
2.3 Optimising the filters	45
2.4 Numerical simulation and experimental results.	47
2.5 Discussion.	50
References	52
3 Correcting the Illumination	55
3.1 Introduction	56
3.2 Methodology for Feedforward Control	57
3.3 Experimental Design and Calibration	60

3.4	Biological Imaging Results	62
3.5	Discussion.	65
	References	66
4	Correcting the Image	69
	Part One	69
4.1	Introduction.	70
4.2	Blind multi-frame (or multi-channel) deconvolution	71
4.3	TIP algorithm.	74
4.4	Experiments.	75
	4.4.1 Object and PSF reconstruction	77
	4.4.2 Image types.	77
	4.4.3 Empirical convergence	78
	4.4.4 Algorithm comparisons.	79
4.5	Discussion.	85
	References	89
5	Correcting the Image	93
	Part Two	93
5.1	Introduction.	94
5.2	Methodology for Aberration Correction	95
5.3	Experimental Design	98
5.4	Imaging Results.	99
5.5	Discussion.	102
	References	103
6	Conclusions & Future Outlook	105
	References	108
	Curriculum Vitæ	109
	List of Publications	111

1

Introduction

Please bear in mind that my observations and thoughts are the outcome of my own unaided impulse and curiosity alone; for, besides myself, in our town [Delft] there be no philosophers who practice this art, so pray, take not amiss my poor pen and the liberty I here take in setting down my random notions.

Antonie van Leeuwenhoek

Chapter Abstract

Humans have been making images of their environment for millennia and whilst we have gotten better at it, the same underlying principle remains: imaging is the process of making a recording of a specific object's spatio-temporal distribution. This chapter lays the foundations of the theory of optical imaging and the sources of the distortions that reduce our ability to make faithful recordings of what we are looking at.

Specifically, we shall look at microscopy and the difficulties involved in making images of biological specimens. The main challenge addressed by this thesis are “aberrations” that degrade the quality of these images. A set of techniques known as adaptive optics will be presented as a solution to these aberrations. An overview of the state-of-the-art showing how adaptive optics has been implemented in microscopy will be given along with the outstanding challenges and research questions.

This chapter is an extended version of what has been published in *Practical guidelines for implementing adaptive optics in fluorescence microscopy*, Proc. of SPIE 10502, Adaptive Optics and Wavefront Control for Biological Systems IV, 105021F (2018) [1]

1.1. The Wave Theory of Light

To understand the phenomenon of optical imaging one first needs to consider the nature of light. Imaging requires considering light as a wave that is most thoroughly described by the laws of electrodynamics first elucidated by Maxwell [2] in the 19th Century. What follows here will only be an outline of the most important principles to provide context and groundwork for the main body of this thesis.

The electromagnetic field is vectorial, but with small enough angles of propagation, a simplification of Maxwell's equations, called *Fourier Optics* [3], is sufficient and in this model of light there is a mathematical field denoted by $\psi(x, y, z, t)$ that has a particular amplitude $A(x, y, z, t)$ and phase $\phi(x, y, z, t)$ at every point in space and time:

$$\psi(x, y, z, t) = A(x, y, z, t)e^{j\phi(x, y, z, t)}. \quad (1.1)$$

These functions are real valued and therefore, the electromagnetic field ψ is represented by a complex number in every position. The electromagnetic field is not currently directly measurable and for comparison must be related to a measurable quantity, *i.e.* the modulus of the field, known as the intensity of the light, where the phase information has been discarded:

$$|\psi(x, y, z, t)|^2 = A(x, y, z, t)^2. \quad (1.2)$$

As the electromagnetic field oscillates on the timescale of femtoseconds (10^{-15} s) its temporal component with the current hardware available has a non-observable effect. The time component t , therefore, is ignored and one uses time-averaged fields.

The propagation of this electromagnetic field through space was studied by Fresnel [3] who proposed that free-space propagation may be regarded as a convolution operation of the field with a function $\rho(x, y)$:

$$\psi(x, y, z = z) = \psi(x, y, z = 0) * \rho(x, y), \quad (1.3)$$

which is called the impulse response function of free-space. Here the movement is from one plane with coordinates (x, y) to a plane at a general distance z . For the wavelength of light λ , the analytical form of the function is given by:

$$\rho(x, y) = \frac{e^{j2\pi\frac{z}{\lambda}}}{j\lambda z} e^{j\pi\frac{x^2+y^2}{\lambda z}}. \quad (1.4)$$

If one was to place other optical components between these planes it would change this response function and in this manner whole optical systems can be described. In imaging, this function is usually referred to as the coherent point-spread function (PSF).

Generally, an imaging system is any optical system that takes the light's intensity distribution in one plane and produces a conjugate version of it in another plane along the optical axis. A conjugate version means that the object and image are interchangeable in space, moving the object to the image plane will produce an image in the

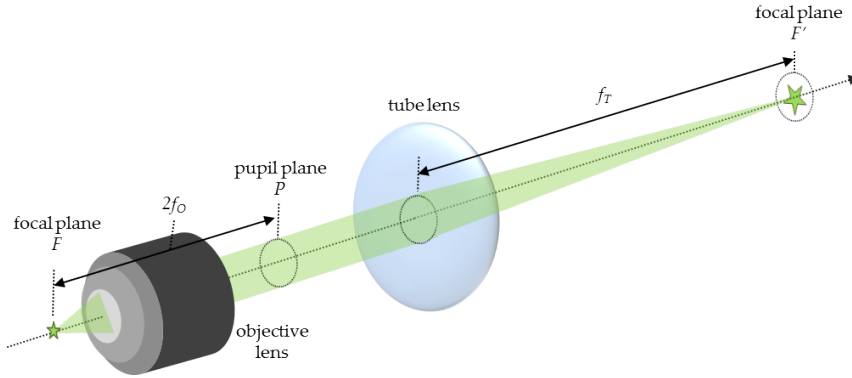


Figure 1.1: A schematic diagram of a microscope showing the three planes of interest. F is the object plane containing the source of light. This light is first collected and collimated by the objective lens. The light travels to P , which is the pupil plane and here a planar wavefront is formed. The light is then focused by the second lens, known as the tube lens, in whose focal plane is the image plane F' .

original object plane — the system is reversible. An example of this is the microscope, which is shown schematically in Fig. 1.1.

As can be seen in the diagram, imaging systems contain lenses and the effect of these can be derived by considering the light propagating through them. Without proof [3], the complex transmittance of a lens with focal length f_o is given by:

$$t_o = c_o e^{-j\pi(x^2+y^2)/\lambda f_o}, \quad (1.5)$$

where c_o is a constant phase term that has no effect on the intensity distribution. With this stated, if one has a field $\psi_-(x, y)$ before the lens, considering it to be a thin lens of zero thickness, the field after the lens is:

$$\psi_+(x, y) = t_l \psi_-(x, y) = c_o \psi_-(x, y) e^{-j\pi(x^2+y^2)/\lambda f_o}. \quad (1.6)$$

Now, if one lets this light propagate to the back focal plane of the lens, this is P in Fig. 1.1, one obtains the following expression by combining Eq. 1.4 and Eq. 1.6:

$$\psi(v, \nu) = c_o \frac{e^{j2\pi\frac{v^2}{\lambda}}}{j\lambda f_o} \iint_{-\infty}^{\infty} \psi_-(x, y) e^{-j\pi(x^2+y^2)/\lambda f_o} e^{j\pi[(v-x)^2+(\nu-y)^2]/\lambda f_o} dx dy. \quad (1.7)$$

Dropping the static phase terms, the expression may be simplified:

$$\psi(v, \nu) = e^{j\pi(v^2+\nu^2)/\lambda f_o} \iint_{-\infty}^{\infty} \psi_-(x, y) e^{-j2\pi(vx+\nu y)/\lambda f_o} dx dy, \quad (1.8)$$

where one can recognise the definition of the Fourier transform:

$$\psi(v, \nu) = e^{j\pi(v^2+\nu^2)/\lambda f_o} \Psi_-\left(\frac{v}{\lambda f_o}, \frac{\nu}{\lambda f_o}\right), \quad (1.9)$$

with $\Psi_- = \mathcal{F}^{-1}\{\psi_-\}$ and the phase term of a spherical wave within the paraxial (small angle) approximation. A special case of this occurs when one considers the field in the focal plane of the lens. In this case, the spherical phase term vanishes and the field in the back focal plane, or *pupil*, is the scaled Fourier transform of the field in the focal plane.

$$\psi_P(v, \nu) = \Psi_F \left(\frac{v}{\lambda f_O}, \frac{\nu}{\lambda f_O} \right). \quad (1.10)$$

This leads to a way to model the effect of an optical system in a simple and straightforward manner. In Eq. 1.3 the propagation through an optical system, from field in ψ to field out ψ' , is shown as a convolution. It is easier to consider this in the Fourier domain with spatial frequencies (v, ν) , where it becomes a point-wise multiplication:

$$\begin{aligned} \mathcal{P}(v, \nu) &= \mathcal{F}^{-1}\{p(x, y)\}, \\ \psi'(x, y) &= \psi(x, y) * p(x, y), \\ \Psi'(v, \nu) &= \Psi(v, \nu) \cdot \mathcal{P}(v, \nu). \end{aligned} \quad (1.11)$$

These relations give a very important formula that will be used extensively as the foundation for imaging. Ignoring any static phase term, it is:

$$\psi'(x, y) = \mathcal{F} \{ \mathcal{F}^{-1}\{\psi(x, y)\} \cdot \mathcal{P}(v, \nu) \}. \quad (1.12)$$

$\mathcal{P}(v, \nu)$ is the Generalised Pupil Function (GFP) and describes the field in the pupil if there is a δ -function, or point-source, in the focal plane of the imaging system. Let it be known as this point, in Eq. 1.12 that one has taken all the three-dimensional information about the propagation of the light along this optical path and condensed it into the effect a single complex multiplication in this plane. This is always an approximation in real systems, and it is the *isoplanatic* approximation.

Mathematical Conventions In this thesis, the Fourier transforms \mathcal{F} will be used to describe the process of moving from the pupil plane to the focal plane, and inverse Fourier transforms \mathcal{F}^{-1} will be used to describe going from the focal plane to the pupil plane. Uppercase letters, e.g. A , will generally refer to quantities in the frequency domain, whereas lowercase, e.g. a , will refer to the same quantity in the spatial domain.

1.2. The Imaging Equation

Further simplifications are possible if the light is assumed to be incoherent, *i.e.* each point in the image is a linear superposition of contributions from the object without any interference effects. Now, the intensities in the planes may be used and one may write them as:

$$\begin{aligned} o(x, y) &= |\psi(x, y)|^2, \\ i(x, y) &= |\psi'(x, y)|^2 = | \mathcal{F}^{-1} \{ \Psi(v, \nu) \cdot \mathcal{P}(v, \nu) \} |^2. \end{aligned} \quad (1.13)$$

where $o(x, y)$ is the object and $i(x, y)$ is the image distribution. The expression for the image can be simplified further by noting:

$$\begin{aligned} |\Psi(\nu, \nu) \cdot \mathcal{P}(\nu, \nu)|^2 &= |\Psi(\nu, \nu)|^2 |\mathcal{P}(\nu, \nu)|^2, \\ |\psi(x, y) * \rho(x, y)|^2 &= |\rho(x, y)|^2 * |\psi(x, y)|^2, \\ i(x, y) &= |\rho(x, y)|^2 * o(x, y). \end{aligned} \quad (1.14)$$

At this point it is more convenient to introduce a new variable, the incoherent point-spread function $h(x, y)$:

$$h(x, y) = |\rho(x, y)|^2 = |\mathcal{F}\{\mathcal{P}(\nu, \nu)\}|^2, \quad (1.15)$$

with its Fourier transform $H(\nu, \nu)$ known as the Optical Transfer Function (OTF). Giving us the incoherent imaging formulae:

$$\begin{aligned} i(x, y) &= h(x, y) * o(x, y), \\ l(\nu, \nu) &= H(\nu, \nu) \cdot O(\nu, \nu). \end{aligned} \quad (1.16)$$

In all real cases, it should be noted that one's recording of the object is never perfect and is always corrupted by a noise component $w(x, y)$, so that in general dropping the spatial coordinates for clarity as there is no ambiguity in the result:

$$i = h * o + w. \quad (1.17)$$

From this simple equation, everything required for mastery of imaging is given¹. It yields the following thesis: the best representation of the object is given when one's imaging system has a PSF which tends to that of a δ -function:

$$\begin{aligned} h &\rightarrow \delta \\ \Rightarrow i &= \delta * o + w = o + w. \end{aligned} \quad (1.18)$$

In this case, the image would be exactly that of the object only corrupted by the noise of the recording system.

1.3. The Generalised Pupil Function (GPF)

A δ -function PSF is impossible as the GPF would need to be unity over all space, which is clearly an impractical result at best. The GPF from Eq. 1.15, therefore, contains all the information about the quality of the imaging system. It allows the image of a point-source after travelling through the system to be calculated and it allows one to know how close two point-sources can be before they are indistinguishable from one another, called the *resolution* of the system. To understand better, it is helpful to split the GFP into an amplitude term $A(\nu, \nu)$ and a phase term $\phi(\nu, \nu)$:

$$\mathcal{P}(\nu, \nu) = A(\nu, \nu) e^{i\phi(\nu, \nu)}. \quad (1.19)$$

¹As with so many elegant and simple physical formulae the most profound difficulties can arise.

Connecting this to reality one can see that $A(v, \nu)$ defines the physical shape of the aperture in the system. Whereas $\phi(v, \nu)$ gives the delay the light will incur at different points of this aperture. In this case, a system is defined as diffraction-limited only if $\phi(v, \nu) = 0$, *i.e.* it is only affected by the diffraction with the aperture. The resolution of the optical system has many heuristic and mathematical formulations, but the most commonly used metric is known as the Abbe diffraction-limit [2] and the minimum distance r_d for a circular aperture is given by the following formula:

$$r_d = \frac{\lambda}{2NA}, \quad (1.20)$$

where λ is the wavelength of the light and NA is the called the numerical aperture, it is defined as $NA = \eta \sin \alpha$, where α is the half-angle for the marginal ray, that which touches the aperture, through the imaging system and η is the refractive index on the object side. If $\phi(v, \nu)$ is non-zero the system has a *phase aberration* which affects how the light travels from the source to the detector degrading the image, the resolution of the system r now is always poorer than the diffraction-limited case:

$$r > r_d. \quad (1.21)$$

It is useful to note that the approximations of scalar theory are valid up to around a $NA \approx 0.8$. Above this value the vectorial nature of the electromagnetic field needs to be taken into account since the vector of the field can no longer be assumed to be wholly perpendicular to the optical axis.

1.4. Wavefronts & Phase

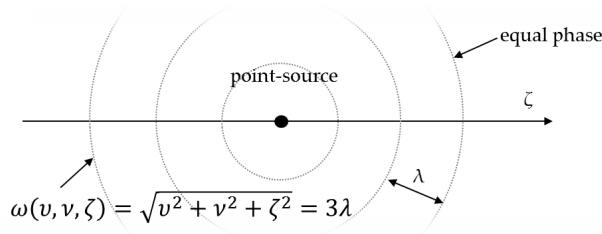


Figure 1.2: A point-source acts as the origin for spherical waves. The positions of equal phase in the field are shown and these are three-dimensional spherical surfaces. The surfaces at $\phi = 0, 2\pi, 4\pi$ & 6π are shown.

The source of aberrations and the phase term $\phi(v, \nu)$ in the GPF will require the introduction of another concept, the *wavefront*. If one imagines a point-source as being the origin of spherical oscillations or *waves* of the electromagnetic field, this can be modelled in scalar wave theory by [3]:

$$\psi_s = \frac{e^{jkr}}{r}, \quad (1.22)$$

where $k = 2\pi/\lambda$ is the wavenumber and $r = \sqrt{v^2 + \nu^2 + \zeta^2}$. A wavefront is defined as positions in this field of equal phase, see Fig. 1.2 for a diagrammatic representation of the concept. These within the quantum picture of light may be regarded as photons that left the source at the same time. The wavefronts in free space for ψ_s , therefore, are spherical in form:

$$\omega(v, \nu, \zeta) = \sqrt{v^2 + \nu^2 + \zeta^2} \quad (1.23)$$

If the refractive index the photons have travelled through is different they will have gone different distances from the source after a certain time t and the wavefront $\omega(v, \nu, \zeta)$ will not longer be spherical.

The phase of the field is dependent both on the spatial position and the point in time, but as mentioned previously the time dependence is usually discarded. The measure of the correlation of phase at different points in the field, both in time and in space, is known as *coherence*. A result of this property of the field is that only light that is coherent in both time and space exhibits interference phenomena.

Normally, in optical systems one likes to consider planes of propagation with the light travelling in the positive z direction. The effect of a lens will be considered and from Eq. 1.10 given the previous assumptions it performs a Fourier transform between the focal plane and pupil plane [3]. This implies that the wavefronts are transformed by a lens from a spherical wave to a plane wave, and the field within the paraxial approximation is:

$$\psi_p = e^{ikz}. \quad (1.24)$$

This has wavefronts that are perpendicular to the optical axis. If there is an imperfection in the lens or a non-uniform region of refractive index variation the wavefront will be deformed. The light is slowed down more in some regions than in others. The result is that the wavefront in the pupil is no longer planar. This can be seen in Fig. 1.3(a) and (b) where a non-uniform refractive index distribution leads to phase delays.

It should be noted that the phase $\phi(v, \nu)$ of the GPF is *not* the same as the wavefront in the pupil. The wavefront is a three dimensional surface of equal phase, whereas, the phase in the pupil is a function of how the phase varies only in one plane. To explain this, imagine a spherical wavefront centered on $\zeta = R$. The wavefront $\omega(v, \nu, \zeta)$ like in Eq. 1.23 is given by:

$$\omega(v, \nu, \zeta) = \sqrt{v^2 + \nu^2 + (\zeta - R)^2}, \quad (1.25)$$

and let us consider the surface of equal phase that touches $v = \nu = \zeta = 0$ as can be seen in Fig. 1.3(c). The phase in this plane is given by distance between the plane and wavefront surface up to some constant piston term ϕ_0 :

$$\phi(v, \nu) = \frac{2\pi}{\lambda} \zeta(v, \nu) + \phi_0, \quad (1.26)$$

where $\zeta(v, \nu)$ is defined by the distance between the wavefront surface and the plane $\zeta = 0$. With a little rearrangement of Eq. 1.25 and Eq. 1.26 it can be seen with

$\omega(v, \nu, \zeta) = R$:

$$\phi(v, \nu) = \frac{2\pi}{\lambda} \left(R - \sqrt{R^2 - v^2 - \nu^2} \right) + \phi_0 \neq \omega(v, \nu, \zeta = 0). \quad (1.27)$$

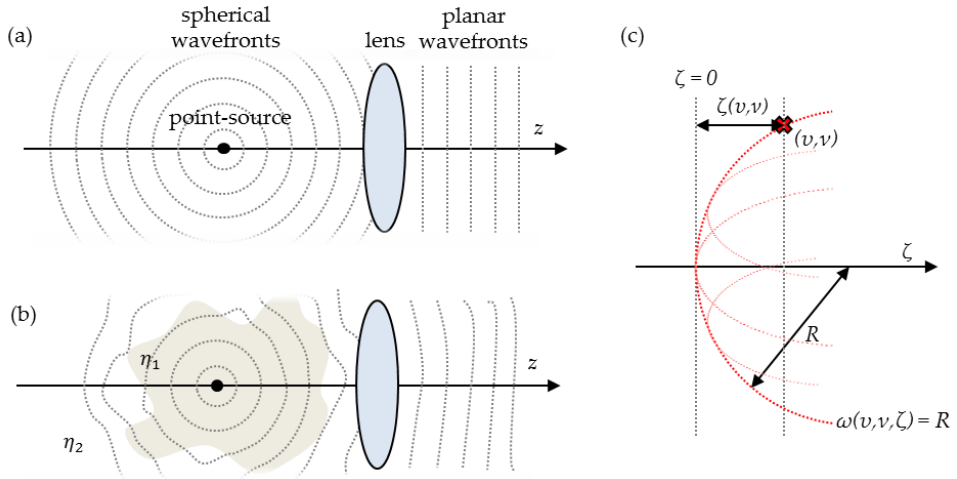


Figure 1.3: This figure shows the effect of changes in refractive index on the wavefront shape. (a) Shows a perfect system where there is no phase aberration. The spherical wavefronts that leave the source are collimated by the lens resulting in plane waves. (b) The spherical wavefronts that start at the point source are distorted by the refractive index changes leading to a non-planar wavefront in the pupil, and the source of the phase term in the GPF. (c) A diagram showing the difference between the wavefront and the phase.

1.5. The Effect of Wavefront Aberrations

If the wavefront in the pupil is non-planar it will have an effect on the systems ability to image. Going back to the imaging formula, Eq. 1.17, and remembering that better images require h to be close to a δ -function, one must now consider what the effect is on h . For a circular aperture of radius R , the effect can be calculated numerically by computing:

$$h(x, y) = \left| \mathcal{F} \left\{ \text{circ}(R) e^{j\phi(v, \nu)} \right\} \right|^2, \quad (1.28)$$

and the value of $h(x, y)$ can be known for a given $\phi(v, \nu)$ distributions. In Fig. 1.4, a comparison between the simulated PSF for a flat wavefront in (a) and a distorted wavefront in (b) is shown.

Qualitatively, the effect is that the PSF becomes larger in size as more of the light is deflected away from the focus. This means that the imaging convolution operation leads to a more blurry image. For demonstration purposes, one can show the effect of an aberration on the formation of images combining Eq.1.17 and Eq. 1.19 with a

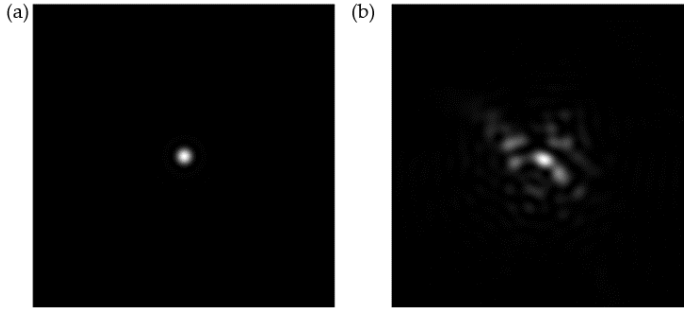


Figure 1.4: Computationally simulated PSFs by Fourier transforming the pupil function of (a) an aberration-free flat wavefront and (b) an aberrated PSF from a distorted wavefront.

horizontal coma aberration, the PSF becomes:

$$h(x, y) = \left| \mathcal{F} \left\{ \text{circ}(R) e^{j \frac{2\pi}{\lambda} \alpha (3\nu^3 + 3\nu^2\nu - 2\nu)} \right\} \right|^2, \quad (1.29)$$

where α is a scaling coefficient. The effect of this on the image is shown in Fig. 1.5.

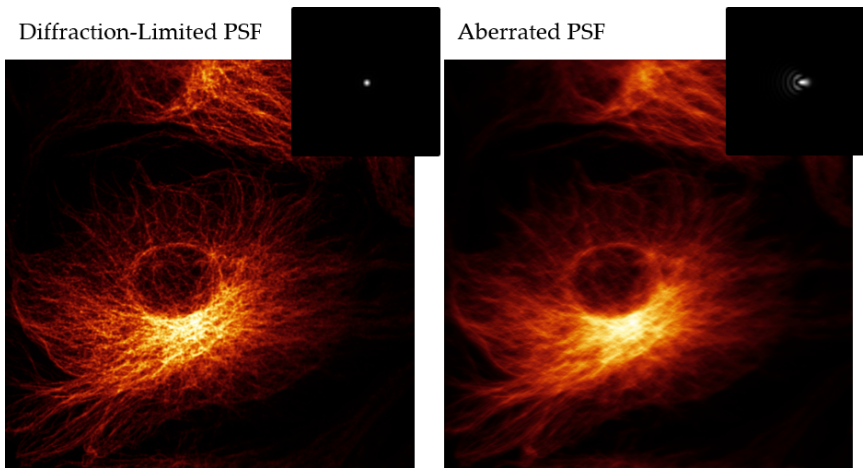


Figure 1.5: A confocal image of fluorescently stained microtubules has been computationally aberrated using the imaging formula Eq. 1.17. The effect of an aberrated PSF (inset) on the formation of images can then be compared with a diffraction-limited case. It is clear from visual comparison that the details and the resolution in the diffraction-limited image are better than with the coma aberration.

Here it can be seen that the introduction of the aberration to the GPF has a consequence on the image formation. The resultant image with the aberration is more blurry than without the coma aberration. The resolution is worse, as there are now features in the aberrated version that are no longer distinguishable when compared with the diffraction-limited version.

1.6. Microscopy

The word *microscopy* is derived from the Greek words *micros* meaning “small” and *skopein* meaning “to see” and refers to a broad and diverse set of methods used to investigate objects that are too small to be resolved with the naked eye. A microscope is an imaging system with a large magnification factor.

There are many different imaging modalities and types of contrast available that fall under this umbrella term. A good definition then is that it applies to any technique that allows the imaging of objects on the scale of micrometres (μm). The first compound microscopes (a schematic in Fig. 1.1) were developed in the 16th century by Dutch spectacle makers Hans & Zacharias Jansen [4]. The use of microscopy, however, to study the “hidden world” was pioneered by Antonie van Leeuwenhoek [5] and Robert Hooke [6] in the subsequent century.

The ability to see small biological objects is in and of itself not that helpful in understanding how they work. It is necessary to have a source of contrast that is specific to what is being studied. For these reasons, of particular interest in the life sciences, such as biology or medicine, is the use of *fluorescence* as a source of contrast.

Fluorescence is a physical effect that certain molecules known as *fluorophores* exhibit. They absorb light at one frequency and then re-emit it a small fraction of time later at a lower frequency. This change in frequency is due to energy loss into the vibrational energy modes of the molecule and the observable result is a change of colour. This effect is known as the *Stokes' shift* [7] and allows the light to be separated with frequency-dependent filters. This allows light from specifically labelled molecules to be seen over a black background.

Originally, it was necessary to use fluorescence dyes [8] that would chemically bond with the molecule or ion of interest, acting as a tag or probe. Advances in genetic research, however, have allowed the development of fluorescent proteins [9], which can be encoded in the genomes of organisms. In this case, the organism itself produces the fluorophore attached to protein of interest. This technique has allowed a revolution in biological imaging. A large amount of work now goes into designing these genetically modified organisms and testing that the function of the organism is not inhibited by the genetic modification.

It should be noted that the previously discussed diffraction-limit was for many years the horizon for optical imaging and the reduction of aberrations in the systems were designed to return the operation to close to the physical limit. This was the case until relatively recently with the development of “super-resolution” techniques such as STED [10], PALM [11] and STORM [12], when it became possible to resolve features smaller than the Abbe limit with fluorescence imaging.

There are different types of fluorescence imaging that have been developed for biology. They can be broadly separated into two categories: the first is *wide-field* fluorescence microscopy and the second is *scanning* fluorescence microscopy.

1.6.1. Wide-field Fluorescence Microscopy (WFFM)

In wide-field fluorescence microscopy the detector used is planar, such as a camera. The optical system is set up such that the microscope follows the principle of Fig. 1.1. Here a conjugate image plane of the object is formed at a magnification given by the ratio of the tube lens to objective lens focal lengths $M = f_T/f_O$.

The main benefits of wide-field microscopy is its simplicity, robustness and parallelism. There are fewer parts involved and this decreases system aberrations and increases reliability. The speed at which one is able to image in wide-field is much faster relative to scanning methods since you image an entire plane at one time. For these reasons it is commonly used to image biological events that occur at high speeds, for example, neuron activity [13].

On the other hand, the downside of wide-field imaging is the absence of sectioning. Light from planes outside of the focus is still able to propagate through the optical system and arrive at the detector. The presence of this light creates an *out-of-focus blur* that increases the background and thus decreases the contrast and clarity of the images formed. Furthermore, when specimen's composition is highly scattering or the imaging depth is large these effects and the effect of aberrations renders the image too low in quality to be of practical use.

1.6.2. Scanning Microscopy (SM)

In this imaging modality the planar detector is replaced with a point detector. The position of detection is then scanned so that a pixel-by-pixel map of the specimen can be made. There are two common methods that are used in imaging today. The first confocal microscopy uses a pin-hole aperture to reject out-of-focus light and second uses two-photon excitation to section the specimen.

The patent for the confocal microscope was originally filed in the 1950s by Marvin Minsky [14, 15], but it was only thirty years later that this technique was incorporated successfully with scanning technique, which has made the method a popular imaging method today [16]. The placement of a pinhole at the point detector means that only light from the focal plane will travel on an optical path that allows it to reach the detector. The rest of the light from out-of-focus planes will hit the aperture and not be detected.

Since the out-of-focus light is *rejected* an increase contrast is gained over wide-field fluorescence microscopy. An additional bonus with confocal microscopy is that it also boosts the resolution of the microscope. The probabilities involving emission and detection are combined in this configuration. The final PSF of the confocal microscope is that of the same system operating in a wide-field modality squared. Thus the resolution with the same objective and tube lenses with no aberrations is $\sqrt{2}$ × better.

A similar principle is used in multi-photon microscopy [17]. It uses the fact that the cross-section² for multi-photon absorption is highly unlikely to occur apart from at high intensities. For example, it is proportional to the intensity squared for two-photon

²A quantum mechanical probability.

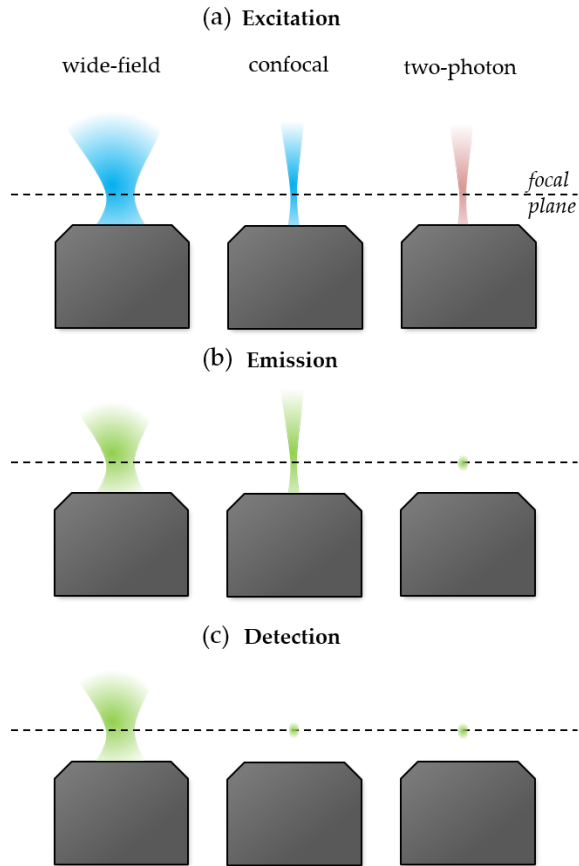


Figure 1.6: (a) The excitation profiles of wide-field, confocal and two-photon microscopes. (b) The emission profile of wide-field, confocal and two-photon microscopes. (c) The detected emission from the wide-field, confocal and two-photon microscopes. The confocal microscope has a pinhole that rejects light from out-of-focus planes, so that all the light that is emitted is not collected by the microscope.

absorption. By using a pulsed infrared laser source, therefore, one is able to generate sufficient laser intensity to cause fluorescence in the visible waveband. This technique has innate sectioning ability due to the excitation of fluorescence only taking place in a very narrow region surrounding the focal position.

The downsides to scanning microscopy are that it is not parallel and requires moving parts. Every position in the image is scanned and recorded separately, therefore, losing the parallelism usually found in image formation. The scanning requires the use of moving parts to deflect the illumination light and fluorescence and therefore, due to inertia there is a physical limit to how fast it is possible to go. Many of the processes of life happen on time-scales that are faster than the refresh rate of a scanning microscope

and therefore, new techniques have been developed to provide sectioning.

The key rationale behind scanning techniques is to reduce the background of the out-of-focus fluorescence so that images with higher contrast can be rendered deep in tissues *in vivo* [18]. The excitation, emission and detection regions are compared visually in Fig. 1.6 for these techniques.

1.6.3. Light Sheet Fluorescence Microscopy (LSFM)

A *light-sheet* microscope, sometimes called the “Ultramicroscope”, is a type of microscope first developed by Siedentopf and Zsigmondy [19] in the early 20th century and involves the formation to two orthogonal optical paths. One path is the illumination which is formed when light is focused using cylindrical rather than spherical optics leading to a large astigmatism in one of the directions generating a two-dimensional sheet of light. Originally, the source of contrast was scattering from objects in the light-sheet or the *dark-field* image. Much later it was shown that if a fluorescent sample is brought into this region of illumination it will absorb the incident photons. These photons will be re-emitted in all directions and if this is viewed looking down into the light-sheet one will be able to see the fluorescence from a two-dimensional plane. The fact that the light is generated in a two-dimensional plane is a powerful tool and the sample can be illuminated in many thin two-dimensional sections to create a three dimensional picture without the need to physically section the sample.

It currently has many names that are used interchangeably such as: Selective Plane Illumination Microscopy (SPIM) [20] or Orthogonal-Plane Fluorescence Optical Sectioning (OPFOS) [21] where a static light-sheet is used. Alternatively, when a beam is scanned rapidly in one direction it is sometimes called Digital Scanned Light-sheet fluorescence Microscopy (DSLM). All these are actually forms of light-sheet fluorescence microscopy (LSFM) and throughout this thesis, this term will be used.

The schematic of the setup is found in Fig. 1.7, a cylindrical beam is focused or a Gaussian beam is scanned through the focal plane of a second objective lens that is used for imaging fluorescence. The disadvantages of this technique are the geometrical constraints found in objective lenses and the necessity for non-conventional sample preparation techniques. This ends up limiting the NA of the lenses that can be used, meaning that LSFM generally has a lower maximum resolution than other confocal or multi-photon techniques. There have been methods developed to provide epi-illuminated LSFM [22–24] and therefore, restore conventional sample preparation techniques again by decreasing the NA of the objective lens.

In summary, LSFM may be considered as the hybridisation between the confocal scanning systems and wide-field. It combines the benefits of wide-field microscopy with those of a scanning system. It provides high-speed optically sectioned images, however, this comes at a cost of more difficult sample mounting and preparation techniques and a lower overall NA. With this combination of sectioning and speed, it is possible to image whole tissues at high-speed in order to study their temporal behaviour [25, 26].

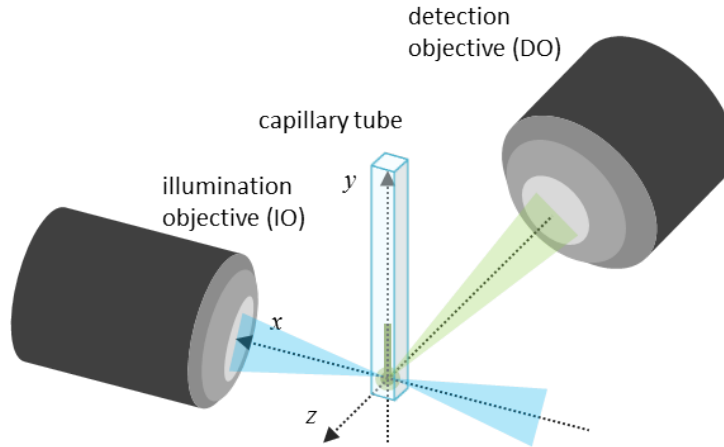


Figure 1.7: The configuration for light-sheet fluorescence microscopy (LSFM). The standard microscope design is modified by use of a cylindrical beam or scanner that illuminates the focal plane of the detection objective lens (DO) through an illumination objective (IO).

1.7. Adaptive Optics in Microscopy

1.7.1. Introduction

Adaptive optics was first developed to correct for aberrations introduced by the atmosphere in the context of astronomy and defence [27], however, its cost was prohibitively expensive for use in normal laboratory settings, for example, where it could be employed in microscopy. Research started in the last few years of the 1990s with the advent of low-cost adaptive optical elements [28–30] and the theoretical development of ideas around the validity of adaptive optics for aberration correction in microscopy [31, 32].

One of the first implementations in microscopy appears in the tip-tilt correction that is found in the work of O’Byrne et al. [33]. Here correction to the tip and tilt of the wavefront is done using mirrors in confocal microscope rather than the introduction of another element. The use of this methodology is to reduce the image shifts that occur when scanning over the field-of-view. This method is still to be preferred over using another adaptive element such as a deformable mirror (DM) or a spatial light modulator (SLM) in the path to reduce the coupling of the aberration modes, which may not be translation free [34].

Likewise other implementations at this time all centred around the use of AO in confocal microscopy [35]. Both in the standard epi-confocal microscope [36] and in a transmission setup [37] and both of which were working with what are called focal-plane sensors. This is where the signal from the usual imaging sensor is used to feedback to the actuators of the adaptive optical element (AOE) often through the formation of a *image metric*. An image metric is a method of quantifying how close the system is to an aberration-free state, the idea is to maximise the metric and the aberrations will be removed.

To increase this metric an optimisation algorithm is employed. For example, the microscope designed by Albert et al. [37] used a genetic algorithm [38] to optimise the signal from the device and by increasing the signal one assumed to have removed the aberrations in the system due to the nature of the confocal pinhole rejection.

In the same year, Neil [39] suggested a new form of wavefront sensing that would allow the separation of individual Zernike modes within the sample [40, 41]. This modal-based sensor allowed the different modes to be corrected using a AOE efficiently and without optimisation. The downsides to this approach is that it requires removing photons from detection and this is undesirable in fluorescence microscopy where photons are limited. This theoretical sensor was then applied in an experimental multi-photon system and shown to improve the imaging capabilities of microscope [42].

Alongside this was the development of new computational techniques that could improve the quality of the images formed. In 2001, Kam et al. [43] approached the problem of aberration correction in a microscope by using ray tracing to calculate the 3D point-spread function (PSF) of the microscope and use this to deconvolve the images that they were recording. The drawbacks of this technique is the process of deconvolution at this time was a lengthy one and therefore, it was not ideal for biological imaging where knowledge of the quality of the image is wanted in real-time.

The following year Sherman et al. [44] continuing on from the work of the previous paper [37] produced a focal-plane sensing multi-photon system again using a genetic algorithm to optimise the signal.

Further analysis and extension of the modal sensor from Neil allowed in principle the expansion of this modal wave sensing to confocal microscopy [45, 46]. This technique seems, however, never transitioned from concept to reality. It is likely that the difficulty of practically creating this adaptive optics system in a confocal microscope proved to be technologically out of reach and the movement of the scientific community towards focal-plane sensing cemented.

Later in 2003, a focal-plane method using an image metric was applied to a multi-photon system [47]. Here the image metric was maximized by using a hill-climbing algorithm. The time of optimisation, however, was still too long for what is practically usable in biological imaging.

Theoretical work continued with Wright et al. [48] and Booth [49] providing an analysis of the algorithms that were being used to optimise the image metrics. The theoretical development surrounding focal-plane sensing adaptive optics showed that there are approximations that can be made to improve the convergence and speed of the optimisation problems. Booth investigated the signal that is measured in confocal microscopy, i.e. the point-source detection. The Strehl ratio, intensity of an aberrated to unaberrated PSF, was then used as a metric for the optimisation of the signal but was only valid for small aberrations.

A new approach was found in 2006 when Rueckel et al. developed a coherence-gated technique [50]. This approach involves the use of interferometry as a sensor in the pupil-plane. The sensor in this case does not use the fluorescent light that is

being imaged from the sample. Instead the back-scattered laser light is used to gather information about the aberrations that the sample was inducing. By using a pulsed laser source it was possible to provide gates of coherence that allowed only the light from the same wave-packets to interact and interfere. Whilst there is a background signal from other wave-packets only the matched wave-packet produces an interference pattern that can be decoded to find information about the optical path of the different photons.

Later Booth further developed his theory to involve the correction of larger aberrations that had been missing from his previous analysis [51]. This approach used an extension of the Zernike modal method of studying aberrations to include the Lukosz-Zernike polynomials [52, 53] that have the benefit of having the same properties as the Strehl ratio metric.

In 2007, Kam et al. [54] modelled the applicability of applying adaptive techniques to wide-field microscopy. Wide-field fluorescence microscopy is widely used in biological laboratories because it provides a fast, easy and cost effective form of imaging. It does not have the complexity and unreliability of using a more advanced microscope. It would be ideal, therefore, if adaptive optics could improve the images from wide-field systems too. This technique of wide-field adaptive correction was applied later to an experimental system in 2010 by Kner et al. [55].

In the work of Débarre et al. [56], they showed that using a new optimisation scheme they were able to demonstrate much faster adaptive imaging using a two-photon microscope. This involved finding N modes of the system such that the cross-talk between the correction modes was minimised. The choice of correction modes were mathematically orthogonalised via a calibration procedure. This technique allowed for the use of a quadratic maximisation routine, where the maximum could be found quickly and efficiently using $2N + 1$ measurements by fitting a quadratic curve for each mode.

In 2009, Ji et al. [57] developed a new method for improving the imaging capabilities of a two-photon microscope. Here the pupil was segmented using a SLM and sequentially the elements of pupil are turned on and off. Any aberrations through this part of the pupil can then be recovered and corrected using the adaptive optical element. This technique remains in the domain of focal-plane sensing adaptive optics as no extra sensor has been used to obtain the wavefront.

A method for microscopy using a pupil-plane sensor was developed by Cha et al. [58]. The approach here was to use the back-scattered light from the sample and image this light onto a Shack-Hartmann sensor using a confocal pinhole as a filter. This pinhole allows only the light from the focal plane of the lens and therefore, the area being imaged to be sensed by the wavefront sensor. Later Shaw et al. [59] gave a theoretical description of how a confocal wavefront sensor may be used optimally.

From here the focus of the literature centres around optimising model-based focal-plane sensing and optimisation. In 2010, Song et al. [60] presented a model-based method for improving the speed of focal-plane sensing adaptive optics. The next year a helpful paper by Thayil et al. [34] provided an explanation of how it is possible to

calibrate such systems in the vein of Booth and Débarre.

In 2011, both Azucena [61] for wide-field and Tao et al. [62] for confocal used the Shack-Hartmann sensor as a pupil-plane sensing scheme in microscopy. In each of these cases the methodology is similar whilst the microscope is different. In each case the introduction of embedded guide beacons or guide stars is used. These take the form of fluorescent beads and emit on a different waveband to the fluorescence from the sample. In this case, the sensing is done at one wavelength and the imaging at another.

In the last few years, work in improving the optimisation of focal-plane based techniques was done by Antonello et al. [63, 64] and showed how convex optimisation techniques can be applied to the problem of calculating and correcting the wavefront error. Furthermore, the application of adaptive optics in different microscopy modalities started to increase and be used outside of the traditional confocal and multi-photon setups such as in light-sheet fluorescence microscopy (LSFM) [65] and stimulated emission depletion (STED) microscopes [66].

1.7.2. Key Considerations

An overview of the *state-of-the-art* up to the point the work on this thesis began has been provided in the previous section. Not every publication, however, involved in applying adaptive optics in fluorescence microscopy has been described. From here, the key methods involved in the application of adaptive optics for fluorescence microscopy will be given.

Given the scope of ‘fluorescence microscopy’ it will not be possible to go into all the details of how this may be achieved in every modality, but a helpful outline of the principles for the major groups of scanning (see 1.6.2) and wide-field (see 1.6.1) microscopes will be attempted. The light-sheet fluorescence microscope [20, 21], which this thesis has been mainly been concerned with, will be treated as a form of wide-field microscope.

It will be first explained what the source of aberrations is and their effect in fluorescence microscopy. After which the three parts of an adaptive optics system will be discussed: the first is the *wavefront sensor*, the second is the *corrector* and the final piece of the puzzle to understand is the *controller*.

1.7.3. The Source of Aberrations in Microscopy

The source of aberrations in fluorescence microscopy is the inhomogeneous distribution of refractive index in biological tissues — if the system aberrations are neglected. Since it was understood from the beginning of microscopy that one could not look inside biological tissues very easily, solutions had to be devised. The original approach to this was to use a microtome to cut the sample into thin quasi two-dimensional slices and build up a three-dimensional picture by stacking these images together.

It is obviously, not the most helpful approach if one wants to understand biology whilst it is alive, therefore, more innovation was necessary and with the advent of fluorescence microscopy, a new approach could be used. Fluorescence light is only emitted

from areas that are illuminated and this occurs with an intensity that is proportional to the strength of that illumination. If one illuminates only the area that one wishes to image, *i.e.* a two-dimensional plane then one gets an *optically* sectioned image. Optical sectioning is widely employed and may be found in confocal [16], two-photon [17] and light-sheet fluorescence microscopy. It is a highly successful approach and gives a much better signal-to-noise ratio, contrast and image quality than without sectioning.

The problem with using optical sectioning is the light used for sectioning is affected by the very same inhomogeneity that plagues the signal one is trying to acquire. This means the image acquired is doubly affected: the section illuminated is not the assumed section and this emitted light is then affected by its own propagation through the specimen.

In Fig. 1.8 a schematic of the effect is shown for a light-sheet modality. The light enters from the left and is aberrated as it travels through the specimen. This results in the fluorescence emission from out-of-focus planes, but also the uniformity of the illumination over the plane is ruined. The image is reduced in contrast and the observed fluorophore distribution is not faithful to the actual distribution inside the specimen.

Unlike the light-sheet microscope, in many microscopes the excitation and the illumination pass through the same aberration and therefore, a single adaptive optical element (AOE) can be used for *isoplanatic* correction, *i.e.* in a single point of the field-of-view (FOV). In other microscopy systems, a correction is required for the illumination and fluorescence independently meaning two AOE's are necessary.

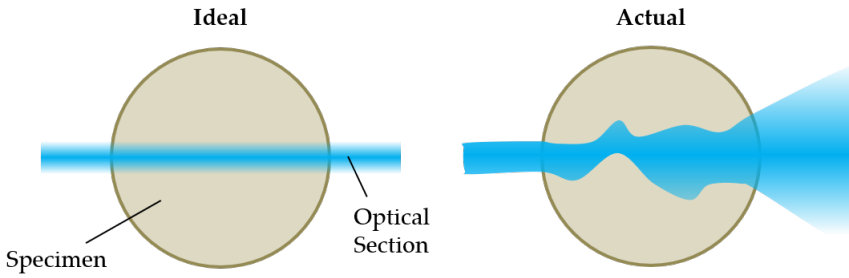
A second challenging point for consideration is shown schematically in Fig. 1.9. Here the light from two points in the specimen is shown travelling from the source fluorophore to the microscope objective. This light travels through two distinct optical paths and acquires two different phase aberrations. These would need two different corrections to be applied to the AOE in order to correct them perfectly. The aberrations in microscopy are *anisoplanatic*, meaning that a different correction for different areas of the FOV is necessary.

The normal approach in AO for microscopy has been taken from astronomy and it is to place a corrective element in the pupil plane. This is the plane where all the light from the different sources in the focal plane overlap. Here it is possible to find an average or global *isoplanatic* correction that will improve the overall image quality regardless of the *anisoplanatic* nature of the aberrations. Complete correction, however, for all areas of the FOV cannot be done with a single element in the pupil plane.

Nevertheless, considering the standard approach, if one applies a correction in the pupil-plane it will result in some areas of the image improving and some areas degrading (depending on the particular aberration). For the reasons of universal effect most adaptive optics systems work by having their corrector and sensor in this pupil-plane — it is a good compromise.

The crucial point of understanding is that the correction required in biological samples is three-dimensional because the aberration is three-dimensional. It is impossible

(a) Excitation



(b) Detection

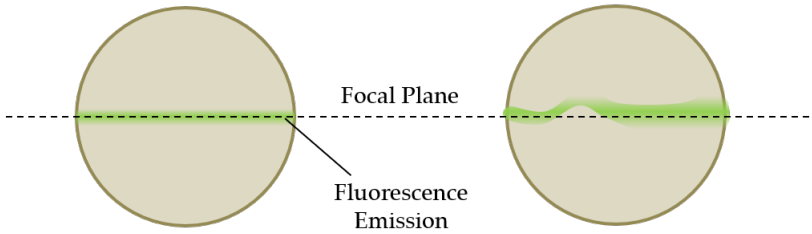


Figure 1.8: A comparison between what the effect of aberrations is on optical sectioning. (a) in the ideal or assumed case a quasi-two-dimensional plane is illuminated and all the light collected at the sensor comes from this thin section of the specimen. (b) a more realistic case inside a three-dimensional sample, the excitation light is affected by the aberrations and does not form a two-dimensional plane. The light collected at the sensor in this case is not a true representation of the fluorophores in this plane but has been corrupted by out-of-focus light and non-uniform illumination profile.

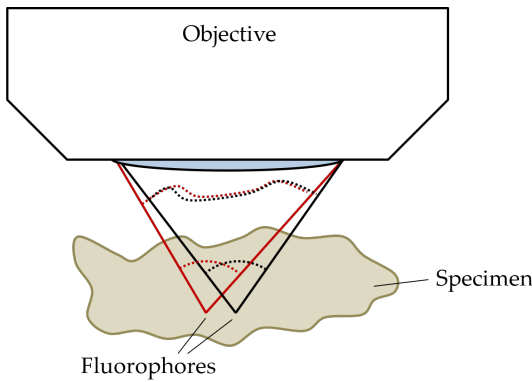


Figure 1.9: The source of aberrations in fluorescence microscopy comes from the inhomogeneous refractive index of biological tissues. Light from two different sources in the sample will travel through two different optical path lengths and thereby acquiring different phase delays.

with a single plane corrector to achieve correction throughout the sample in one shot. For the purpose of extending the correction, multi-conjugate systems are being developed to provide a correction that more closely approximates the phase aberration present [67–69]. Nevertheless, this thesis will work with a two-dimensional corrector in the pupil-plane of an optical system and many things can still be done to improve the imaging quality.

1.7.4. Wavefront Sensing

It should be clear from the literature survey that there are two types of wavefront sensing that can be chosen: one in the pupil and one in the focal-plane of the system. In the majority of cases the choice will be determined by both one's available hardware budget and the modality of the microscope. Focal-plane sensing is more common in fluorescence microscopy since this do not require the loss of signal-levels in imaging, however, it is possible to apply pupil-plane sensors to fluorescence microscopy if one has the right budget, application and will-power.

The big difference between the two is that a focal-plane sensor uses the data directly from the imaging sensor, i.e. a scientific camera, photo-diode, etc. and only requires the addition of the corrector in the setup. Whereas, the pupil-plane sensor such as the Shack-Hartmann sensor [70] works by using a lenslet array in a secondary optical path and measures the displacement of an array of focal spots. The Shack-Hartmann is the only pupil-plane sensor that shall be treated in detail in this chapter, however, others exist such as the Partitioned Aperture Wavefront (PAW) sensor [71], the pyramid sensor [72], and interferometry can also be used [50] to sense the aberration.

The Pupil-Plane Wavefront Sensor

The pupil-plane wavefront sensor (PP-WFS), specifically here the Shack-Hartmann sensor, requires loss of photons or the use of a second fluorophore at a different wavelength. It also requires the use of point-sources, in microscopy this implies the introduction of non-biological guides in the form of beads to act as localised sources of aberration information [62]. The downside of this is obviously the introduction of a foreign agent is going to activate an immune response *in vivo* and may effect the biology of what is being studied.

The PP-WFS configuration is shown in Fig. 1.10 and as can be observed it is practically more difficult to implement than the FP-WFS c.f. Fig. 1.11 as one must split the light by the beam-splitter (BS) shown in Fig. 1.10. For standard operation, the PP-WFS must be conjugated to the corrector and the pupil-plane of the objective giving a linear relationship between the corrector inputs and the measured phase. (The procedure for this will be described in the subsequent Section 1.7.4.) The ratio of the beam splitter must be chosen to ensure the correct amount of light for imaging and for wavefront sensing if using one wavelength. The lenslet array (LA) pitch p (the distance between lenses) and its focal length (f_A) affect the resolution and the amplitude of the phase aberration that the sensor can detect. It is necessary to have an approximate estimate of what is required before purchasing one of these. As a guide, the maximum

phase gradient that can be measured by a particular Shack-Hartmann is given by:

$$\langle \nabla \phi \rangle_{\max} \approx \frac{\pi \rho^2}{2\lambda f_A}. \quad (1.30)$$

where $\langle \cdot \rangle$ is the mean over the lenslet area and λ is the wavelength of light. From this equation, it can be deduced that the larger the value of f_A the smaller the displacement for the same phase gradient. It must also be considered that the pitch defines the sampling resolution of the pupil. In this case, a large pitch with a short focal length allows the measurement of large low order aberrations. From a pure adaptive optics perspective, unless the entire system is designed *ad hoc*, the rule-of-thumb in the selection of a sensor is using a number of sub-apertures equal to around three times the number of corrector actuators. Additional factors, however, must be considered based on the nature of aberrations one expects. A small pitch with large focal length allows the measurement of smaller high order aberrations. Moreover, the signal from the point source is split between sub-apertures, so the more lenslets the less light per sub-aperture, therefore, the signal-to-noise ratio is lower and the computational complexity increases, both of which are counter-productive.

Another important metric is the dynamic range of the total lenslet array and this can be computed for a given aberration. For example, the total defocus stroke $\Delta\lambda_{\text{def}}$ of the system with $M \times M$ lenslets and normalised radius $0 \leq \rho \leq 1$ may be approximated in the following way:

$$\begin{aligned} \phi_1 &= 2\pi\Delta\lambda_{\text{def}}\rho^2, \\ M \langle \nabla \phi \rangle_{\max} &= 4\pi\Delta\lambda_{\text{def}}, \\ \Delta\lambda_{\text{def}} &= \frac{Mp^2}{8\lambda f_A}. \end{aligned} \quad (1.31)$$

A typical lenslet array could have $p = 300\mu\text{m}$, $f_A = 17.526\text{ mm}$, and around $M = 400$ lenslets — this gives a $\Delta\lambda_{\text{def}} \approx 26$ or 165 radians peak-to-valley at $\lambda = 500\text{nm}$. Other aberrations have a more complex spatial distribution and therefore, back of the envelope calculations for these are not as straightforward as the one for defocus.

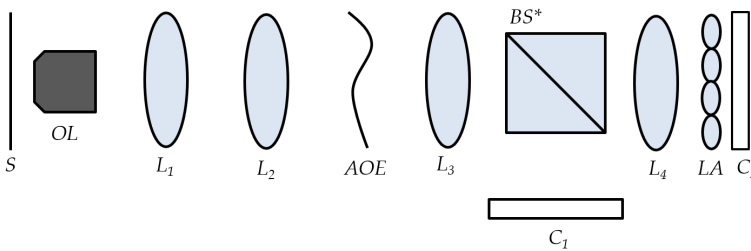


Figure 1.10: Pupil-plane wavefront sensing setup with a Shack-Hartmann sensor. *The beam-splitter (BS) here can be a dichroic beam splitter. *S* - sample; *OL* - objective lens; *L_n* - lens; *AOE* - adaptive optical element; *BS* - beam splitter; *LA* - lenslet array; and *C* - camera.

The signal level, however, will be the biggest hindrance to successful operation. Each sub-aperture of the sensor reduces signal-to-noise ratio of the measurement.

The noise in the centroid measurements affects the ability to correctly identify the wavefront. This means it may be necessary to reduce the number of sub-apertures, in turn reducing the spatial resolution and dynamic range of the sensor, in order to have a working system.

For example, it is theoretically possible to have an AO system that could continually correct for every position of the scanner in a confocal scanning or multi-photon system. The problem here is that sensor would have to be able to detect light at low signal-to-noise ratios and high-speeds that are out of reach for even the best current EMCCD³ cameras. As a compromise with the sensor the signal may be integrated over the whole period of a single frame, the de-scanned light will be averaged over the sensor giving the average aberration over the field-of-view instead — not as good correction, but better than nothing at all.

As an aside, the PP-WFS can also be used on wide-field images, only if a field stop or “guide stars” are used. In this case, the fluorophore needs to be very bright and the noise reduced as much as possible. Another approach is to use the multiple images of the sample and use cross-correlation to detect local shifts in the images [73]. This once again requires a very good signal-to-noise ratio for successful application. To conclude, for wide-field imaging especially and fluorescence microscopy in general it is not usually possible to employ a pupil-plane sensor and therefore, focal-plane sensing is employed.

The Focal-Plane Wavefront Sensor

Aberration correction based on a focal-plane wavefront sensor (FP-WFS) is generally performed by using the information from the microscope images themselves to estimate the optimal correction to apply on the AOE. All that is necessary for realizing a FP-WFS system is the inclusion of the corrector normally still in the pupil-plane of the system (possibly in other places too), which is usually done through a 4-f telescope. This is schematically shown in Fig.1.11.

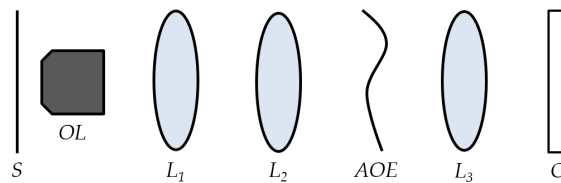


Figure 1.11: Focal-plane wavefront sensing setup. *S* - sample; *OL* - objective lens; *L_n* - lens; *AOE* - adaptive optical element; and *C* - camera.

From an imaging point-of-view, the great advantage of this sensor is that no light is subtracted from the imaging system in order to perform aberration correction. On the other hand, since the relationship between the aberrations and image quality is non-linear, sensing the wavefront requires the acquisition of a substantial amount of

³Electron Multiplying Charge-Coupled Device

images. While the wavefront can be elucidated by a pupil-plane wavefront sensor in 1-10 frames depending on the signal-to-noise ratio, it will take at least an order of magnitude more frames to acquire the same information with a FP-WFS due to the non-linearity [74].

The relationship between the phase in the pupil $\phi(v, \nu)$, at the location of the corrector, and the intensity in the image plane $i(x, y)$, at the sensor is, in the case of an isoplanatic aberration for incoherent imaging is modelled by:

$$i(x, y) = |\mathcal{F}\{A(v, \nu)e^{j\phi(v, \nu)}\}|^2 * o(x, y), \quad (1.32)$$

where $o(x, y)$ represents the fluorophore distribution, which for the analysis here can be a point-source δ -function. The shape of the aperture is given by the function $A(v, \nu)$. Dropping the spatial dimensions, a corrector can introduce a change to the phase in the pupil such that it becomes $(\phi + \varphi)$ and a metric function $\sigma(i(\varphi))$ defining the quality or “goodness” of an image can be maximised:

$$\max_{\varphi} \sigma(i(\varphi)) \text{ or } \max_{\varphi} \sigma(|\mathcal{F}\{Ae^{j(\phi+\varphi)}\}|^2). \quad (1.33)$$

In order to maximise the metric, an optimisation algorithm must be employed (see Section 1.7.5). Some information, however, about the metrics is required at this point. If one is dealing with a point-source, this is simpler than an extended source because one knows *a priori* what is being looked at. In this case, maximisation of the brightest point, the second central moment of the spot, the image standard deviation or the spatial frequency content will all yield a optimisation that converges to the diffraction-limited spot. Depending on the order of the corrector, the length of time taken is dependent on the sensitivity of the metric and how many local maxima it has and how deep they are.

On the other hand, if one has an extended source the problem is much more difficult. It is not known *a priori* what the best image is. A good approach in this case is to include some *a priori* information, for example, if it is possible to encode a particular spatial frequency into the image by modulating the illumination [75]. In this case, maximising this particular spatial frequency is akin to reducing the aberration. If modulation of the illumination is not possible then maximisation of the power spectrum of the image within a given radius in the Fourier domain is an alternative and a somewhat robust methodology [76]. The success or failure of these optimisation procedures is very dependent on the amount of out-of-focus fluorescence and the photo-bleaching rate.

A drawback is that most metrics are indirectly dependent on the amount of signal. As the procedure can take many frames, the minimum is $N + 1$ where N is the number of actuators [74], it is not uncommon that the amount of light collected from the fluorophores decreases over this period of minutes [77]. This can lead to frames later in the acquisition being scored lower or higher than those at the start, leading to a misleading quantification — especially if the approach is model-based (see Section 1.7.5). The summation of out-of-focus fluorescence can also lead to false-positive optimisation.

Furthermore, it is often necessary to exclude displacement modes (i.e. tip, tilt and defocus) from one's optimisation space since instead of changing the image quality, they move the FOV through the sample, and the correction procedure would therefore just find the FOV where the metric is maximized, not the maximum of the desired FOV. These considerations makes wavefront sensing with extended objects in wide-field microscopy problematic. It is likely, that one will converge to a local maxima that is better than the original image, but is not the globally optimally solution, to represent this mathematically one could say, the optimum solution x^* :

$$x^* = \arg \min_x \|\phi - \varphi(x)\|, \quad (1.34)$$

gives a residual $\epsilon > 0$, which is the correction to the sensitivity of the adaptive optics system. In the case of a non-optimal solution \hat{x} , the following is true:

$$\|\phi - \varphi(\hat{x})\| > \epsilon \forall \hat{x} \in \mathcal{X} \setminus x^*, \quad (1.35)$$

where \mathcal{X} is the set of all possible inputs to the system.

Wavefront Correction

If one can now assume it is possible to obtain the wavefront through the methods of sensing presented then in order to perform correction of aberrations, a multi-actuator, two-dimensional phase modulator is need. This is generally placed in a pupil-plane of the system. With the exception of deformable lenses [78], and transmissive liquid crystal spatial light modulators, most phase modulators are reflective and since the pupil-plane of most microscope objective is located physically inside the objective itself, a secondary pupil-plane must be created through a 4-f relay telescope. This is illustrated in Fig. 1.12, where the AOE is placed in plane P' conjugate to the pupil-plane inside the objective.

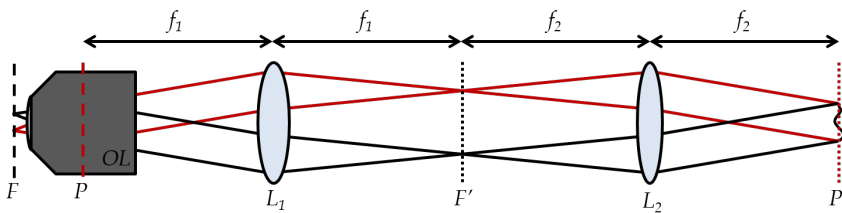


Figure 1.12: Where to place the corrector in a pupil-plane configuration, in P' that is conjugated via a 4-f system to the objective pupil-plane P .

The size of the back aperture plane of the objective should be calculated from its magnification and numerical aperture, and the focal lengths of the telescope must be correctly estimated so that the image of the objective's pupil-plane at the AOE location is equal to the size of the active area of the AOE. In general, it is good practice to design the optical system with a specific microscope objective and AOE

Table 1.1: Information on different types of types of AOE.

Type	Speed	Stroke	Order	Hysteresis	Cost
Piezo [79]	★★★	★★	★	★	€
Membrane [79]	★★★	★★	★★	★★★★	€
Voice Coil [80]	★★★	★★★★★	★★	★★	€€
Micromachined [81]	★★★	★	★★★★★	★★★★★	€€€€
LCD SLM [82]	★	★★★★★	★★★★★	★★★★★	€€€
Adaptive Lens [83]	★★	★	★	★	€€

in mind, because the use of a different objective, or an AOE of different size, would require a re-design of the telescope conjugating the two planes.

In the case of deformable mirrors (DM), the main actuator technologies commercially available are piezo-electric, electrostatic membrane, voice coil and micro-machined silicon. A notable alternative is constituted by liquid crystal spatial light modulators, which only work on coherent monochromatic light, and are therefore only suitable for multi-photon laser scanning microscopy and cannot be used on the incoherent fluorescent light.

Each technology represents a trade-off in the main technical specifications, namely: speed, order of correction, correction stroke, repeatability of the correction, and cost. A summary of performance comparison is reported in Table 1.1. The reader should notice that no numbers are reported, as constant evolution of technology means the better products are often reported on the market. The main features of correctors that need to be considered are the following:

Speed It is generally not considered as a critical parameter for microscopy, as the response time of most DMs (usually on the sub-millisecond scale) is much faster than the frame rate of any microscope, or any wavefront sensor operating in low light conditions. Spatial light modulators are a notable exception to this, as their refresh time can be as low as a few Hz, and may constitute a limit to the correction speed of the entire AO system.

Stroke Stroke is a sample-dependent parameter. A high stroke, however, can be extremely helpful in some specific situations. When using dry objectives or oil immersion objectives, a severe spherical aberration will appear and increase linearly with sample depth, and can only be compensated with with very high stroke mirrors. Moreover, high stroke especially in the low-orders allows for additional refocusing or scanning capabilities.

Number of Actuators / Order It is a very sample specific parameter, as the amplitude and order of aberrations can vary wildly with the index of refraction distribution in a biological sample. It must be considered, however, that while a high order corrector with a high number of actuators can achieve correction in highly scattering materials [67], the size of the field-of-view where the correction is valid decreases with the order of the aberration, so that special and more complex hardware and software configurations are needed to take full advantage of a high-order corrector. Moreover, higher numbers of actuators require longer optimisation procedures, or higher numbers of sub-apertures in wave-front sensors, therefore, this reduces the usability of the microscope. It is, therefore, a generally good suggestion for a simple isoplanatic AO system to choose lower order correctors.

Hysteresis & Creep Piezo-electric actuators, and less noticeably voice coil actuators, are affected by hysteresis and creep. Hysteresis is where the direction of the change of input will affect the response of the corrector and creep is where the set-point of the corrector changes with time. These properties of the corrector may hinder the repeatability and stability of input response. While this is a generally negligible problem in the case of pupil-plane wavefront sensing and model-free optimisation methods, model-based optimisation applications can be greatly affected, so hysteresis-free modulators such as membrane mirrors are to be preferred for this.

1.7.5. Controllers

The purpose of a controller is to take the sensor measurements or the reconstruction of the wavefront, either from the focal-plane or the pupil-plane and convert this into control inputs for the corrector. The block scheme for this whole system is shown in Fig. 1.13.

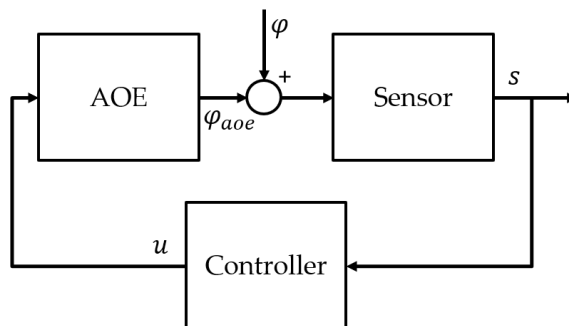


Figure 1.13: The adaptive optics control block scheme. There are three parts to the system, the AOE, the sensor and the controller. The variables here are the aberration phase φ , the corrector control inputs u that lead to a correction phase φ_{aoe} and the sensor outputs s .

Whilst the function of the controller is the same in all adaptive optics systems, its design and function depend on its context. The controller can be made in a number of ways and best method depends on the type of sensor used, the application, and the

corrector. A summary of the general approaches used in the literature are summed up in Table 1.2.

Table 1.2: Information on different types of AO control. The values in the Table are approximations based on current technological possibilities and will change over time. SH is Shack-Hartmann sensor.

Type	Speed	Aberration Size	Order	SNR
Model-free optimisation	$\mathcal{O}(10^2)$ s	$< 60\lambda$	< 20	> 10 dB
Model-based optimisation	$\mathcal{O}(10^1)$ s	$< 20\lambda$	< 60	> 15 dB
Pupil-plane with SH	$\mathcal{O}(10^{-2})$ s	$< 40\lambda^*$	< 60	> 10 dB

* The limit is on the phase gradient within a lenslet as discussed in Section 1.7.4.

The first type of control is called *model-free* and the second category is *model-based*. From the names it is possible to imagine that the difference in these two is the explicit making of a mathematical model of parts of the optical system: the AOE, the sensor and the propagation of light through the other components. From this model a relationship between the sensor outputs and the control inputs can be elucidated and a controller designed to manage this feedback [49, 60].

Model-free control on the other hand has no built in model of the system. It simply reacts to the measurements it takes and tries to steer the system towards a pre-defined goal: the minimisation or maximisation of a metric. Model-free can only really apply to the case of focal-plane sensing, it would be possible to apply this to a pupil-plane sensing but it is not immediate clear why one would want to do this. Since the purpose of using a wavefront sensor is so that there is a simple linear relationship between the correction phase and the measurement. This linear relationship, is an example of something that arises from the mathematical model and allows the correction to be done very quickly and with *closed-loop* feedback.

A good summary between the two optimisation techniques would be: model-free control requires little calibration, but is slower to correct; whereas model-based control requires long systematic calibration, but is faster to correct. When comparing these with a pupil-plane sensing scheme one notes that the sensor is going to be faster, but requires the removal of photons or the addition of guide stars in the sample.

Control with Pupil-Plane Sensors

There are many complex methods of control for pupil plane sensors, but the simplest approximates the relationship between the sensor and the corrector as being purely linear, the aberration is assumed to be *static*, which is often a good assumption in microscopy. This behaviour is contained in H , the influence matrix, and it is responsible for turning centroid displacements \mathbf{s} from a flat reference into actuators inputs \mathbf{u} for

the AOE:

$$\mathbf{s} = H\mathbf{u} \quad (1.36)$$

The Shack-Hartmann sensor output is a vector of centroid displacements for a 2D array of focal points. It is possible to relate the average phase gradient $\langle \nabla \phi \rangle_i$ in the i^{th} sub-aperture to the centroid displacement (\bar{x}_i, \bar{y}_i) of the focal spot in the sub-aperture by:

$$s_i = (\bar{x}_i, \bar{y}_i) \approx f_A \langle \nabla \phi \rangle_i = f_A \left(\left\langle \frac{\partial \phi}{\partial x} \right\rangle_{(x_i, y_i)}, \left\langle \frac{\partial \phi}{\partial y} \right\rangle_{(x_i, y_i)} \right). \quad (1.37)$$

To control the system, one needs to find first a flat reference input array, \mathbf{u}_0 , through optimisation (see Section 1.7.5) and then one can calculate the matrix H relative to this flat wavefront position. The simplest way to do this is by measuring the response of the sensor to a perturbation of a single actuator, for example, actuator 1:

$$\mathbf{s}_1 = H \begin{pmatrix} 1 \\ 0 \\ \vdots \\ 0 \end{pmatrix} = \begin{pmatrix} H_{11} & 0 & \dots & 0 \\ H_{21} & 0 & \dots & 0 \\ \vdots & \vdots & \ddots & \vdots \\ H_{N1} & 0 & \dots & 0 \end{pmatrix}, \quad (1.38)$$

when repeated for all actuators this builds up a complete H matrix. To use for control, it needs to be inverted either using the Penrose-Morse pseudo-inverse or single value decomposition (SVD). In pseudo-inverse form it appears as the following:

$$\mathbf{u} = (H^T H)^{-1} H^T \mathbf{s} \quad (1.39)$$

For closed-loop operation, it is often necessary to feedback a fraction of this ($0 \leq \gamma \leq 1$) to the existing input signals to increase the robustness of the controller, in the following manner:

$$\mathbf{u}^{(k+1)} = \mathbf{u}^{(k)} - \gamma (H^T H)^{-1} H^T \mathbf{s}^{(k)}. \quad (1.40)$$

Control with Focal-Plane Sensors

Both model-based and model-free optimisation techniques depend on the computation of a metric to quantify the quality of the image, as in Eq. (1.33). An optimisation algorithm is then used to find the maximum (or minimum) of this metric. This metric may be considered to form a multi-dimensional surface, where one is trying to find the highest peak (or lowest). In Fig. 1.14 the value of some metric is shown in schematic form for a AOE with two degrees of freedom. The type of algorithm, Fig. 1.14(a) showing a model-based approach and Fig. 1.14(b) showing the model-free approach determines the set of measurements at specific inputs that need to be measured to find the peak.

The figure has been intentionally drawn to show that there can be two types of metric shapes in general, those that are *convex* with respect to the degrees of freedom as in Fig. 1.14(a) or *non-convex* as in Fig. 1.14(b). Non-convexity implies that function does not have one unique maximum and it is possible to converge to a local maxima, that do not offer the globally best solution. Whereas, in convex optimisation if one converges to a maximum one can be certain that it is global.

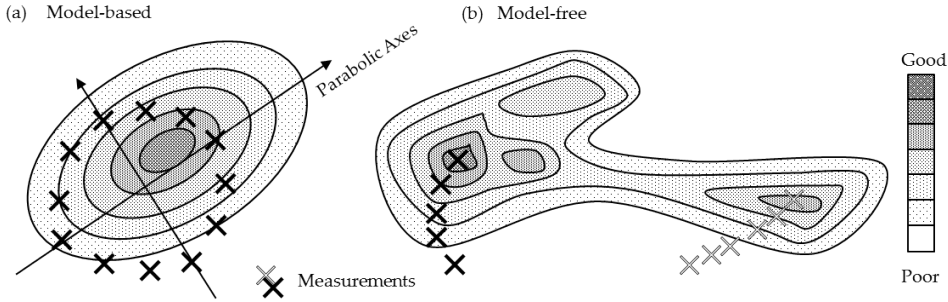


Figure 1.14: A sketch of difference between (a) model-based optimisation approach where a set of measurements are taken in a pre-defined pattern to calibrate the system before optimisation and (b) model-free optimisation approaches where measurements are taken sequentially based on the value of the metric. In most adaptive optics systems this optimisation landscape is in many more dimensions and depending on the metric may have more or less local maxima.

Model-free optimisation Model-free control is usually performed with non-convex metrics, systems that are not well-defined, change their behaviour with time, or have a low signal-to-noise ratio. It is an approach that is most likely to work to control an adaptive optical system. The method is slow, but it is robust and is able to operate with a low signal-to-noise ratio on a system that you do not know very much *a priori* about. As such, it is recommended to use this approach to test whether the combination of AOE and your application are compatible and then to progress to a more complex methodology. In Fig. 1.14(b) the model-free approach is shown for two starting conditions described by the white and black crosses. In the black crosses case, the algorithm starts and takes steps in the direction of increasing metric value, and converges to the maximum of the function. In contrast to this, the white crosses show the same algorithm starting in a different initial position where it converges instead to a local maximum that does not give the optimal correction.

Metrics The landscapes shown in Fig. 1.14 are defined by the metric and the degrees of freedom of the AOE. The first and most crucial step is designing a metric to evaluate the aberration as this strongly affects the ability to perform correction. As previously remarked upon, in wide-field microscopy the definition of such a metric is challenging and can be very sample dependent. Nevertheless, examples of the broad spectrum of approaches are listed here:

- Brightness — $\sum_{xy} i(x, y)$ [37].
- Sharpness — $\sum_{xy} i(x, y)^2$ [84].
- Frequency content in \mathcal{R} — $\sum_{\mathcal{R}} |\mathcal{F}\{i(x, y)\}|^2$ [76].
- Intensity gradient⁴ — $\sum_{xy} |\nabla i(x, y)|^2$ [84].

⁴sometimes called sharpness too

- Second central moment — $\sum_{x,y}(x - \bar{x})^2(y - \bar{y})^2 i(x, y)$ [85].

The shape of these metrics for the same microscope can be very different and make it easier or harder to optimise. For example, the convex shape of the metric in Fig.1.14(a) will allow for fast and efficient correction due to the ability to make a parabolic approximation to the metric function, whereas in Fig.1.14(b) the optimisation will be slow and inefficient since it can converge to alternative maxima.

Algorithms The choice of algorithm is not as important as the metric, however, for a given application one may desire the measurements to progress in a particular manner — such as small incremental steps rather than large scans. An incomplete list of algorithms is given here:

- *Coordinate Search (CS)* [56] — sequentially scan through a range of aberration values along the degrees of freedom and find the maxima. Simple to implement and fairly robust, but can give a result that is not a true maximum.
- *Stochastic Gradient Descent/Ascent* [86] — randomly perturb the aberration values by a small amount, if it gives a better value keep the perturbation, if not revert. Will converge to local maxima.
- *Gradient Descent/Ascent* [87] — measure the multi-dimensional gradient of the metric then take a positive step in the steepest direction. This will quickly converge to a local maximum but can easily diverge in the presence of noise.
- *Second-order gradient methods, BFGS* [88], etc. — these compute the Hessian to find extra information about the metric function. Faster than first-order methods but even more sensitive to noise. These work better with analytically evaluable functions and again these can diverge if the noise is too high.
- *Simplex* [89] — measure the metric for a set of aberration values then compute the metric weighted centre-of-mass in the aberration coefficients space, next measure the metric at this new aberration values and replace the lowest metric value with the new measurement then repeat. Will converge to the closest local maximum, it is slower but less sensitive to noise than the gradient-based approaches.
- *Genetic algorithms, simulated annealing, etc.* [37] — work by searching the space of possible aberration values for the most “fit” solution. These algorithms are for when one has a poor understanding or knowledge of the metric or system. They are almost certain to converge to the global maximum, but can take a very long time to get there.
- *DONE algorithm* [90] — an algorithm developed by Blik et al., works by generating a dynamic model of the metric function as a series of cosine functions whose coefficients are determined by the available measurements of the metric.

Each successive new measurement is performed close to the estimated minimum of the function, and added to the model. Slower in convergence than the gradient-based methods, but it is extremely robust to noise and can avoid local maxima. Careful hyper-parameters determination is required making it quasi-model-based.

Model-based optimisation Model-based control requires the use of *a priori* information about the setup and the nature of light propagation through aberrations. A mathematical model is made of how the variables (control inputs) affect the metric. This type of control imposes much more stringent conditions on the optical setup and is sensitive to anything that can change the model, such as misalignment or different sample types, etc.

In most model-based AO implementations in microscopy, the metric is assumed to be a quadratic function of the correction inputs x :

$$\begin{aligned} M(x) &\approx M_0 - x^T \mathbf{B}x, \\ M_0 &\in \mathbb{R}, \\ x &\in \mathbb{R}^N, \\ \mathbf{B} &\geq 0 \in \mathbb{R}^{N \times N}, \end{aligned} \tag{1.41}$$

which is a system with N degrees of freedom (usually the number of actuators of the AOE), and is determined by $\mathcal{O}(N^2)$ parameters. It is possible to determine, usually through a lengthy calibration procedure, in the manner shown in Fig. 1.14 where a circle in the space of the bases is used to find the parabolic axes of the metric. With this specific aberration base where the matrix B is diagonal, the function can be more easily expressed as:

$$M(x) = M_0 + \sum_{n=1}^N b_n x_n^2. \tag{1.42}$$

In this case, the absolute minimum can be easily found, in low noise scenarios, with only $2N + 1$ measurements, by measuring the value of the metric with no correction applied, and subsequently for two additional values of each coordinate of the aberration base. With this data the optimal values of b_n can be easily identified, and the minimum location can be extrapolated.

This provides much faster convergence than any model-free method, reaching performances similar to those of a wavefront sensor based system. Calibration of a base respecting the condition in Eq. (1.42) is non-trivial and small misalignments of the system, or use of different samples can easily render the calibration ineffective, severely affecting the performances of the optimisation. A few examples may be found in the following articles:

1. Second central moment metric with Lukosz-Zernike (LZ) functions [51].
2. Mean image intensity in two-photon microscopy with an orthogonalised base [56].

3. Second central moment metric with gradient orthogonal functions [91].

In summary, the advantage yielded by these techniques is that the speed at which correction may be done is increased over model-free approaches. The disadvantage of this approach is that the technique requires the metric function to have a known form, which can generally only be guaranteed over a small aberration range. If one wishes to apply this approach, one must find a good metric for one's imaging modality and quantify it analytically. From this model of the image formation process calculate a set of basis functions that are orthogonal with respect to this metric. In this way, within the scope of the model the metric function will be convex around the maximum of the function for small enough perturbations and correction can be done quickly.

1.8. The Motivation & Outline of this Thesis

1.8.1. Motivation

Adaptive optics for fluorescence microscopy has evolved over the last thirty years into a set of well-developed methods for the correction of aberrations originating from the inhomogeneity of biological samples. The quality of these systems has increased with this research combined with the availability of new technologies that has made the process more accessible, faster, more sensitive and in many cases simpler.

This does not imply that the work is finished or that there is no where to go in the investigation of techniques and methodologies for adaptive optics in microscopy. It was decided at the start of the work on this thesis to focus the research on the implementation of adaptive optics in light-sheet fluorescence microscopy. The rationale behind this decision were the following points.

Potential Impact The use of light-sheet fluorescence microscopy had been increasing from its rediscovery in the 2000s including in new applications and contexts. Since the use of light-sheet microscopy is only logical with three-dimensional samples, where sectioning is necessary, there are always aberrations. The application of adaptive optics, therefore, solves an outstanding problem with the technique. It is a technique that is likely to continue to expand in the future and work on building the foundations of applying adaptive optics in this modality would hopefully be useful providing a starting point for any future implementations.

Novelty Whilst adaptive optics had been already applied in the fluorescence detection path of the microscopy [65], there was still much room for novel research. No work had yet been attempt to truly optimise the illumination of the microscope. Both in the sense of correcting for the system design through adaptive optical element and feedback, and also for the aberrations that strongly affected the optical sectioning ability of the microscope. Furthermore, the literature on the application of adaptive optics in wide-field microscopy was also sparse. It was deemed that improvements to the correction of aberrations in wide-field modalities would also be an element in the thesis.

Interesting Problems From both an optical design perspective and control perspective an adaptive light-sheet fluorescence microscope has interesting challenges. It has two optical paths that would require the integration of two adaptive optical elements. The images one obtains on the camera are influenced by both of these elements, the two paths are not independent. One must find methods that are not influenced by the potential cross-talk between the elements whilst correcting for aberrations both on the excitation and emission paths.

1.8.2. Outline

Given the motivations described above, the goal of the thesis was to (1) find methods to optimise the shape of the illumination light to provide a more uniform beam over the field of view of the microscope, (2) correct for the aberrations in the illumination path and (3) correct for illuminations in the fluorescence detection. The thesis has been organised to cover this research in the following order:

Shaping the Illumination Chapter 2 looks specifically at the illumination system in a light-sheet fluorescence microscope. It is assumed that one is able to shape the incident light. What then is the optimal phase pattern to apply in order to image successfully with these microscopes? The chapter explores the design and use of binary pupil filters to generate an extension of the depth of field of the illumination system of the light-sheet microscope.

This chapter is based on the work that has been published in the following article:

Pupil filters for extending the field-of-view in light-sheet microscopy, **D Wilding**, P Pozzi, O Soloviev, G Vdovin, CJ Sheppard, M Verhaegen, *Optics letters* **41** (6), 1205-1208 11 (2016)

Correcting the Illumination Chapter 3 covers the sensing and detection of aberrations in the illumination system of a light-sheet microscope. The illumination in this system must travel through the sample to illuminate a plane so that its fluorescence from this plane can be detected. If there are aberrations the light-sheet becomes thicker and distorted leading to a misrepresentation of the three-dimensional fluorescence distribution. How can this be sensed and corrected? In this chapter a wavefront sensor is used on the epi-fluorescent light to detect and then using feed-forward control correct the aberration improving the image quality.

This chapter is based on the work that has been published in the following article:

Adaptive illumination based on direct wavefront sensing in a light-sheet fluorescence microscope, **D Wilding**, P Pozzi, O Soloviev, G Vdovin, M Verhaegen, *Optics express* **24** (22), 24896-24906 4 (2016)

Correcting the Image: Part One Chapter 4 concerns itself with correcting wide-field images in general. It is not specific *per se* to microscopy, however, the techniques

described were developed for the use in microscopy. Deconvolution techniques tend to produce non-physical results if the information about the aberration is not well-known. What can be done to improve the deconvolution of the images from a microscope? In this chapter the development of an algorithm for combining multiple observations of a sample with varying point-spread functions is proposed as a solution.

This chapter is based on the work that has been published in the following article:

Blind multi-frame deconvolution by tangential iterative projections (TIP), **D Wilding**, O Soloviev, P Pozzi, G Vdovin, M Verhaegen, *Optics express* **25** (24) (2017)

Correcting the Image: Part Two Chapter 5 continues on from Chapter 4 as the application of the general technique for use in fluorescence microscopy. Is it possible to capture successful images without correcting the wavefront? This chapter explore the possibility of computational correction of the images using multiple observations assisted by the physical perturbation of the optical system.

This chapter is based on the work that has been published in the following article:

Pupil mask diversity for image correction in microscopy, **D Wilding**, P Pozzi, O Soloviev, G Vdovin, M Verhaegen, *Optics express* **26** (12) (2018)

References

- [1] D. Wilding, P. Pozzi, O. Soloviev, G. Vdovin, and M. Verhaegen, *Practical guidelines for implementing adaptive optics in fluorescence microscopy*, (2018) pp. 10502 – 10502 – 12.
- [2] M. Born and E. Wolf, *Principles of Optics* (Cambridge University Press, 1959).
- [3] J. W. Goodman, *Introduction to Fourier optics* (Roberts and Company Publishers, 2005).
- [4] E. G. Ruestow, *The microscope in the Dutch Republic: The shaping of discovery* (Cambridge University Press, 1996).
- [5] A. van Leeuwenhoek, *The select works of anthony van leeuwenhoek: containing his microscopical discoveries in many of the works of nature*, Vol. 1 (translator, 1800).
- [6] R. Hooke, *Micrographia* (1665).
- [7] G. G. Stokes, *On the change of refrangibility of light*, Philosophical Transactions of the Royal Society of London **142**, 463 (1852).
- [8] H. Rinderknecht, *Ultra-rapid fluorescent labelling of proteins*, Nature **193**, 167 (1962).
- [9] M. Chalfie, Y. Tu, G. Euskirchen, W. W. Ward, and D. C. Prasher, *Green fluorescent protein as a marker for gene expression*, Science **263**, 802 (1994).
- [10] S. W. Hell and J. Wichmann, *Breaking the diffraction resolution limit by stimulated emission: stimulated-emission-depletion fluorescence microscopy*, Optics letters **19**, 780 (1994).
- [11] E. Betzig, G. H. Patterson, R. Sougrat, O. W. Lindwasser, S. Olenych, J. S. Bonifacino, M. W. Davidson, J. Lippincott-Schwartz, and H. F. Hess, *Imaging intracellular fluorescent proteins at nanometer resolution*, Science **313**, 1642 (2006).
- [12] M. J. Rust, M. Bates, and X. Zhuang, *Sub-diffraction-limit imaging by stochastic optical reconstruction microscopy (storm)*, Nature methods **3**, 793 (2006).
- [13] I. Ferezou, S. Bolea, and C. C. Petersen, *Visualizing the cortical representation of whisker touch: voltage-sensitive dye imaging in freely moving mice*, Neuron **50**, 617 (2006).
- [14] M. Minsky, *Confocal scanning microscope*, Rapport technique, Patent **3** (1955).
- [15] M. Minsky, *Confocal patent focal scanning microscope*, US patent, serial (1957).

- [16] W. Amos and J. White, *How the confocal laser scanning microscope entered biological research*, *Biology of the Cell* **95**, 335 (2003).
- [17] W. Denk, J. H. Strickler, W. W. Webb, *et al.*, *Two-photon laser scanning fluorescence microscopy*, *Science* **248**, 73 (1990).
- [18] F. Helmchen and W. Denk, *Deep tissue two-photon microscopy*, *Nature methods* **2**, 932 (2005).
- [19] H. Siedentopf and R. Zsigmondy, *Ueber sichtbarmachung ultramikroskopischer teilchen, mit besonderer anwendung auf goldrubinglaser*, *Drude's Annalen der Physik, t., X. J. Phys. Theor. Appl.* **2**, 692–702 (1903).
- [20] J. Huisken, J. Swoger, F. Del Bene, J. Wittbrodt, and E. H. Stelzer, *Optical sectioning deep inside live embryos by selective plane illumination microscopy*, *Science* **305**, 1007 (2004).
- [21] A. Voie, D. Burns, and F. Spelman, *Orthogonal-plane fluorescence optical sectioning: Three-dimensional imaging of macroscopic biological specimens*, *Journal of microscopy* **170**, 229 (1993).
- [22] M. Tokunaga, N. Imamoto, and K. Sakata-Sogawa, *Highly inclined thin illumination enables clear single-molecule imaging in cells*, *Nature methods* **5**, 159 (2008).
- [23] C. Dunsby, *Optically sectioned imaging by oblique plane microscopy*, *Optics express* **16**, 20306 (2008).
- [24] M. B. Bouchard, V. Voleti, C. S. Mendes, C. Lacefield, W. B. Grueber, R. S. Mann, R. M. Bruno, and E. M. Hillman, *Swept confocally-aligned planar excitation (scape) microscopy for high-speed volumetric imaging of behaving organisms*, *Nature photonics* **9**, 113 (2015).
- [25] M. B. Ahrens, M. B. Orger, D. N. Robson, J. M. Li, and P. J. Keller, *Whole-brain functional imaging at cellular resolution using light-sheet microscopy*, *Nature methods* **10**, 413 (2013).
- [26] S. Kumar, D. Wilding, M. B. Sikkell, A. R. Lyon, K. T. MacLeod, and C. Dunsby, *High-speed 2d and 3d fluorescence microscopy of cardiac myocytes*, *Optics express* **19**, 13839 (2011).
- [27] J. W. Hardy, *Adaptive optics for astronomical telescopes*, Vol. 16 (Oxford University Press on Demand, 1998).
- [28] G. Vdovin and P. Sarro, *Flexible mirror micromachined in silicon*, *Applied optics* **34**, 2968 (1995).

- [29] T. G. Bifano, R. K. Mali, J. K. Dorton, J. A. Perreault, N. Vandelli, M. N. Horenstein, and D. A. Castanon, *Continuous-membrane surface-micromachined silicon deformable mirror*, *Optical Engineering* **36**, 1354 (1997).
- [30] C. Paterson, I. Munro, and J. C. Dainty, *A low cost adaptive optics system using a membrane mirror*, *Optics Express* **6**, 175 (2000).
- [31] M. J. Booth, M. Neil, and T. Wilson, *Aberration correction for confocal imaging in refractive-index-mismatched media*, *Journal of Microscopy* **192**, 90 (1998).
- [32] C. J. Sheppard and M. Gu, *Aberration compensation in confocal microscopy*, *Applied optics* **30**, 3563 (1991).
- [33] J. O'Byrne, P. Fekete, M. Arnison, H. Zhao, M. Serrano, D. Philp, W. Sudiarta, and C. Cogswell, *Adaptive optics in confocal microscopy*, in *Proceedings of the 2nd International Workshop on Adaptive Optics for Industry and Medicine*, GD Love, ed. (World Scientific, 1999) (Citeseer, 1999).
- [34] A. Thayil and M. J. Booth, *Self calibration of sensorless adaptive optical microscopes*, *Journal of the European Optical Society-Rapid publications* **6** (2011).
- [35] T. Wilson, M. A. Neil, and M. J. Booth, *Dynamic wavefront control in confocal microscopy*, in *18th Congress of the International Commission for Optics*, Vol. 3749 (International Society for Optics and Photonics, 1999) pp. 498–500.
- [36] M. J. Booth, M. A. Neil, R. Juškaitis, and T. Wilson, *Adaptive aberration correction in a confocal microscope*, *Proceedings of the National Academy of Sciences* **99**, 5788 (2002).
- [37] O. Albert, L. Sherman, G. Mourou, T. Norris, and G. Vdovin, *Smart microscope: an adaptive optics learning system for aberration correction in multiphoton confocal microscopy*, *Optics letters* **25**, 52 (2000).
- [38] M. Mitchell, *An introduction to genetic algorithms* (MIT press, 1998).
- [39] M. A. Neil, M. J. Booth, and T. Wilson, *New modal wave-front sensor: a theoretical analysis*, *JOSA A* **17**, 1098 (2000).
- [40] R. J. Noll, *Zernike polynomials and atmospheric turbulence*, *JOSA* **66**, 207 (1976).
- [41] Z. von F, *Beugungstheorie des schneidenverfahrens und seiner verbesserten form, der phasenkontrastmethode*, *Physica* **1**, 689 (1934).
- [42] M. Neil, R. Juškaitis, M. Booth, T. Wilson, T. Tanaka, and S. Kawata, *Adaptive aberration correction in a two-photon microscope*, *Journal of microscopy* **200**, 105 (2000).
- [43] Z. Kam, B. Hanser, M. Gustafsson, D. Agard, and J. Sedat, *Computational adaptive optics for live three-dimensional biological imaging*, *Proceedings of the National Academy of Sciences* **98**, 3790 (2001).

- [44] L. Sherman, J. Ye, O. Albert, and T. Norris, *Adaptive correction of depth-induced aberrations in multiphoton scanning microscopy using a deformable mirror*, Journal of microscopy **206**, 65 (2002).
- [45] M. J. Booth and T. Wilson, *Refractive-index-mismatch induced aberrations in single-photon and two-photon microscopy and the use of aberration correction*, Journal of biomedical optics **6**, 266 (2001).
- [46] M. J. Booth, M. A. Neil, and T. Wilson, *New modal wave-front sensor: application to adaptive confocal fluorescence microscopy and two-photon excitation fluorescence microscopy*, JOSA A **19**, 2112 (2002).
- [47] P. Marsh, D. Burns, and J. Girkin, *Practical implementation of adaptive optics in multiphoton microscopy*, Optics Express **11**, 1123 (2003).
- [48] A. J. Wright, D. Burns, B. A. Patterson, S. P. Poland, G. J. Valentine, and J. M. Girkin, *Exploration of the optimisation algorithms used in the implementation of adaptive optics in confocal and multiphoton microscopy*, Microscopy Research and Technique **67**, 36 (2005).
- [49] M. Booth, *Wave front sensor-less adaptive optics: a model-based approach using sphere packings*, Optics Express **14**, 1339 (2006).
- [50] M. Rueckel, J. A. Mack-Bucher, and W. Denk, *Adaptive wavefront correction in two-photon microscopy using coherence-gated wavefront sensing*, Proceedings of the National Academy of Sciences **103**, 17137 (2006).
- [51] M. J. Booth, *Wavefront sensorless adaptive optics for large aberrations*, Optics letters **32**, 5 (2007).
- [52] J. Braat, *Polynomial expansion of severely aberrated wave fronts*, JOSA A **4**, 643 (1987).
- [53] W. Lukosz, *Der einfluß der aberrationen auf die optische übertragungsfunktion bei kleinen orts-frequenzen*, Optica Acta: International Journal of Optics **10**, 1 (1963).
- [54] Z. Kam, P. Kner, D. Agard, and J. W. Sedat, *Modelling the application of adaptive optics to wide-field microscope live imaging*, Journal of microscopy **226**, 33 (2007).
- [55] P. Kner, J. Sedat, D. Agard, and Z. Kam, *High-resolution wide-field microscopy with adaptive optics for spherical aberration correction and motionless focusing*, Journal of microscopy **237**, 136 (2010).
- [56] D. Débarre, E. J. Botcherby, T. Watanabe, S. Srinivas, M. J. Booth, and T. Wilson, *Image-based adaptive optics for two-photon microscopy*, Optics letters **34**, 2495 (2009).

- [57] N. Ji, D. E. Milkie, and E. Betzig, *Adaptive optics via pupil segmentation for high-resolution imaging in biological tissues*, *nature methods* **7**, 141 (2009).
- [58] J. W. Cha, J. Ballesta, and P. T. So, *Shack-hartmann wavefront-sensor-based adaptive optics system for multiphoton microscopy*, *Journal of biomedical optics* **15**, 046022 (2010).
- [59] M. Shaw, K. O'Holleran, and C. Paterson, *Investigation of the confocal wavefront sensor and its application to biological microscopy*, *Optics express* **21**, 19353 (2013).
- [60] H. Song, R. Fraanje, G. Schitter, H. Kroese, G. Vdovin, and M. Verhaegen, *Model-based aberration correction in a closed-loop wavefront-sensor-less adaptive optics system*, *Optics express* **18**, 24070 (2010).
- [61] O. Azucena, J. Crest, S. Kotadia, W. Sullivan, X. Tao, M. Reinig, D. Gavel, S. Olivier, and J. Kubby, *Adaptive optics wide-field microscopy using direct wavefront sensing*, *Optics letters* **36**, 825 (2011).
- [62] X. Tao, B. Fernandez, O. Azucena, M. Fu, D. Garcia, Y. Zuo, D. C. Chen, and J. Kubby, *Adaptive optics confocal microscopy using direct wavefront sensing*, *Optics letters* **36**, 1062 (2011).
- [63] J. Antonello, M. Verhaegen, R. Fraanje, T. van Werkhoven, H. C. Gerritsen, and C. U. Keller, *Semidefinite programming for model-based sensorless adaptive optics*, *JOSA A* **29**, 2428 (2012).
- [64] J. Antonello, T. van Werkhoven, M. Verhaegen, H. H. Truong, C. U. Keller, and H. C. Gerritsen, *Optimization-based wavefront sensorless adaptive optics for multiphoton microscopy*, *JOSA A* **31**, 1337 (2014).
- [65] C. Bourgenot, C. D. Saunter, J. M. Taylor, J. M. Girkin, and G. D. Love, *3d adaptive optics in a light sheet microscope*, *Optics express* **20**, 13252 (2012).
- [66] T. J. Gould, D. Burke, J. Bewersdorf, and M. J. Booth, *Adaptive optics enables 3d sted microscopy in aberrating specimens*, *Optics express* **20**, 20998 (2012).
- [67] J.-H. Park, W. Sun, and M. Cui, *High-resolution in vivo imaging of mouse brain through the intact skull*, *Proceedings of the National Academy of Sciences* **112**, 9236 (2015).
- [68] R. D. Simmonds and M. J. Booth, *Modelling of multi-conjugate adaptive optics for spatially variant aberrations in microscopy*, *Journal of Optics* **15**, 094010 (2013).
- [69] J. Mertz, H. Paudel, and T. G. Bifano, *Field of view advantage of conjugate adaptive optics in microscopy applications*, *Applied optics* **54**, 3498 (2015).

- [70] B. C. Platt and R. Shack, *History and principles of shack-hartmann wavefront sensing*, *Journal of Refractive Surgery* **17**, S573 (2001).
- [71] J. Li, D. R. Beaulieu, H. Paudel, R. Barankov, T. G. Bifano, and J. Mertz, *Conjugate adaptive optics in widefield microscopy with an extended-source wavefront sensor*, *Optica* **2**, 682 (2015).
- [72] R. Ragazzoni, *Pupil plane wavefront sensing with an oscillating prism*, *Journal of modern optics* **43**, 289 (1996).
- [73] R. W. Wilson, *Slodar: measuring optical turbulence altitude with a shack-hartmann wavefront sensor*, *Monthly Notices of the Royal Astronomical Society* **337**, 103 (2002).
- [74] H. Yang, O. Soloviev, and M. Verhaegen, *Model-based wavefront sensorless adaptive optics system for large aberrations and extended objects*, *Optics express* **23**, 24587 (2015).
- [75] D. Wilding, P. Pozzi, O. Soloviev, G. Vdovin, R. Fiolka, and M. Verhaegen, *Hybrid adaptive and computational light-sheet fluorescence microscopy*, (2018) pp. 10502 – 10502 – 7.
- [76] D. Débarre, M. J. Booth, and T. Wilson, *Image based adaptive optics through optimisation of low spatial frequencies*, *Optics Express* **15**, 8176 (2007).
- [77] P. A. Santi, *Light sheet fluorescence microscopy a review*, *Journal of Histochemistry & Cytochemistry* **59**, 129 (2011).
- [78] S. Bonora, Y. Jian, P. Zhang, A. Zam, E. N. Pugh, R. J. Zawadzki, and M. V. Sarunic, *Wavefront correction and high-resolution in vivo oct imaging with an objective integrated multi-actuator adaptive lens*, *Optics express* **23**, 21931 (2015).
- [79] *Flexible optical b.v.* <https://www.okotech.com><https://www.okotech.com>, accessed: 2018-02-24.
- [80] *Alpao*, <https://www.alpao.com/><https://www.alpao.com/>, accessed: 2018-02-24.
- [81] *Boston micromachines corportation*, <https://www.bostonmicromachines.com/><https://www.bostonmicromachines.com/>, accessed: 2018-02-24.
- [82] *Meadowlark optics*, <https://www.meadowlark.com/><https://www.meadowlark.com/>, accessed: 2018-02-24.
- [83] *Dynamic optics*, <http://www.dynamic-optics.eu/><http://www.dynamic-optics.eu/>, accessed: 2018-02-24.
- [84] J. Fienup and J. Miller, *Aberration correction by maximizing generalized sharpness metrics*, *JOSA A* **20**, 609 (2003).

- [85] P. Pozzi, D. Wilding, O. Soloviev, G. Vdovin, and M. Verhaegen, *Adaptive optics in digital micromirror based confocal microscopy*, in *SPIE BiOS* (International Society for Optics and Photonics, 2016) pp. 971706–971706.
- [86] M. A. Vorontsov, *Decoupled stochastic parallel gradient descent optimization for adaptive optics: integrated approach for wave-front sensor information fusion*, *JOSA A* **19**, 356 (2002).
- [87] M. Vorontsov, G. Carhart, and J. Ricklin, *Adaptive phase-distortion correction based on parallel gradient-descent optimization*, *Optics letters* **22**, 907 (1997).
- [88] R. Fletcher, *Practical methods of optimization* (John Wiley & Sons, 2013).
- [89] G. Vdovin, P. Sarro, and S. Middelhoek, *Technology and applications of micro-machined adaptive mirrors*, *Journal of Micromechanics and Microengineering* **9**, R8 (1999).
- [90] L. Blied, H. R. Verstraete, M. Verhaegen, and S. Wahls, *Online optimization with costly and noisy measurements using random fourier expansions*, *IEEE transactions on neural networks and learning systems* (2017).
- [91] P. Pozzi, D. Wilding, O. Soloviev, H. Verstraete, L. Blied, G. Vdovin, and M. Verhaegen, *High speed wavefront sensorless aberration correction in digital micromirror based confocal microscopy*, *Optics Express* **25**, 949 (2017).



2

Shaping the Illumination

*Research is what I'm doing when
I don't know what I'm doing.*

Wernher von Braun

Chapter Abstract

Pupil filters, represented by binary phase modulation, have been applied to extend the field of view of a light-sheet fluorescence microscope. Optimisation has been used first numerically to calculate the optimum filter structure, and then experimentally, to scale and align the numerically synthesized filter in the microscope. A significant practical extension of the field of view has been observed, making reported approach a valuable tool on a path to wide-field light-sheet microscopy.

This chapter has been published in *Pupil filters for extending the field-of-view in light-sheet microscopy*, Optics Letters **41**, 6 (2016) [1].

2.1. Introduction

Light-sheet (LS) microscopy [2, 3] achieves optical sectioning in specimens by forming a thin LS in the plane orthogonal to the optical axis of an imaging microscope. An ideal LS should be very thin, as the thickness of the LS defines the axial resolution. As an additional requirement the thickness and intensity of the LS should both be kept as uniform as possible over the field-of-view (FOV). The LS should be wide and long enough to cover the whole FOV of the microscope.

In practice, however, the parameters of the LS are governed by laws of diffraction and scattering in the specimen, and therefore, the ideal parameters are hardly ever achieved. The optimisation of these parameters for a LS is of interest for a number of practical applications in biomedical imaging [4]. There has been much work done on the enhancement of the LS, this includes the creation of scanned Bessel beams [5], Airy beams [6], and aspheric optical systems [7].

In all such approaches the goal is a redistribution of the light field that enables the light to propagate with a lower divergency in the vicinity of the focus. The theoretically optimum solution in three-dimensions is the infinite energy Bessel beam [8], and its two-dimensional equivalent the cosine beam [9]. In practice, the Bessel beam cannot be produced; however, hybrids of these beams with the Gaussian beam can be obtained [10]. The weakness of all of these beam engineering techniques are the strengthening of the subsidiary side lobes that decrease the optical sectioning ability in the LS microscope; this can be reduced by deconvolution post-processing [6], but it still remains a limiting factor.

2.2. Binary pupil filters

It was shown by Shepherd in [11] that a symmetric binary pupil filter (PF) can be used for maximizing the extension of a two-dimensional LS formed by a cylindrical lens with a band structure of $0 \vee \pi$ phase shifts. The band positions are symmetrical with respect to the optical axis of the lens, but have no rotational symmetry.

The PF solutions could theoretically out-perform the Gauss-Bessel beams [11], therefore, this is calling for experimental verification. The generalization of this technique to complex pupil functions could allow for the additional correction and compensation of aberrations introduced by the sample and is an active area of our research. Since our hope is to show that PFs can provide an alternative to expensive adaptive elements we have limited our scope.

In Figure 5.1 the structure of the PF is shown alongside the cylindrical element that forms the LS. The PF considered in this chapter have N symmetric elements with $M = (N - 1)/2$ step changes in the phase as the half-aperture is traversed. Following the same notation as in [11], these parameters are called m_i 's, $i = 1, \dots, M$, the normalized pupil coordinates at which the step change occurs.

For clarity of explanation Figure 2.2 shows the schematic of the geometry of the LS microscope system. The orthogonal detection of the light in the illumination path and the fluorescence path are shown. The coordinate system represented in the Figure

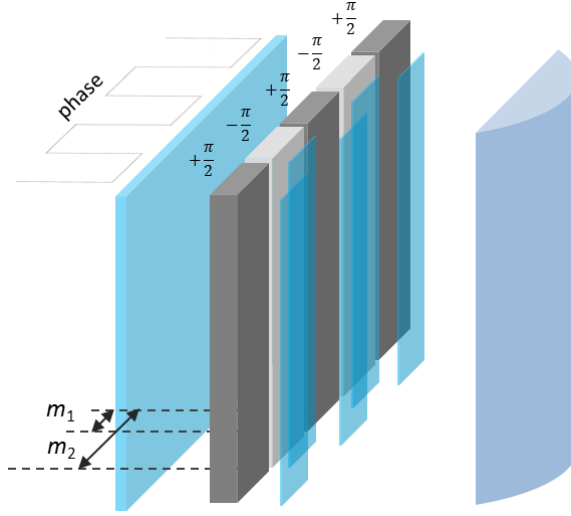


Figure 2.1: A schematic showing the realization of pupil filters in a LS microscope. The field is modulated by the introduction of π phase differences before a cylindrical phase element in the pupil. By controlling the shape of the band structure the focal intensity distribution is changed.

is used throughout the text.

2.3. Optimising the filters

The solutions to the wave equation for elements up to $N = 7$ are presented in Table 1 of [11]; however, to find the solutions for $N > 7$ requires an ever increasing amount of time by brute force. Hence it is highly desirable to find the solutions via more time efficient numerical optimisation techniques. Moreover, in order to implement these PFs on the experimental system it is necessary to calibrate the m_i 's to further improve the parameters of LS.

Optimisation is finding the minimum of a cost or objective function that represents a physical measure as functions of decision variables. Concretely, in [11] a parameter G_A is proposed with its decision variables m_i 's. It is a measure of the axial point-spread function and is derived from the analysis of the pupil field moments, however, it is impossible to apply this metric to the experimental setup.

To overcome this, a new metric, one that can be experimentally measured is proposed in this chapter. Measurements of the focal field are taken at K positions along the optical axis giving peak intensities I_k . Typically, it was found that $K = \mathcal{O}(M)$ is sufficient. The root mean square deviation from the maximum focal intensity is then calculated:

$$\text{r.m.s.} = \rho = \sqrt{\frac{1}{K} \sum_{k=0}^K (I_k - \max(I_k))^2} \quad (2.1)$$

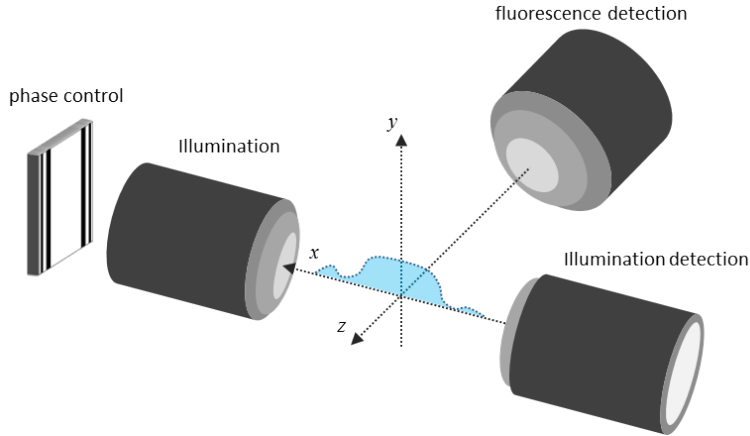


Figure 2.2: The axes configuration in the focal plane for the detection of illumination light and fluorescence light. The light enters from the left via the phase element and is focused along the xy -plane. Depth is with respect to the fluorescence objective.

The PF solution that provides good LS parameters forms a flat intensity profile around the focus along the optical axis. This implies the curvature of the intensity field is minimized, i.e. $G_A \rightarrow 0$. Therefore, the optimal PF solution, \mathbf{m}^* , that minimizes the deviation from peak intensity, ρ , over a given range Δ is what is desired.

The problem can be written as,

$$\begin{aligned} \min_{\mathbf{m}} \rho(\mathbf{m}, \Delta) \\ \text{s.t. } m_i + \delta < m_{i+1} \end{aligned} \quad (2.2)$$

where $\mathbf{m} \in \mathbb{R}^{(N-1)/2}$ are the optimisation variables. δ is the width of a Fresnel zone in the pupil. Although modest in dimension for a small number of elements, the problem is not trivial to solve. The objective function is non-convex and has a number of local minima, although, it is a simpler problem than the minimization of G_A due to the numerical instability of the metric. Furthermore, as the number of dimensions is expanded, the number of non-optimal local minimizers increases.

These local minima arise due to the complex interference interactions between different regions in the pupil. For example, it is possible for the positioning of two of the zones to provide a net effect of zero to the field. Hereby, the numerical procedure for example can find the $N = 3$ solution in all higher dimensions with increasing permutations. For this reason the value of Δ becomes a very important tuning parameter in the optimisation, too high and the solution will not exist and too low the number of non-global minima increases slowing the process.

The global optimisation is performed with a custom algorithm written by the authors that uses a stochastic gradient descent [12] to converge to multiple minima simultaneously. Each group of solutions is evaluated on the strength of the group's

weighted mean or centroid rather than the individuals to increase robustness against noise.

2.4. Numerical simulation and experimental results

In Figure 2.3 the x -profiles for the PF solutions for $N = 1, 3, \dots, 11$ found in the simulated environment are shown. The simulated fields are obtained with Fresnel propagation within the approximations of scalar diffraction theory [13]. The main result shown is that increasing the value of N increases the axial extend of the PSF, likewise, it increases the lateral extent also but less than simply increasing the numerical aperture (NA). This was shown in [11] for $N = 3, \dots, 7$ and it has been extended to $N = 11$ here.

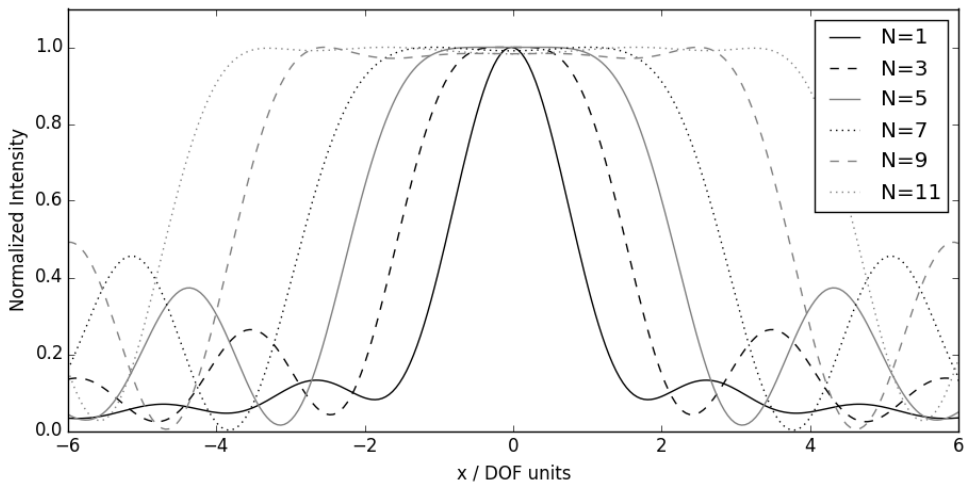


Figure 2.3: Simulations of the intensity profile along the x -axis. Increasing the number of elements in the pupil filter increases the axial extend of the PSF and therefore, increases the uniformity over the FOV in a LS microscope. The intensity is normalized in this plot.

The problem is more complicated experimentally due to the noise introduced in the intensity measurements, therefore, it was impossible to consistently find the solution to the global optimisation on the experimental setup.

To overcome this a two-stage optimisation process was required to consistently find the solution. Firstly, the global optimum is found via simulation with the advantage of no measurement noise. Secondly, this solution is locally optimised on the experimental system to correct for pupil matching, system aberrations and differences in magnification.

This can be done since in a region close to the theoretical global minimum the cost function is quasi-convex. The local optimisation can proceed using a noise robust algorithm [14]. This process converges to the new minimum within a few iterations, typically under 25. Here the pupil phase, $\phi(\mathbf{m})$ is optimised with $\mathbf{c} \in \mathbb{R}^2$ such that the

new phase $\phi'(\mathbf{m})$ is:

$$\phi'(\mathbf{m}) = c_0\phi(c_1\mathbf{m}) \quad (2.3)$$

2

The LS microscope has been realized with a liquid crystal phase-only spatial light modulator (SLM) (512x512, Meadowlark/Boulder, US) conjugated to the pupil of a NA= 0.3 water immersion illumination objective (UMPLFLN 10x Olympus, Japan). Such a configuration allows for the forming arbitrary pupil functions with high resolution; however, in this chapter the scope of possible solutions are limited to the class described in [11].

A 488nm laser source (100mW Sapphire 488nm LP, Coherent, US) illuminates the PF generated by the SLM and is conjugated with the pupil plane of the illumination objective mounted in a custom water immersion sample chamber. The measurements of the objective function are obtained through a confocal objective (UMPLFLN 10x Olympus, Japan) onto CMOS camera (DCC1545M, Thorlabs, US). This is done at different values of defocus by modulating the phase on the SLM. A full intensity profile can also be imaged in the same manner by sweeping through a volume.

In Figure 2.4 the x-axis profile of the intensity for the optimised experimental PFs are shown for $N = 1, \dots, 11$. A good match between the theoretical prediction in Figure 2.3 and the experimental results is found, thus confirming the validity of the PF theory and its practical usefulness.

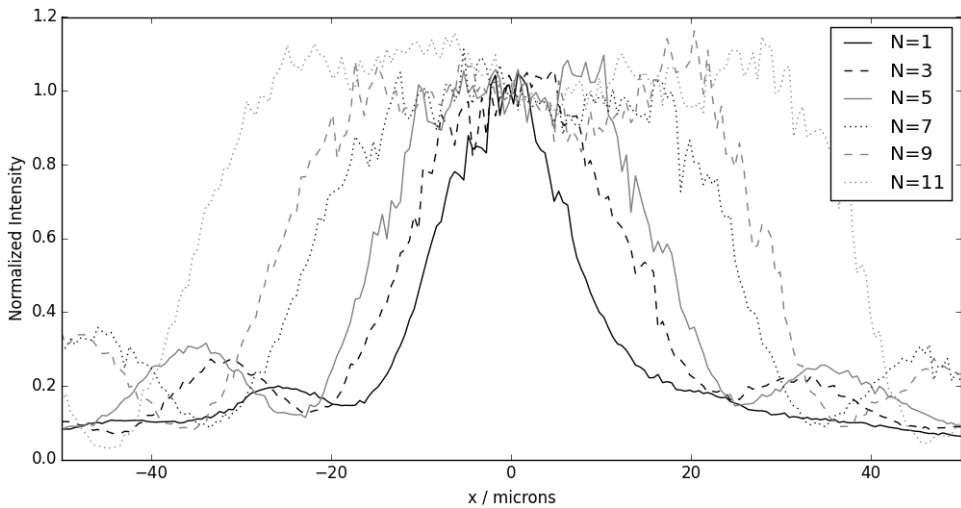


Figure 2.4: Experimental plots of the intensity profile along the x-axis. In agreement with the simulations increasing the number of elements in the pupil filter increases the axial extend of the PSF. The plots are normalized to the mean intensity in a $5\mu\text{m}$ central region.

Increasing the number of elements in the BFP increases the depth-of-field (DOF) whilst decreasing the focal intensity. For discussion, in Figure 2.5 the xz-intensity of

the $N = 11$ optimised filter shown alongside the Gaussian beam and the numerical solution directly applied.

The first point to note is the improvement gained by the optimisation procedure in the uniformity of the beam over the region. The numerical solution does not have the long uniform region over the FOV, but falls off after the focus, however, this is recovered by the optimisation process. The PF must be matched to the pupil scale and the wavelength to gain optimal performance. The optimisation ensures that both of these conditions are satisfied by scaling in size and amplitude. The π phase difference ensures a real pupil function giving the symmetry in the yz -plane seen in the optimised solution but which is missing in the unoptimised solution.

Measuring the full-width at half maximum (FWHM) for the $N = 11$ filter shows a 4.2x increase in the DOF for a 1.6x increase in lateral PSF width. This is a better ratio than decreasing the NA 2.6x, and thus DOF extension has been achieved. In addition to this, the intensity is uniform over the central region, something that cannot be said about Gaussian or Gauss-Cosine beams. As a result there is a region of $70\mu\text{m}$ that has a uniform intensity LS, this should in theory provide over this region better imaging than these other beam profiles.

To further test this hypothesis, experimental investigation of the performance of the PF enhanced LS has been conducted by acquiring three dimensional volumes of fluorescent microspheres. The purpose is to measure the resolution of the microscope across the FOV. The axial PSF of the beads over the FOV varies according to the thickness of the LS at that position. The PFs designed to increase the LS extent whilst retaining lateral thickness is expected to improve the axial resolution towards the edges of the FOV.

The fluorescence image of the microsphere sample is captured via a relay system and a deformable mirror (DM69, Alpao, France) for focus change and detection, to scientific CMOS camera (Orca Flash 4, Hamamatsu Photonics, Japan). This configuration allows for full control of the LS and image focus for three-dimensional imaging and sectioning of the sample.

In order to obtain sufficient sampling the z -scan is done using the DM in conjunction with the SLM. The system is calibrated such that plane of the LS and the focal plane of the detection objective are matched. The calibration procedure uses a sharpness-based optimisation [15] to find the optimum defocus position at two known LS positions and form a linear model valid over the range of the defocus. Hereafter the focus of the detection objective and the LS remain coplanar.

The beam is scanned through a volume of the sample to produce a series of optically sectioned xy images at different z positions. This three-dimensional dataset can then be computationally processed and viewed from arbitrary angles, of which the orthogonal set xz is chosen. In Figure 2.6 the maximum intensity projections over small y -range is shown for the $N = 11$ optimised beam, along with the Gaussian and for reference a Gauss-Cosine beam.

This series of images show that the PF increases the uniformity of the resolution and intensity over the extension region compared with the Gaussian and Gauss-Cosine

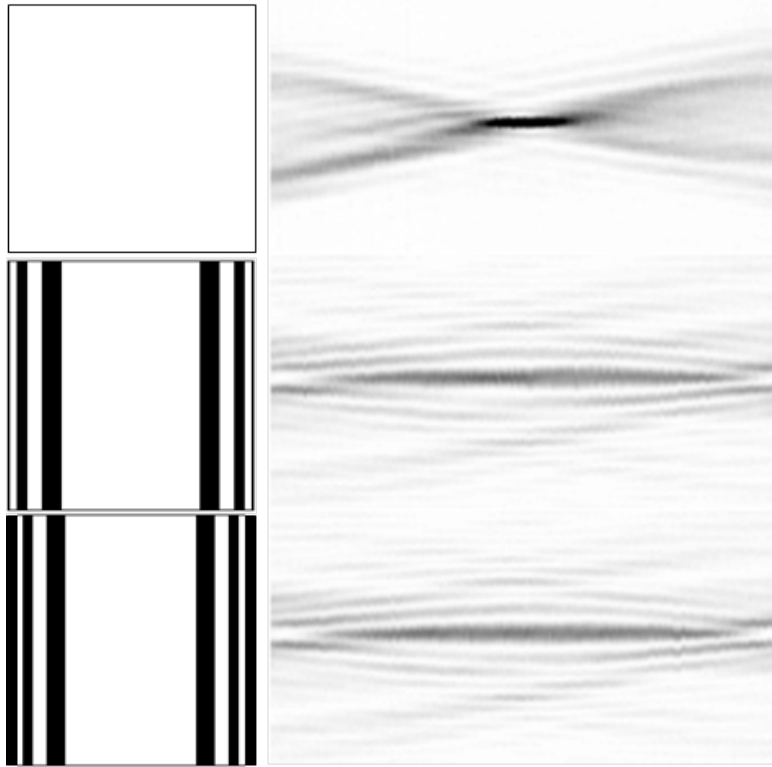


Figure 2.5: Image of xz beam intensity profile produced by the illustrative PFs on the left. From the top the Gaussian, the numerical solution solution for $N = 11$ and the optimised solution for $N = 11$. The region displaced for each PSF is $100 \times 18\mu\text{m}$. There is no normalization of intensity.

beam as expected. Outside of the $50\mu\text{m}$ central region double and triple PSFs are observed consistent with the intensity profile shown in Figure 2.5.

The image contrast and the resolution in the centre is decreases as a natural consequence of the extension of the DOF. The peak power decreases as N is increased such that the peak intensity for $N = 11$ is a third of the original Gaussian power. The reason for this is both the lateral spreading of the PSF and redistribution of spatial frequencies, that is greater energy in side-lobes. The power in the centre is decreased but the variance of the intensity across the FOV is minimized.

2.5. Discussion

Binary pupil filters, therefore, are a simple and cost effective solution to the extension of the useful FOV in a LS microscope. The computation of the PF that provides a LS with optimal parameters is possible for large number of elements via numerical optimisation. This allows for the design of filters with a long flat focus and therefore, a wide FOV for the LS microscope. Whilst it is possible, if not time consuming, to

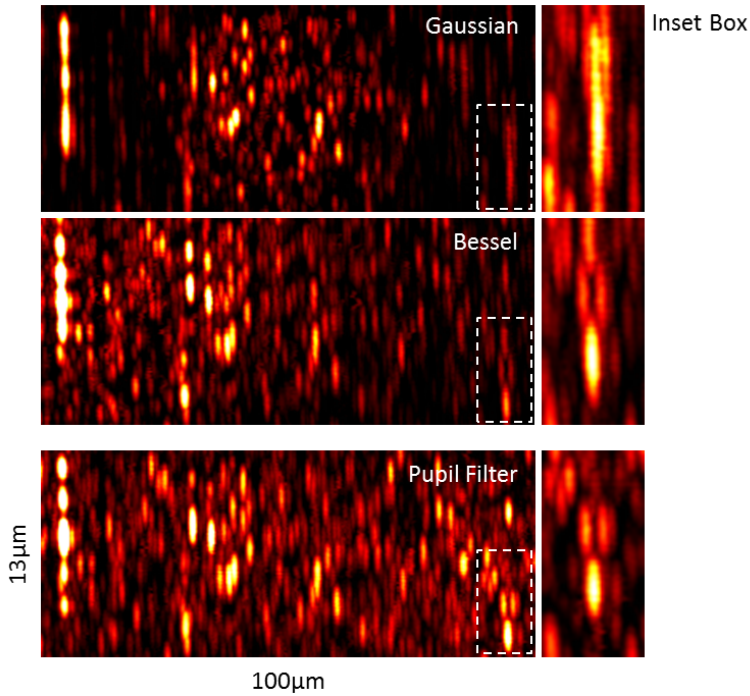


Figure 2.6: Microspheres xz -profile with a Gaussian beam, a Bessel beam, and a PF $N = 11$. Same imaging parameters, normalized to central bead intensity. The inset shows a zoom of beads at a distance of 25μ from the focus of the light-sheet.

calculate the solutions for greater values of N at some point the reduction in peak power and increasing power in the side-lobes reduces the usefulness the PFs for imaging.

It has been shown how these PFs are found by a two stage process of numerical optimisation, one to find the global solution via simulation and the second to find the local improvement on an experimental system. The profiles of the light intensity and their effect on the resolution of the microscope has been demonstrated.

It has been shown that the PFs produce a symmetric PSF along two axes owing to the real pupil function. This particular feature of PFs is not found in many other DOF extension methods such as the Gauss-Bessel beam or the Airy beam. It should be possible to exploit this symmetry to reduce the complexity in deconvolution calculations commonly employed in LS microscopy.

Finally, the PFs' theoretical advantage over the Gauss-Cosine or Gauss-Bessel beam has been shown experimentally, and since they do not require annuli for generation, more power can be delivered to the sample with the same source. Moreover, PFs could be manufactured as phase masks designed to fit particular microscope objectives. As a result the extended FOV could be realized with a much simpler, cheaper and durable system than presently available.

References

- [1] D. Wilding, P. Pozzi, O. Soloviev, G. Vdovin, C. J. Sheppard, and M. Verhaegen, *Pupil filters for extending the field-of-view in light-sheet microscopy*, *Optics letters* **41**, 1205 (2016).
- [2] A. Voie, D. Burns, and F. Spelman, *Orthogonal-plane fluorescence optical sectioning: Three-dimensional imaging of macroscopic biological specimens*, *Journal of microscopy* **170**, 229 (1993).
- [3] J. Huisken, J. Swoger, F. Del Bene, J. Wittbrodt, and E. H. Stelzer, *Optical sectioning deep inside live embryos by selective plane illumination microscopy*, *Science* **305**, 1007 (2004).
- [4] P. A. Santi, *Light sheet fluorescence microscopy a review*, *Journal of Histochemistry & Cytochemistry* **59**, 129 (2011).
- [5] T. A. Planchon, L. Gao, D. E. Milkie, M. W. Davidson, J. A. Galbraith, C. G. Galbraith, and E. Betzig, *Rapid three-dimensional isotropic imaging of living cells using bessel beam plane illumination*, *Nature methods* **8**, 417 (2011).
- [6] T. Vettenburg, H. I. Dalgarno, J. Nytk, C. Coll-Lladó, D. E. Ferrier, T. Čížmár, F. J. Gunn-Moore, and K. Dholakia, *Light-sheet microscopy using an airy beam*, *Nature methods* **11**, 541 (2014).
- [7] S. Saghafi, K. Becker, C. Hahn, and H.-U. Dodt, *3d-ultramicroscopy utilizing aspheric optics*, *Journal of biophotonics* **7**, 117 (2014).
- [8] J. Durnin, J. Miceli Jr, and J. Eberly, *Diffraction-free beams*, *Physical Review Letters* **58**, 1499 (1987).
- [9] L. W. Casperson, D. G. Hall, and A. A. Tovar, *Sinusoidal-gaussian beams in complex optical systems*, *JOSA A* **14**, 3341 (1997).
- [10] C. Sheppard and T. Wilson, *Gaussian-beam theory of lenses with annular aperture*, *IEE Journal on Microwaves, Optics and Acoustics* **2**, 105 (1978).
- [11] C. J. Sheppard, *Pupil filters for generation of light sheets*, *Optics express* **21**, 6339 (2013).
- [12] P. Wolfe, *Convergence conditions for ascent methods*, *SIAM review* **11**, 226 (1969).
- [13] J. W. Goodman, *Introduction to Fourier optics* (Roberts and Company Publishers, 2005).
- [14] H. R. G. W. Verstraete, S. Wahls, J. Kalkman, and M. Verhaegen, *Model-based sensor-less wavefront aberration correction in optical coherence tomography*, *Optics Letters* (2015).

- [15] R. A. Muller and A. Buffington, *Real-time correction of atmospherically degraded telescope images through image sharpening*, JOSA **64**, 1200 (1974).



3

Correcting the Illumination

*Success is not final, failure is not fatal:
it is the courage to continue that counts.*

Winston Churchill

Chapter Abstract

A methodology for the adaptive control and correction of phase aberrations in the illumination arm of a light-sheet fluorescence microscope has been developed. The method uses direct wavefront sensing on epi-fluorescent light to detect the aberration present in the sample. Using this signal, the aberrations in the illumination arm are subsequently corrected with a spatial light modulator in a feedforward mode. Adaptive correction, resulting in significant improvement in the axial resolution, has been demonstrated by imaging *Tg(fli:GFP)* zebrafish embryos.

This chapter has been published in *Adaptive illumination based on direct wavefront sensing in a light-sheet fluorescence microscope*, Optics Express **24**, 22 (2016) [1].

3.1. Introduction

Light-sheet fluorescence microscopy (LSFM) is a microscopy technique that delivers wide-field optically sectioned images at high acquisition rates by splitting the illumination and detection of the fluorescence light into two orthogonal arms [2, 3]. One of the most common uses of the LSFM is to image embryos and organs, that tend to be in microscopic terms: thick, optically inhomogeneous and scattering samples.

As a result, LSFM suffers strongly from phase aberrations in both of its optical arms leading to a reduction in imaging quality. The aberrations in the imaging arm reduce the resolution of the resulting image. The aberrations in the illumination arm act in a more complicated manner. The effect of these aberrations changes over the field and can create strong non-uniformity in the illumination, slicing selectivity and image brightness over the image. Whilst correction of the phase aberrations in the imaging arm has been previously demonstrated [4], the problem of the correction in the illumination arm has yet to be solved. The reason for this is that there is currently no method for sensing the sample induced aberrations such that the light-sheet can be shaped to compensate for them. In this chapter, a solution to the sensing and correction of these phase aberrations is presented. *Direct wavefront sensing* [5] on the fluorescent light emitted back in the direction of the source allows the optimal shape of the light-sheet to be found by utilizing a feedforward adaptive optics (AO) control system. This direct sensing is based on data from a Shack-Hartmann wavefront sensor [6] incorporated in an easily constructed epi-fluorescence arm. Once this aberration is known it can be corrected by applying the scaled conjugate phase to a spatial light modulator (SLM) controlling the illumination light.

This methodology is a departure from currently used methodologies where these aberrations are reduced by either chemically clearing the sample [7] or using biologically engineered organisms [8] to improve their optical quality. Whilst other approaches have modified the illumination of the microscope, they have not concentrated on correcting these aberrations, but rather using more complex methodologies that are less affected by them. They can be broadly grouped as methods changing the physical properties of the beam [9], the fusing of multiple datasets [3], or applying deconvolution [10] as means to improve the overall imaging result.

The drawback of these existing techniques is that aberrations are still present and it is necessary to infer the fluorescence signal, because it cannot be directly observed. Aberrations imply that fluorescence is in fact generated outside of the assumed sectioned plane, resulting in an increase in the background signal, a reduction in the signal-to-noise ratio, and features appearing in planes where they are not truly present.

To remove these spurious features the dataset must be deconvolved using its three-dimensional spatially variant point-spread function (PSF). Here noise corruption and the necessity to estimate the PSF over the field-of-view dictate that the output be an inference. Adaptive optics could allow for the correction of these phase aberrations, therefore, giving the direct observation of the fluorescence signal from the desired plane with no need for inference or extra post-processing.

3.2. Methodology for Feedforward Control

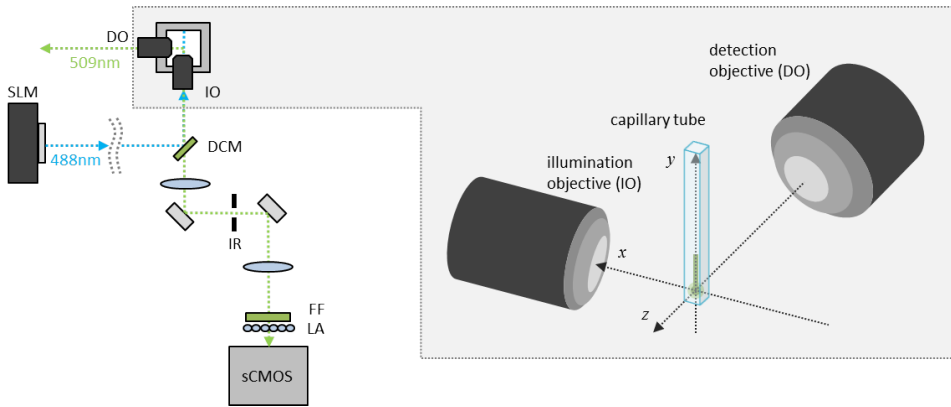


Figure 3.1: A schematic representation of the optical system showing the major optical components for the addition of the sensor to the microscope design. The light from the spatial light modulator (SLM) is conjugated via the dichroic mirror (DCM) onto the illumination objective (IO). The light focuses into the sample that gives off uniform fluorescence into 4π steradians. The fluorescence is captured in two paths, one through the detection objective (DO) and onto the camera for imaging; and epi-fluorescently through the IO via an optical relay to the wavefront sensor composed of a fluorescence filter (FF), a lenslet array (LA) and sCMOS camera. The iris (IR) allows the regulation of the spot sizes on the sensor. For explanatory purposes the orientation of the coordinate axes for the LSFM are shown on the right.

Adaptive optics has three main steps: wavefront sensing, reconstruction and correction. AO has been implemented in microscope systems in one of two ways [11]. One method, “direct sensing”, uses a device known as a wavefront sensor (WFS), which provides a signal that can be related to the spatiotemporal variation of the phase in a particular plane of the optical system. The strongest advantage for using a sensor is its speed and this is often necessary when the phase aberration has fast temporal dynamics; however, it generally applies constraints to what can be imaged (e.g. only point-sources), it can lead to anisoplanatic correction depending on the type of aberration, and it requires photons that could be used for imaging.

The second method, “indirect sensing” or “indirect optimisation”, uses an optimization procedure to iteratively improve the quality of the images. This second technique is known as sensor-less AO and is typically used in microscopy systems where the photon budget is low, or the object constraints for the sensor are not met. The advantage is that it can be always implemented with a suitable metric, however, if N is the number of modes used for the corrective element then the minimum number of steps to correct the aberration is $N + 1$ [12], this leads to a lengthy and costly imaging process.

To sense the aberration in the illumination path, it was decided to use direct wavefront sensing, and since the back-scattered coherent illumination light would produce a speckle field at the wavefront sensor, the incoherent epi-fluorescent light was cho-

sen to sense the aberration. It should be noted that the fluorescence light emitted orthogonally to the illumination is used for imaging, therefore, no light normally used for imaging is lost to sense and correct the aberration, see Fig. 5.1 for the layout of the experimental system.

3 A point-source in the centre of the microscope FOV in free space would produce a flat wavefront in the pupil plane of the illumination objective. Hence, by adding a wavefront sensor conjugated with this pupil plane it is possible to sense the phase aberration acquired in the optical path on the way out of the sample. By Babinet's principle the illumination light will acquire the same phase aberration, scaled by the wavelength, on its way into the sample. Shaping the incident light with the conjugate aberration will, therefore, recover a point-source. A further advantage of this approach is if the illumination is restored to a Gaussian focus, then by definition, it cannot diverge faster from the focus. As a result any subsequent aberrations in the path will produce a light-sheet that is thinner, thus also increasing the axial resolution at the far side of the sample.

Unfortunately, LSFM is generally used to image extended sources and therefore, no point-source at the centre of the FOV is normally present. Whilst it would be possible to introduce so called 'guide stars' [13], practically this would be difficult to implement and could interfere with biological processes. It is possible, however, to locate a region of fluorescence in a sample at the centre of the FOV. When a *beam* is used for illumination instead of a light-sheet, that is the cylindrical defocus is removed, fluorescence is generated throughout the Gaussian point-spread function (PSF) of the optical system.

With this extended incoherent source, the wavefront sensor reconstructs a weighted average of the anisoplanatic aberrations, that have been introduced by the sample in the vicinity of focal region, and the isoplanatic aberration of the system, including the pupil aberration and, to some extent, the aberration caused by the sample. The final correction from this sensor will be efficient because in a practical system the isoplanatic low-order component has a considerable weight. Moreover, the wavefront corrector conjugated to the system pupil plane is only capable of correction of this isoplanatic component of the aberration field.

A Shack-Hartmann wavefront sensor can be conjugated to this pupil plane showing an array of PSFs, or *spots* created by its lenslet array. The conventional procedure of wavefront correction by minimizing spot shifts from a known flat reference is not applicable for the case in discussion. The reason for this is that the epi-fluorescent light does not pass back via the corrector; even if it did, it is of the wrong wavelength and polarisation to have the desired effect. The system as a result can sense the aberration, but it cannot detect the effect of its own correction on the wavefront. It must instead operate in a blind single step feedforward mode, where the only means of verification of aberration correction is in the improvement found in a three-dimensional acquisition.

Following the usual procedure for this type of control, the spot displacements in each of the sub-apertures are linearly related to a modal decomposition of the wavefront

in Zernike polynomials Z_n , where n is the Noll index. The stacked spot displacement vector \mathbf{s} can be linearly related via the sensor geometry matrix G to the vector of Zernike coefficients \mathbf{z} by:

$$\mathbf{s} = G\mathbf{z}. \quad (3.1)$$

To find the spot displacements \mathbf{s} requires knowledge of the flat wavefront reference position \mathbf{r} . The current measured centres \mathbf{c} and the reference centres \mathbf{r} are related to the displacement by the following expression: $\mathbf{s} = \mathbf{c} - \mathbf{r}$. The reference spot positions, therefore, must be found before the control methodology can be applied. In this case, it is desirable to have a source in the centre of the FOV that has the similar properties as those found in the samples one desires to image (i.e. partially extended, same wavelength and intensity). Thus, a uniformly fluorescent medium of the correct wavelength and concentration is the most directly comparable.

Once \mathbf{s} is calculable the inverse relationship of Eq.3.1 is required, and since G is often not invertible, the Moore-Penrose left pseudo-inverse is used to define the Zernike coefficients at the sensor given the spot displacements:

$$\mathbf{z} = (G^T G)^{-1} G^T \mathbf{s}. \quad (3.2)$$

The same Zernike polynomial modes Z_n are used for controlling the phase on the spatial light modulator (SLM), and once the wavefront reconstruction is done its conjugate is applied to the SLM. The vector of phases for every pixel φ^{SLM} is related to the sum of the Zernike polynomials at its position \mathbf{z}^{SLM} by the following mathematical relationship:

$$\varphi^{\text{SLM}} = \Phi \mathbf{z}^{\text{SLM}}, \quad (3.3)$$

where Φ is a matrix that contains the value of the Zernike polynomials at the pixel positions. Due to various scaling factors including the wavelength and the aperture sizes, it is important to note that the Zernike coefficients from the sensor are related to the coefficients for the SLM by a scaling factor β :

$$\mathbf{z}^{\text{SLM}} = \beta \mathbf{z}. \quad (3.4)$$

Although β is theoretically calculable, it is better to make an experimental measurement. As previously mentioned the WFS is generally insensitive to the corrective phase, however, it is not completely and it is possible to make use of the translational Zernike modes (tip, tilt and defocus) for this purpose. As these modes correspond to the movement of the focal spot in three dimensions, the WFS is sensitive to their application on the SLM and β can be measured.

The ratios between applied Zernike coefficient on the SLM and the measured coefficient on the WFS for each of the translation modes are averaged together. With β now known, the corrective phase $\hat{\varphi}^{\text{SLM}}$ applied to the SLM can be directly related to the spot displacements on the sensor by:

$$\hat{\varphi}^{\text{SLM}} = -\beta \Phi (G^T G)^{-1} G^T \mathbf{s}. \quad (3.5)$$

where the whole expression has been multiplied by -1 to affect the correction of the phase aberration. The control procedure is, in summary: measure the spot displacements using a beam, rather than a light-sheet; then reconstruct the wavefront using the modal decomposition; finally, apply the conjugate and scaled phase to the corrective element. After this step, one can return the system to a light-sheet mode and image the sample.

In summary, the main reason for the use of the feedforward control strategy is that it is not possible to image the laser line directly in an aberrating sample and obtain feedback. While this methodology senses and corrects the aberration introduced between the objective lens and the focal plane, any images of the shape of the light-sheet itself would be affected by a different aberration, which could not be corrected by the wavefront corrector. Even a perfectly corrected light-sheet would, therefore, appear aberrated if imaged directly. For these reasons, it is impossible to image the light-sheet inside an aberrating sample in this optical configuration, thus feedforward control is used.

3

3.3. Experimental Design and Calibration

For the purpose of experimental verification, a light-sheet fluorescence microscope has been realized in the configuration shown in Fig. 5.1, here the illumination is provided by a 488nm laser (100mW Sapphire LP, Coherent Inc., U.S.) followed by polarization optics (WPH10M-488 and GT5-A, Thorlabs, U.S.) to produce linearly polarized light for the following spatial light modulator (SLM) (512x512, Meadowlark Optics, U.S.) with the additional benefit of providing a fixed intensity attenuator.

The light from the SLM is optically conjugated to the back aperture of an NA= 0.3 objective lens (UMPLFLN 10x Olympus, Japan) via a beam expander (AC508-180-A-ML and AC508-200-A-ML, Thorlabs, U.S.) of $1.11\times$ thus utilising the full numerical aperture (NA) of the microscope objective. To form the light-sheet a cylindrical lens pattern is applied to the SLM, thus cancelling the focusing power of the lens in the y -direction, such that it is possible to have a light-sheet across the vertical field-of-view of the detection camera of around $400\mu\text{m}$.

The detection of fluorescence follows the standard LSFM design and is orthogonal to the light-sheet propagation direction. The fluorescence light is conjugated from the NA= 0.5 imaging objective (UMPLFLN 20x Olympus, Japan) to a deformable mirror (DM) (DM69, ALPAO, France), which used for changing the imaging plane in step with the SLM, via a 1:1 telescope (AC508-180-A-ML, Thorlabs, U.S.). The fluorescence at the mirror is then focused onto the imaging camera (Orca Flash v2, Hamamatsu Photonics, Japan) through a fluorescence filter (MF525-39, Thorlabs, U.S.). Hereby, obtaining a optically sectioned image at a desired plane in the sample. Three-dimensional imaging is obtained by scanning the SLM and DM in synchronous motion after a calibration procedure described in the author's previous work [14].

To this base a Shack-Hartmann wavefront sensor (SH-WFS), made of a lenslet array ($300\mu\text{m}$ rectangular array, Flexible Optical B.V., Netherlands) and a camera (UI-3060CP Rev. 2, IDS, Germany) has been added to record the wavefront of the

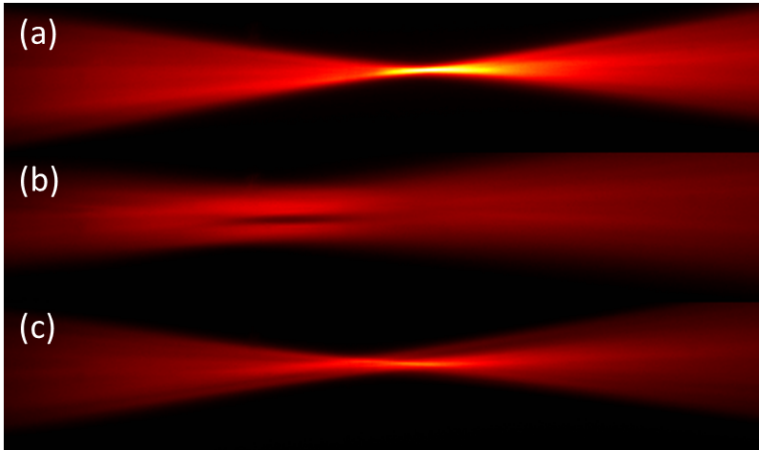


Figure 3.2: (a) Beam profile in fluorescent agarose without added aberration. (b) Beam profile with a low power cylinder placed off-axis in the pupil plane of the focusing objective. (c) The corrected beam profile using the wavefront sensor system.

epi-fluorescent light. The light incident to the microscope is reflected from a dichroic mirror (DCM) (MD498, Thorlabs, U.S.) such that the epi-fluorescent light from the sample can be collected via an optical relay (AC254-150-A-ML and AC254-100-A-ML, Thorlabs, U.S.) onto this wavefront sensor. A tunable iris (IR) (SM1D12D, Thorlabs, U.S.) for regulating the out-of-focus fluorescence is implemented in the image plane of the optical relay to help with the sensing procedure.

The feedforward calibration is practically done as follows. A reference sample is mounted on the setup, this must be uniformly fluorescent and have the same systematic aberrations as the regular samples. For this purpose, fluorescein in low density agarose (0.5%) is chosen and mounted in a square sided 1x1mm capillary tubes (Vitrotubes™ 1x1mm, VitroCom, U.S.). The laser beam is focused to a spot via the SLM into the fluorescent agarose and aligned with the centre of the FOV of the imaging camera.

This defines the reference position of the Shack-Hartmann spots and it is regarded as virtually aberration free. The wavefront sensor uses the brightest 350 sub-apertures and reconstructs the wavefront using 50 Zernike modes. The sensor geometry matrix G is calculated based on these reference positions and the Zernike phase constructor for the SLM Φ is constructed based on the device properties.

To this reference position a fixed and known amount of tip, tilt and defocus are applied to the SLM sequentially and the displacement of the spots on the Shack-Hartmann are recorded. The scaling parameter β between the applied Zernike coefficient for the SLM and the measured coefficient is recorded and stored in memory. The expression found in Eq.3.5 can now be applied to calculate the correction.

To test this calibration an amount of tip, tilt and defocus are applied to the SLM and the system is run in a closed-loop mode, for only these modes. The system is found to return to the reference position after a few iterations (depending on the size

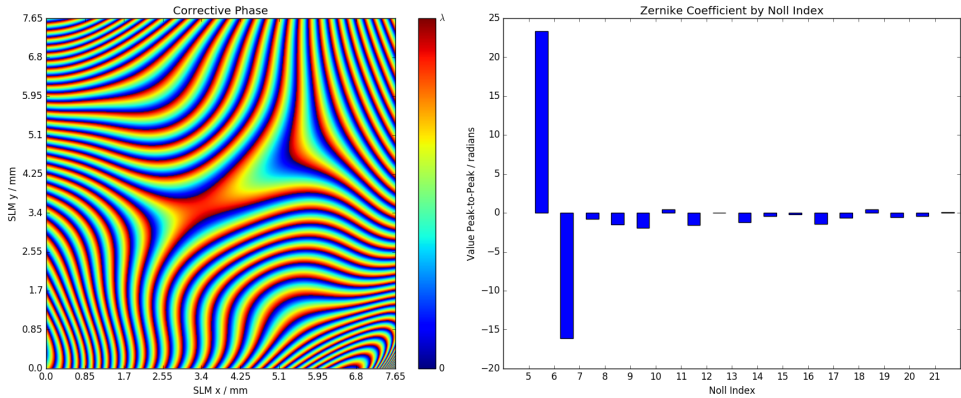


Figure 3.3: On the left the corrective phase based on the data from the wavefront sensor applied to the corrector when imaging a microbead through a *Tg(fli:GFP)* zebrafish embryo as seen in Fig. 3.6 is shown. The phase is wrapped in the range, 0 to 2π or 0 to λ , the wavelength of the light is shown. The right side shows the decomposition of this phase in the peak-to-peak Zernike coefficients in radians ordered by Noll index starting at index 5, astigmatism, below which is uncorrected by the system.

of the feedback parameter), therefore, the calibration is verified for these modes.

In order to test the calibration for higher order Zernike modes it is possible to place a low-power cylinder in the pupil plane of the focusing objective. By imaging the fluorescent agarose it is possible to test if the adaptive system is able to correct modes higher than tip, tilt and defocus. If this lens is placed tilted and off-axis it will introduce further low order Zernike modes above astigmatism. The results of this test, shown in Fig. 3.2, demonstrate the corrective ability of the feedforward system. The limitations of single step correction are also visible in this data. It shows that the system is unlikely to return to the diffraction-limit in a single step, however, significant improvement of the beam profile is observed.

The wavefront sensor is now calibrated for use with any sample. A further note is that when a sample is mounted in the microscope, it is necessary to disable the correction of the translational modes, as they effect the three-dimensional imaging process. In Fig. 3.3, a demonstration of the reconstruction of the wavefront for a sample is shown. The reconstructed wrapped phase is displayed next to the decomposition of modes from the wavefront sensor. The source here was a microbead after a *Tg(fli:GFP)* zebrafish embryo as described in the following section. The limiting factor in the speed of the correction is the exposure time of the camera for sufficient signal-to-noise ratio, typically of the order of a few hundred milliseconds.

3.4. Biological Imaging Results

To test the wavefront sensor technique on biological samples a number of fixed *Tg(fli:GFP)* zebrafish embryos three days post-fertilization (dpf) were imaged on the microscope. Three-dimensional stacks of $400 \times 400 \times 100\mu\text{m}$ were recorded by scan-

ning the sheet and the focus with the DM and the SLM respectively before and after adaptive correction. The specimens were sampled axially at the Nyquist sampling rate of the objective of $1\mu\text{m}$. The raw data was acquired in the xy -plane and later re-sliced for visualization as explained by Fig. 3.4.

It may be noted that the field-of-view of the detection microscope along the illumination path, x -axis, is much larger than the region over which the light-sheet is thinner than the detection objective depth-of-focus, in this case around $\approx 23\mu\text{m}$. Outside of this region the sectioning ability and the axial resolution are worse. The divergence of the beam can be seen in Fig. 3.2 as this is acquired over the same field-of-view.

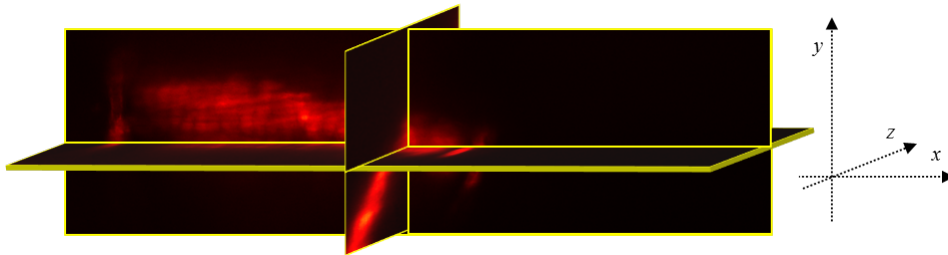


Figure 3.4: The axes definition and imaging form of the microscope. The raw images are acquired in the xy plane and then are re-sliced to form images in xz and yz planes, which can be used for axial comparison.

The z -stack without any correction was acquired using a Gaussian light-sheet. Afterwards, the cylindrical focus was turned off and the wavefront from the sample was measured in the epi-fluorescent signal. Using the ratio of feedback determined in the calibration the conjugate phase is applied to the SLM and a second dataset was acquired without tip, tilt and defocus mode correction. These datasets were re-sliced into xz -orientation and yz -orientation for axial comparison and maximum intensity projections of the central 512 planes are shown side by side in Fig. 3.5.

It is expected that if the aberrations in the light-sheet are reduced then the sheet thickness will decrease, therefore, an increase in the axial resolution should be observed. Furthermore, in a suitable regions of the samples, features that were not visible with the aberrated light-sheet should become visible with the corrected light-sheet.

For an example of the performance of the system, a section from the body region of one of the zebrafish has been included in Fig. 3.5. Looking at the projections found here, one sees agreement with these expectations. The spreading of the features along the axial z direction is smaller in the corrected beam, thus verifying that aberrations have been corrected by the system. It should be noted that this was done using only the central plane as the reference for the correction due to the need for a centrally aligned region of fluorescence for the wavefront sensing. This correction is likely to only be good for a limited range in three dimensions depending on the structure of the sample, however, it is found that the correction appears to have a positive effect throughout the z -range here of $100\mu\text{m}$ and in the visible y -range of around $200\mu\text{m}$. A sample with intensely varying refractive index would be expected to fare worse, nevertheless,

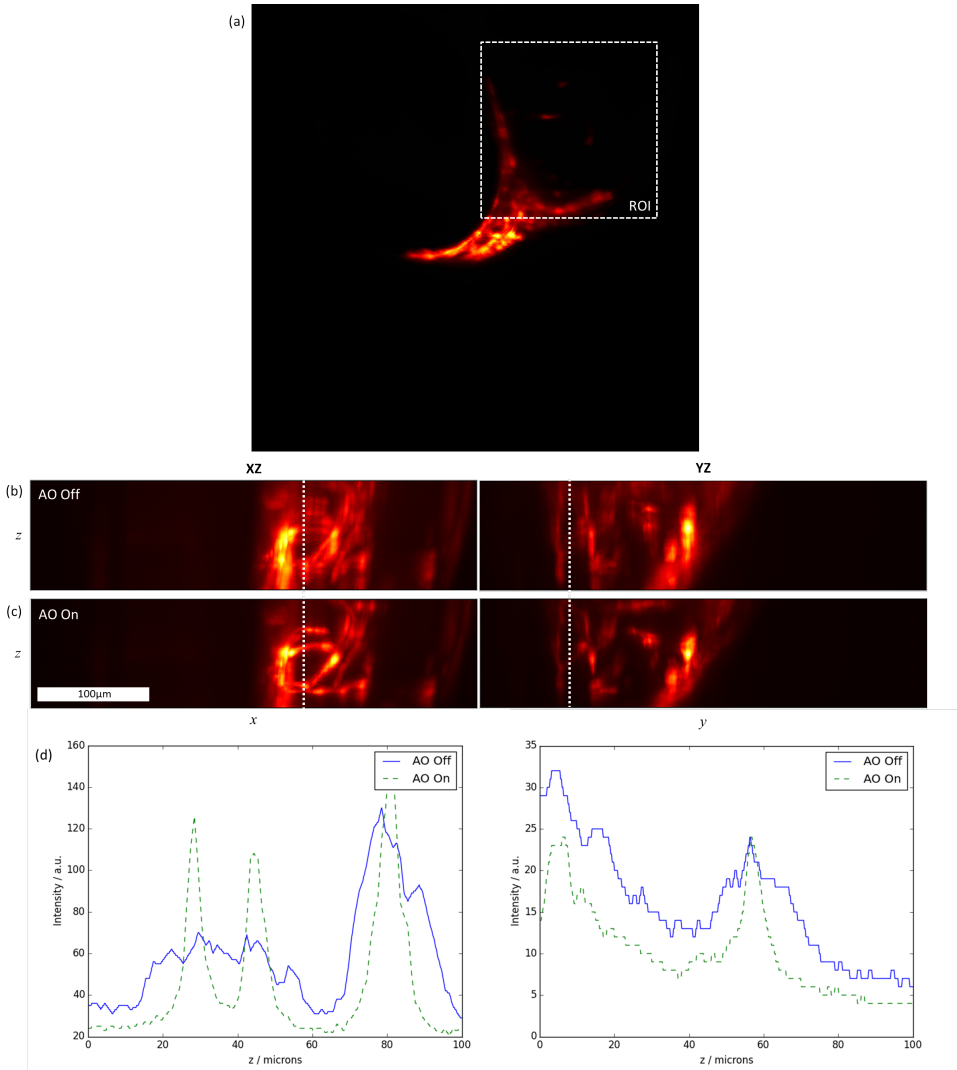


Figure 3.5: (a) A raw slice from the corrected dataset showing the region of interest (ROI.) (b) Maximum intensity projections through the ROI to give xz-images and yz-images from a 3 dpf *Tg(fli:GFP)* zebrafish larvae for a standard non-adaptive light-sheet. (c) The same ROI with adaptive correction. (d) The line profiles taken through these projections along the white lines shown in (b) and (c).

with an SLM conjugated to the system pupil only the isoplanatic aberrations from the centre of the FOV can be efficiently corrected.

Line profiles in the axial direction have been taken, denoted by the white lines in the images, and are displayed next to the corrected images. From these it can be clearly seen that the correction has increased the resolution and brought out features

not visible in the original images. The contrast between regions of no fluorescence and fluorescence are increase also, in keeping with the prediction of better optical sectioning.

In order to quantify the increase in resolution, a zebrafish was included in agarose containing fluorescent microbeads. A microbead is subsequently placed in the centre of the FOV after the light has passed through the zebrafish. In this way, the image of the microbead is affected by an aberration comparable to the one affected images of the biological sample. A three dimensional acquisition is done with and without correction and in Fig. 3.6 the results of this test show conclusively that the adaptive system improves the axial resolution of the system from an aberrated FWHM of $9.2 \pm 0.1 \mu\text{m}$ to a corrected $3.4 \pm 0.1 \mu\text{m}$.

Notice here that the quality of the image in the zebrafish is not as high as previously shown, as the system is sensing the light from the microbead placed behind it and correcting for that, however, there is still some improvement as the labelled vascular structure can be more clearly seen in this region of tail with the AO on.

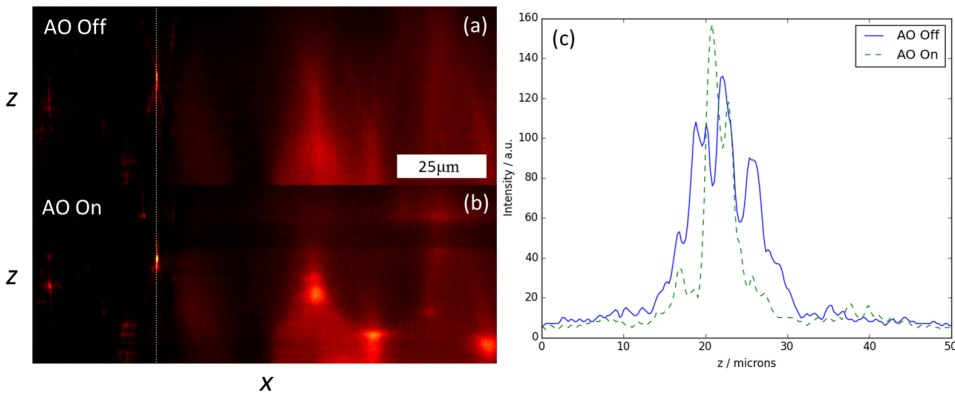


Figure 3.6: Imaging a microbead sample to demonstrate axial resolution improvement. (a) A xz -slice from a dataset where a microbead is used as the guide star after an aberrating sample. (b) The same field of view as in (a) with the adaptive correction system applied. (c) Line profile through the microbead to show the improvement made by the adaptive system. The light is incident from the right.

3.5. Discussion

By direct wavefront sensing on the epi-fluorescent light from a sample, the phase aberrations have been determined and corrected by using feedforward control. The benefits of the correction of phase aberrations as outlined in the introduction are many, and with the methodology presented it has been possible to implement them in the illumination arm of the light-sheet fluorescence microscope.

As a result of this feedforward control the images produced by the adaptive microscope are better than those produced by the same microscope without the adaptive control applied. The methodology lies in the same stream of adaptive optics control

that is also being implemented in astronomical telescopes [15] as an alternative to the more traditional feedback based systems. The use of the epi-fluorescent light appears to be the only available information source for the correction of the phase aberrations in the illumination arm of this type of microscope.

This chapter has focused on how to sense and correct these phase aberrations, but it should be noted that the methodology is also compatible and parallelizable with any modifications to the shape of the beam as demonstrated by multiple groups [9, 14, 16, 17], which if used together would potentially allow for an even greater increase in imaging quality.

The technique is not perfect and does have a drawback that is common to all wavefront sensor methods, it is expected to produce strongly anisoplanatic correction. The correction is calculated only for the centre of the field-of-view and then it is applied for imaging over an entire volume meaning that the quality of the correction should decrease with increasing displacement from this position. From our imaging experiments, however, it is found that the effect is not large enough to require continuous (and problematic) feedforward control to the SLM, despite imaging in a zebrafish that is optically inhomogeneous.

The wavefront sensor is a relatively simple addition to the adaptive LSFM system, being the replacement of the mirror with a dichroic mirror and a $4-f$ system to the sensor. If it is possible to build and implement in a light-sheet microscope, it would guarantee an improvement in image quality, signal-to-noise ratio and axial resolution. The use of a wavefront sensor means that the system is fast, robust and accurate as long as an area of fluorescence can be located in the centre of the field of view. As the fluorescent areas of the sample are generally of interest, it does not apply a particularly stringent constraint on the regions that can be imaged.

From an additional user perspective, the technique is fast and non-invasive, meaning it can work seamlessly in the background once the calibration is done, and as long as the system does not change the calibration will be valid over a long timespan. Moreover, it does not require the use of cleared or genetically engineered samples as the adaptive components work to overcome the optical inhomogeneities.

In summary and conclusion, this chapter has demonstrated that the aberrations present within a sample can be sensed and corrected in the illumination arm of a light-sheet fluorescence microscope, using a feedforward control methodology. As a result, the images from the microscope are improved compared with the non-adaptive case, this is due to a better axial resolution and beam quality produced by the correction of phase aberrations.

References

- [1] D. Wilding, P. Pozzi, O. Soloviev, G. Vdovin, and M. Verhaegen, *Adaptive illumination based on direct wavefront sensing in a light-sheet fluorescence microscope*, *Optics express* **24**, 24896 (2016).
- [2] A. Voie, D. Burns, and F. Spelman, *Orthogonal-plane fluorescence optical sec-*

- tioning: Three-dimensional imaging of macroscopic biological specimens*, Journal of microscopy **170**, 229 (1993).
- [3] J. Huisken, J. Swoger, F. Del Bene, J. Wittbrodt, and E. H. Stelzer, *Optical sectioning deep inside live embryos by selective plane illumination microscopy*, Science **305**, 1007 (2004).
- [4] C. Bourgenot, C. D. Saunter, J. M. Taylor, J. M. Girkin, and G. D. Love, *3d adaptive optics in a light sheet microscope*, Optics express **20**, 13252 (2012).
- [5] M. J. Booth, *Adaptive optical microscopy: the ongoing quest for a perfect image*, Light: Science & Applications **3**, e165 (2014).
- [6] B. C. Platt and R. Shack, *History and principles of shack-hartmann wavefront sensing*, Journal of Refractive Surgery **17**, S573 (2001).
- [7] H.-U. Dodt, U. Leischner, A. Schierloh, N. Jährling, C. P. Mauch, K. Deininger, J. M. Deussing, M. Eder, W. Zieglgänsberger, and K. Becker, *Ultramicroscopy: three-dimensional visualization of neuronal networks in the whole mouse brain*, Nature methods **4**, 331 (2007).
- [8] R. M. White, A. Sessa, C. Burke, T. Bowman, J. LeBlanc, C. Ceol, C. Bourque, M. Dovey, W. Goessling, C. E. Burns, and L. I. Zon, *Transparent adult zebrafish as a tool for in vivo transplantation analysis*, Cell stem cell **2**, 183 (2008).
- [9] F. O. Fahrbach, V. Gurchenkov, K. Alessandri, P. Nassoy, and A. Rohrbach, *Light-sheet microscopy in thick media using scanned bessel beams and two-photon fluorescence excitation*, Optics express **21**, 13824 (2013).
- [10] P. J. Verveer, J. Swoger, F. Pampaloni, K. Greger, M. Marcello, and E. H. Stelzer, *High-resolution three-dimensional imaging of large specimens with light sheet-based microscopy*, Nature methods **4**, 311 (2007).
- [11] M. J. Booth, *Adaptive optics in microscopy*, Philosophical Transactions of the Royal Society of London A: Mathematical, Physical and Engineering Sciences **365**, 2829 (2007).
- [12] M. Booth, *Wave front sensor-less adaptive optics: a model-based approach using sphere packings*, Optics Express **14**, 1339 (2006).
- [13] X. Tao, B. Fernandez, O. Azucena, M. Fu, D. Garcia, Y. Zuo, D. C. Chen, and J. Kubby, *Adaptive optics confocal microscopy using direct wavefront sensing*, Optics letters **36**, 1062 (2011).
- [14] D. Wilding, P. Pozzi, O. Soloviev, G. Vdovin, C. J. Sheppard, and M. Verhaegen, *Pupil filters for extending the field-of-view in light-sheet microscopy*, Optics letters **41**, 1205 (2016).

- [15] D. M. Wiberg, C. E. Max, and D. T. Gavel, *Geometric view of adaptive optics control*, *JOSA A* **22**, 870 (2005).
- [16] B.-C. Chen, W. R. Legant, K. Wang, L. Shao, D. E. Milkie, M. W. Davidson, C. Janetopoulos, X. S. Wu, J. A. Hammer, Z. Liu, B. P. English, Y. Mimori-Kiyosue, D. P. Romero, A. T. Ritter, J. Lippincott-Schwartz, L. Fritz-Laylin, R. D. Mullins, D. M. Mitchell, J. N. Bembenek, A.-C. Reymann, R. Böhme, S. W. Grill, J. T. Wang, G. Seydoux, U. S. Tulu, D. P. Kiehart, and E. Betzig, *Lattice light-sheet microscopy: Imaging molecules to embryos at high spatiotemporal resolution*, *Science* **346** (2014), 10.1126/science.1257998, <http://science.sciencemag.org/content/346/6208/1257998.full.pdf> .
- [17] T. Vettenburg, H. I. Dalgarno, J. Nytk, C. Coll-Lladó, D. E. Ferrier, T. Čížmár, F. J. Gunn-Moore, and K. Dholakia, *Light-sheet microscopy using an airy beam*, *Nature methods* **11**, 541 (2014).

4

Correcting the Image Part One

It is always darkest just before the Day dawneth.

Thomas Fuller

Chapter Abstract

A methodology for retrieving the unknown object distribution and point-spread functions (PSFs) from a set of images acquired in the presence of temporal phase aberrations is presented in this chapter. The method works by finding optimal complimentary linear filters for multi-frame deconvolution. The algorithm uses undemanding computational operations and few *a priori*, making it simple, fast and robust even at low signal-to-noise ratios. Results of numerical simulations and experimental tests are given as empirical proof, alongside comparisons with other algorithms found in the literature.

This chapter has been published in Optics Express *Blind multiframe deconvolution by tangential iterative projections*, Optics Express **25**, 24 (2017) [1].

4.1. Introduction

Scientific imaging systems used in real-world applications rarely produce images that are comparable with their theoretical optimum — the diffraction limit. The presence of media-induced aberrations, both in phase and amplitude, produces a quantitative reduction in the amount of information that is recorded by the system. Incoherent imaging may, however, be considered as a convolution between two functions and if the blurring kernel, or point-spread function, can be obtained it is theoretically possible to extract the object distribution from the recorded image data. The problem is not instantly tractable, as this deconvolution, is a classic ill-posed inverse problem. If nothing is known *a priori* about the two functions, it implies that for any recorded image there are infinite possible combinations of object and point-spread function.

To begin the story of how these inverse problem may be solved, one must go back several decades to the pioneering work of Gerchberg and Saxton [2]. They made great practical progress in solving these inverse problems with the application of an alternating projection (AP) framework. Later the work of Fienup [3] refined these initial discoveries and was significant in finding practical and robust solutions to the phase retrieval problem along with a more thorough mathematical foundation for the operation of AP algorithms.

Gonsalves [4] worked on a related problem, known as phase diversity, approaching it with a similar alternating framework. In phase diversity, one adds a known phase aberration to the optical system and subsequently solves an optimisation problem in order to identify any other unknown aberration. The work of Paxman et al. [5] shows the move towards a more explicit optimisation framework, where a metric is explicitly evaluated and used to inform steps towards a solution. A method for the identification of both the object and the unknown phase was presented and marks the branching of methodology for solving inverse problems: implicit optimisation schemes such as AP and those explicitly evaluating an optimisation metric.

Whilst adding known phases to an optical system is possible, it is indeed, not very practical in many cases. To resolve this problem the notion of an iterative *blind* deconvolution was presented by Ayers and Dainty [6]. Again, in this work they returned to the AP framework and allowed a way to identify the object and the point-spread function by the application of *a priori* constraints on the object and point-spread function.

Aberrations cause certain spatial frequencies in the object not to be transmitted to the imaging sensor meaning that a complete reconstruction of the object from a single aberrated observation is impossible. The way to solve this problem is by the acquisition of multiple frames with different aberrations. If there is sufficient diversity, i.e. all frequencies have been transmitted in the sequence, these images can be used to recover a better estimate of the object than could be possible with a single image by using a blind multi-frame deconvolution algorithm.

Blind multi-frame deconvolution (BMFD) was first truly demonstrated in a practical setting by Schulz [7] and later by Yaroslavsky et al. [8]. Since this point in time, the number of publications about types and variations of blind multi-frame algorithms

have multiplied beyond the scope that may all be summarised here [9–12]. They have become merely a subset of a host of general deconvolution methods that can be broadly subdivided into two main groups: linear and non-linear methods. The linear methods, e.g. Wiener-like filters [13], are fast and robust, but cannot restore information lost during image registration and have propensity to produce non-physical solutions (e.g. negative object intensity). Non-linear methods [14], on the other hand, use the constraints imposed by the physical conditions and are generally less robust and slower to implement.

Another current method for blind multi-frame deconvolution is Maximum Likelihood Estimation (MLE) [15, 16], which uses a Bayesian framework to find the most likely object (and PSFs) satisfying all of the *a priori* information. Multi-frame may also be referred to as multichannel deconvolution [17] and is functionally equivalent. Most of these algorithms may be reduced to the alternating minimisation (AM) class of methods or otherwise Iterative Shrinkage [14, 18]. AM methods subdivide the problem into several individual parts (usually two) and proceed by iteratively updating each of the parts assuming the other parts to be fixed and given by the previous iteration step, they have been well studied as a methodology for solving such inverse problems [19, 20].

The drawback with most inverse methods, for blind deconvolution specifically, is their reliance on *a priori* information to work successfully. Or to be more specific, tunable *a priori* information. It is not possible to assume that all the necessary information is known to the investigator. The second problem, and perhaps the more significant problem, is that these techniques do not work reliably on data at low signal-to-noise ratios without significant investment of time to tune and denoise the data.

In this chapter, the tangential iterative projections (TIP) algorithm is presented as an approach to the aforementioned problems, and as a widely applicable algorithm that may be employed in imaging scenarios where temporal variation of the phase aberration is present. It is shown that it is possible with minimal *a priori* information, only the support size for the point-spread function and its real non-negativity, that blind multi-frame deconvolution can be performed robustly at low signal-to-noise ratios. To verify the claims, thorough qualitative and quantitative tests are performed on numerically simulated images and those acquired with a telescope.

The outline of this chapter is as follows: firstly, the formalisation of blind multi-frame (or multi-channel) deconvolution shall be given; secondly, an outline of the framework of the TIP algorithm will be explained integrated with a look at the implementation of the algorithm; then the experimental results followed by a discussion and the conclusions of the chapter.

4.2. Blind multi-frame (or multi-channel) deconvolution

One has an incoherent imaging system through which it is possible to acquire a set of N two-dimensional images $\{i_n\}$, $n \in \mathbb{N}$ and $1 \leq n \leq N$, of an unknown and constant source object o with changing isoplanatic aberrations, giving rise to different point-spread functions (PSFs) $\{h_n\}$ for each of these recorded images $\{i_n\}$ with an additive

noise component w_n . These images are sampled on a discrete evenly spaced grid with $M \times M$ pixels.

In this *blind* case, it is assumed that one neither knows the object nor the PSFs, and both these variables must be jointly estimated. The mathematical model for the n^{th} image formation is:

$$\begin{aligned} i_n &= o * h_n + w_n, \\ i_n, o, h_n &\in \mathbb{R}_+^{M \times M}, \end{aligned} \quad (4.1)$$

where $*$ is the convolution operation and $\mathbb{R}_+^{M \times M}$ defines that all the images, the object and the point-spread functions are all discrete real non-negative ($M \times M$)-dimensional matrices. It is assumed that within an optimisation framework, there exists a set of $\{\hat{h}_n\}$ and \hat{o} that may be used to accurately approximate the $\{i_n\}$ in the least-squares sense:

$$\begin{aligned} \{\hat{h}_n, \hat{o}\} &= \arg \min_{h_n, o} \sum_{n=1}^N \|i_n - o * h_n\|^2, \\ \text{s.t. } o, h_n &\in \mathbb{R}_+^{M \times M}, \end{aligned} \quad (4.2)$$

where $\|\cdot\|$ denotes L_2 norm. This form of the cost function ensures fidelity to the original image data, but does not provide any constraints to what the PSFs or the object should be, and it has seemingly trivial solutions, such as:

$$\begin{aligned} \hat{h}_n &= i_n, \\ \hat{o} &= \delta^{M \times M}, \\ i_n &= i_n * \delta^{M \times M}, \end{aligned} \quad (4.3)$$

where $\delta^{M \times M}$ is the Delta function on $\mathbb{R}_+^{M \times M}$. In order to obtain a solution that is closer to the real values of $\{h_n\}$ and o additional terms, corresponding to the solution smoothness, reality, or regularisation, may be added to the cost function, or otherwise achieved by imposing constraints on the solutions instead. A discussion of which, will be returned to later.

By exploiting the properties of the Fourier transform, the relationship between the recorded spectral images $I_n = \mathcal{F}(i_n)$, the optical transfer functions (OTFs) $H_n = \mathcal{F}(h_n)$, and the object spectrum $O = \mathcal{F}(o)$ is given by:

$$I_n(\vec{v}_m) = H_n(\vec{v}_m) \cdot O(\vec{v}_m) + W_n(\vec{v}_m), \quad (4.4)$$

where \vec{v}_m , $m = 1, \dots, M^2$ are the spectral sampling points and \cdot represents element-wise multiplication. Here it is assumed that there is the presence of W_n , which corresponds to the unknown noise spectrum. With this notation, (4.2) can be represented as:

$$\begin{aligned} \{\hat{H}_n, \hat{O}\} &= \arg \min_{H_n, O} \sum_{m=1}^{M^2} \sum_{n=1}^N |I_n(\vec{v}_m) - O(\vec{v}_m) \cdot H_n(\vec{v}_m)|^2, \\ \text{s.t. } O, H_n &\in \{\mathcal{F}(f) \text{ with } f \in \mathbb{R}_+^{M \times M}\}. \end{aligned} \quad (4.5)$$

The problem of (4.5) is a constrained bilinear problem, with an objective function that is linear in each of the two variables O and H_n if the other is fixed, and can be solved by alternating minimisation fixing one variable sequentially [21]. From here the m index will be omitted for notational clarity.

For a set of known OTFs $\{H_n\}$ the solution to (4.5) is given by the linear multi-frame deconvolution filter [8]:

$$\hat{O} = \frac{\sum_{n=1}^N (H_n)^* I_n}{\sum_{n=1}^N |H_n|^2}. \quad (4.6)$$

This object estimation may be seen as a Wiener filter with a infinite signal-to-noise ratio (SNR), whose general form for known PSFs is expressed as:

$$\hat{O} = \frac{\sum_{n=1}^N (H_n)^* I_n}{\sum_{n=1}^N |H_n|^2 + \frac{1}{\text{SNR}}}. \quad (4.7)$$

As shown in Jansson et al. [14] and elsewhere, that even for the case of one image ($N = 1$), and a known PSF h , unconstrained linear deconvolution results in noise amplification and loss of information in points where H is close to zero and can be addressed by imposing a non-negativity constraint on the object (and/or the PSF), which plays an important role in establishing convergence to a solution. With this in mind, the problem stated in (4.5) can be augmented by applying any other *a priori* knowledge in terms of the feasible sets of objects and PSFs \mathcal{O} and \mathcal{H} respectively, and the optimisation problem becomes:

$$\begin{aligned} \{\hat{H}_n, \hat{O}\} &= \arg \min_{H_n, O} \sum_{n=1}^N \|I_n - O \cdot H_n\|^2, \\ \text{s.t. } O &\in \mathcal{O}, \\ H_n &\in \mathcal{H}. \end{aligned} \quad (4.8)$$

For completeness, following one major family of solutions to the BMFD problem; this problem of jointly estimating the object and the PSFs belonging to sets \mathcal{O} and \mathcal{H} has been alternatively formulated as a regularised least-squares cost function [17, 18]:

$$\{\hat{H}_n, \hat{O}\} = \arg \min_{H_n, O} \sum_{n=1}^N \|I_n - O \cdot H_n\|^2 + \lambda_o Q(O) + \lambda_h R(\{H_n\}). \quad (4.9)$$

Here the terms $Q(O)$ and $R(\{H_n\})$ are regularisation terms on respectively the object and the PSFs. Many different variations have been proposed in the last few decades, for the interested, the book [18] has an overview and (convergence) analysis of some numerical solutions to this problem based on alternating minimisation (AM). The convergence analysis in [18] is based on the following paper [22]. In Chan and Wong [22], the use is made of quadratic smoothness regularisers for both the image and PSFs. This type of regularisation tend to favour very smooth solutions [18] (as will be seen later). In order to avoid such smoothing the total variation (TV) for both the object and the PSFs has been elsewhere proposed as alternative regularisation (metrics) [18].

4.3. TIP algorithm

The problem stated by (4.8) is a non-convex optimisation problem, leading to non-unique solutions and multiple local minima [22]. The TIP algorithm does not attempt to minimise this metric. The approach of the TIP algorithm is to modify the problem of (4.8) in such a way that it would be possible to get a close enough estimate of the object using as little *a priori* information and with as simple operations as possible.

Following this train of thought, TIP keeps using the linear deconvolution estimate for the object (4.6) at every iteration step. By analysing the denominator of the formula, one can note that, unlike the case of single-image deconvolution, the noise amplification issue will be less prominent if the OTFs $\{\hat{H}_n\}$ do not have common zeros. Please note here, that noise still will be amplified at high frequencies, where the OTFs are small because of the diffraction effect; this issue will be addressed by apodisation as explained in the Discussion. Where there are no common zeros, however, a close enough estimate of the object will be given by a simple and fast operation of linear deconvolution provided the OTFs estimates are close enough to their true values.

To formalise, the k -th estimate for the object spectrum $\hat{O}^{(k)}$ is obtained as projection on the feasible set of the result of the linear deconvolution filter:

$$\hat{O}^{(k)} = \mathcal{P}_{\mathcal{O}} \arg \min_{O \in \mathbb{C}^{M \times M}} \sum_{n=1}^N \|I_n - O \hat{H}_n^{(k-1)}\|^2. \quad (4.10)$$

To update the estimates of OTFs $\{\hat{H}_n\}$, a natural approach would be to use the same (4.8), now for a fixed object spectrum estimate \hat{O} , which is equivalent to finding a projection of point (I_1, \dots, I_n) on a convex set $\hat{O}\mathcal{H}$ (that is a non-uniformly scaled copy of \mathcal{H}). Despite its convexity, this problem is difficult to solve as one needs to update the projection operators at every iteration step, which is contradictory to the desire for simplicity. Instead of this, TIP uses again the linear deconvolution filter I_n/\hat{O} with a subsequent projection onto feasibility set \mathcal{H} , which remains constant at every iteration step. To formalise:

$$\hat{H}_n^{(k)} = \mathcal{P}_{\mathcal{H}} \frac{I_n}{\hat{O}^{(k)}}, \quad n = 1, \dots, N. \quad (4.11)$$

At first glance, it is not clear whether this formula is relevant to the initial problem. It will now be illustrated in a non-rigorous manner that it makes good sense for some types of constraints. Firstly, one notes that in case of non-negative objects and PSFs, the L_1 norm of the convolution operation is equal to the product of the norms of its terms, that is:

$$\|o * h_n\|_1 = \|o\|_1 \cdot \|h_n\|_1. \quad (4.12)$$

Here one can assume all the norms have unit value by adding the corresponding constraint to the definitions of \mathcal{O} and \mathcal{H} , and including a re-normalisation step in each iteration of the algorithm.

Secondly, if one restricts \mathcal{H} to being the case of the limited support constraint $\mathcal{H} = \{h|h(x) = 0, x \notin \mathbb{X}\}$ for some set \mathbb{X} , one can represent any discrete PSF h as

the sum of two non-negative components, which shall be denoted as the tangential and normal components h_{\parallel} and h_{\perp} , the former made with pixels from \mathbb{X} , and the later by the rest of the pixels:

$$h = h_{\parallel} + h_{\perp}, \quad h(x)_{\parallel} = 0, \text{ if } x \notin \mathbb{X}, \quad h(x)_{\perp} = 0, \text{ if } x \in \mathbb{X}. \quad (4.13)$$

Non-negativity implies that $\|h\|_1 = \|h_{\parallel}\|_1 + \|h_{\perp}\|_1$ and thus for a noiseless images one yields from (4.12) and (4.13):

$$\|i\|_1 = \|o * h\|_1 = \|o\|_1 \|h_{\parallel}\|_1 + \|o\|_1 \|h_{\perp}\|_1. \quad (4.14)$$

If as an *a priori* one takes that (the most part of) the PSF is expected to be confined by the region \mathbb{X} , the last summand in (4.14) can be considered as fitting error and should be minimised. This is equivalent to maximising the tangential part of PSF. It may be then seen that the tangential part of the PSF is given by projecting the result of the linear deconvolution on \mathcal{H} :

$$h_{\parallel} = \mathcal{P}_{\mathcal{H}} \mathcal{F}^{-1} \frac{l}{O}, \quad (4.15)$$

and from this one gets the motivation for the use of (4.11). In presence of noise any tangential component of the noise deconvolved with the object is indiscernible from the possible PSF and will add up to the estimation:

$$i/o = h + w/o = (h_{\parallel} + (w/o)_{\parallel}) + (h_{\perp} + (w/o)_{\perp}), \quad (4.16)$$

where notation has been misused to denote as a/b result of linear deconvolution of a with b . This might result to the convergence of the algorithm to a wrong solution, which nevertheless will satisfy the imposed constraints.

By this novel alternating minimisation of the TIP algorithm, one ensures that when the image data is linearly deconvolved by the estimated OTFs $\{\hat{H}_n\}$ the object spectrum \hat{O} is closest to its feasible set. The object spectrum and the OTFs have a *mutual fidelity* with regards to the other. Whereas, to the author's knowledge the majority of blind multi-frame deconvolution methods focus on maximising the fidelity of $H_n \cdot O$ to the image data l_n within a regularisation framework to minimise the contribution of W_n vis-à-vis (4.9).

Figure 4.1 is a flow chart of the algorithm. In it the process of the TIP algorithm is given by 4 operators $\mathcal{P}_1 \dots \mathcal{P}_4$. The details of these operators are given in Table 4.1 and \mathbb{X} continues to define the finite support of the PSFs here, which may be a circle or a square of a tunable size. The algorithm starts with step \mathcal{P}_1 and uses δ -functions as the initial set of unknown PSFs $\{\hat{H}_n^{(0)}\}$, corresponding to minimal *a priori* knowledge about the PSFs.

4.4. Experiments

In this section, a set of experimental tests will be run to demonstrate the properties of the TIP algorithm. Firstly, the deconvolution results from the TIP algorithm will be

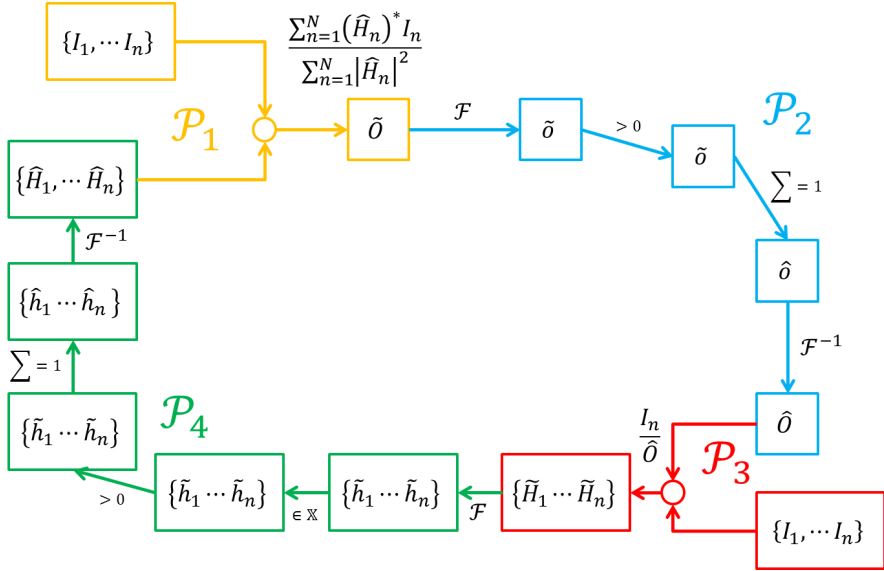


Figure 4.1: An algorithm flowchart showing the steps of TIP. The different projection steps are shown in different colours and the explicit operations are given by the lines between the boxes that contain the data. \mathcal{P}_1 is multi-frame linear deconvolution, \mathcal{P}_2 is the projection to the feasible set \mathcal{O} , \mathcal{P}_3 is linear deconvolution for every frame, and \mathcal{P}_4 is the projection to the feasible set \mathcal{H} . The details are shown in Table 4.1.

Table 4.1: Steps of the TIP algorithm with their descriptions

Step/Projection	Process	Description
Step 1 — \mathcal{P}_1	$\tilde{O} = \frac{\sum_{n=1}^N (\hat{H}_n)^* I_n}{\sum_{n=1}^N \hat{H}_n ^2}$	Multi-frame linear deconvolution
Step 2 — \mathcal{P}_2	$\tilde{o} = \mathcal{F}\{\tilde{O}\}$ $\tilde{o} = 0$ if $\tilde{o} < 0$ $\sum \tilde{o} = 1$ $\hat{O} = \mathcal{F}^{-1}\{\tilde{o}\}$	Fourier Transform Non-negativity Threshold Normalisation Inverse Fourier Transform
Step 3 — \mathcal{P}_3	$\tilde{H}_n = \frac{I_n}{\hat{O}}$	Single-frame linear deconvolution
Step 4 — \mathcal{P}_4	$\hat{h}_n = \mathcal{F}\{\tilde{H}_n\}$ $\hat{h}_n(\mathbf{x}) = 0$ if $\mathbf{x} \notin \mathbb{X}$ $\hat{h}_n = 0$ if $\hat{h}_n < 0$ $\sum \hat{h}_n = 1$ $\hat{H}_n = \mathcal{F}^{-1}\{\hat{h}_n\}$	Fourier Transform Finite Support Constraint Non-negativity Threshold Normalisation Inverse Fourier Transform

presented to give an overview of its general performance and behaviour. Secondly, it will be compared with other blind multi-frame deconvolution algorithms and they shall be analysed in terms of their noise robustness and performance on experimental data.

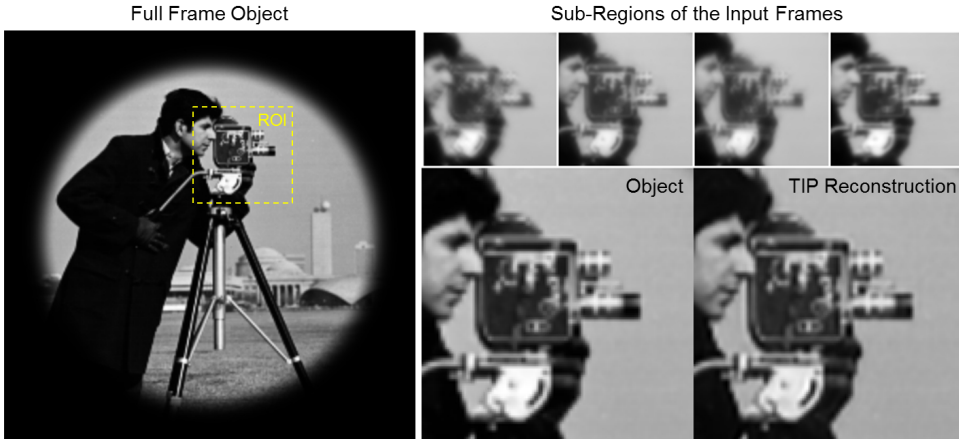


Figure 4.2: On the left, the full frame object is shown, the algorithm processes the image in this size. For clarity, a smaller region-of-interest (ROI) is reproduced on the right. This example shows the reconstruction of the TIP algorithm is very close to the object for this data set and provides an improvement over the input data. The PSFs for this dataset are shown in Fig. 4.3.

4.4.1. Object and PSF reconstruction

The test image of the cameraman is chosen for use as it gives a grayscale image with some features that are quickly lost in the presence of aberrations. This image is shown in Fig. 4.2, (512x512px, 16-bit) and is aberrated using randomly generated PSFs, based on 20 Zernike modes, to give 4 images created by multiplication of the object spectra with the OTFs. A point to note here is that the diffraction-limited image of the scene is lower resolution than the object in Fig. 4.2 due to the size of PSF, therefore, it should be not expected that the algorithm reproduces the object to the same resolution due to the band limitation. (In these images the loss is imperceptible.)

The result shown in Fig. 4.2 demonstrates that the TIP algorithm is able to correctly reconstruct the object o from this input data, furthermore, in Fig. 4.3 the reconstructions of the PSFs $\{\hat{h}_n\}$ show high fidelity to those used to generate the input images. The identification of the PSFs is not pixel perfect, however, it is good enough to produce a qualitatively good reconstruction of the object via the least-squares deconvolution ((4.6)). If one closely observes the edges in the object reconstruction, it is possible to see the effect of the errors in the PSF in the form of a halo.

4.4.2. Image types

The TIP result is better than any of the original observations and one is not introducing any amplification of unwanted noise — the nemesis of linear deconvolution procedures. To demonstrate this not a fluke of this single image, the same generation process with new PSFs is used for different objects, and the results are shown in Fig. 4.4. Figure 4.4 shows that the algorithm works on the following images: a cell from fluorescence microscopy (bright features on a dark field); a photograph of a tulip (dark features

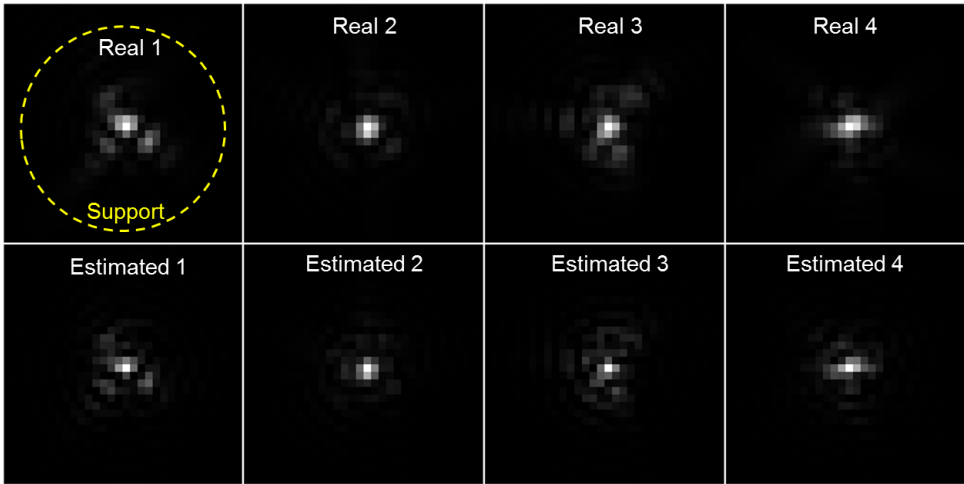


Figure 4.3: Comparison between the real PSFs, top row, used to generate the images seen in Fig. 4.2 and those retrieved by the TIP algorithm, bottom row. The size of the support is shown on the image, a circle with radius 11px.

on a light field); and also the 1951 USAF test chart (binary). It can be concluded from this that the TIP algorithm is no better suited one particular type of image than another, making use of *minimal a priori* information about the system, the algorithm is widely applicable; however, it better suited to extended sources than point-source images

4.4.3. Empirical convergence

In this chapter, the TIP algorithm has not been proven mathematically to converge. This is still a matter of ongoing research for the authors. What can be shown empirically, however, is that the algorithm does converge. To demonstrate this, 100 of trial datasets of 16 images are generated with different aberrations and no additive noise. These are processed using the TIP algorithm and the *peak signal-to-noise ratio* is recorded, and here it is defined in dB for images normalised in the range $[0, 1]$ for iteration k as being:

$$\text{PSNR}^k = -10 \log_{10} (\|o - \hat{o}\|_2^2 / M^2), \quad (4.17)$$

where \hat{o} follows the previous notation of being the estimated object. This is essentially, the difference between the estimated object and the real object, the higher the number the closer the result is to the correct solution.

A plot of these 100 datasets is shown in Fig. 4.5. Here all of the trialled datasets are shown to converge rapidly to a solution, this validates the claim that 10 iterations is enough to produce the solution, since the difference in 10 or 1000 iterations is minimal in linear space. What cannot be claimed, however, is that the algorithm always converges to the *correct* solution — even if for the *a priori* it is the *optimal* solution.

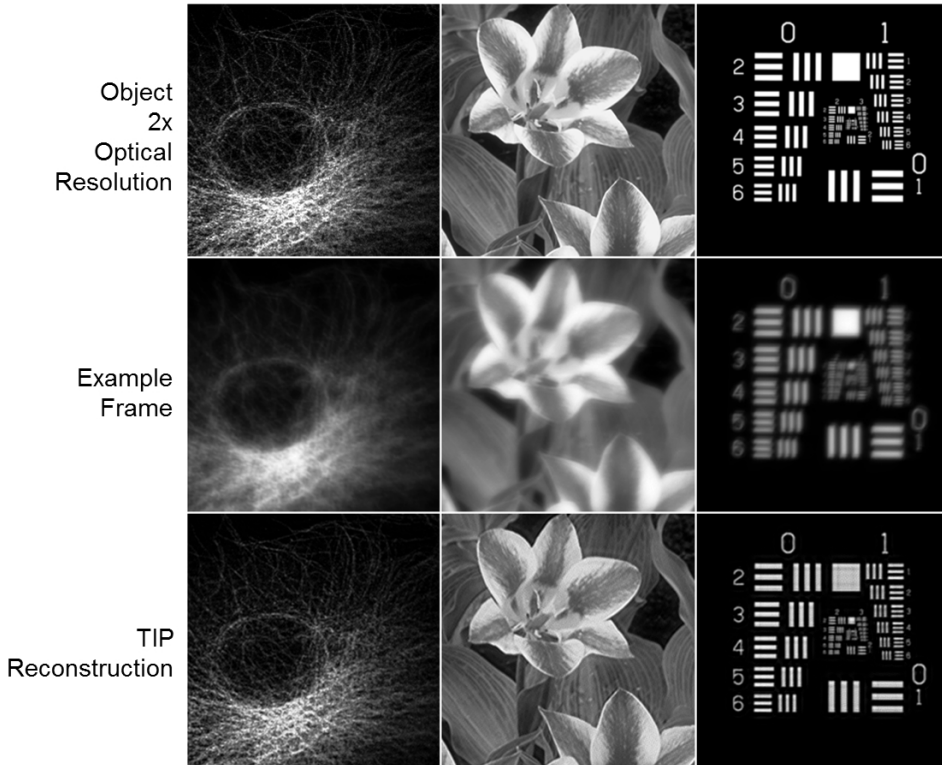


Figure 4.4: Comparison between the object (top), an acquired frame (middle), and the TIP reconstructions (bottom) for different image types.

The reason for this is simple, it is an inverse problem in a highly multidimensional space, which may have non-unique solution or have trivial solutions. The goal of the constraints used is to reduce which of these solutions the algorithm is able to converge to. Once again, empirically one observes that if the *a priori* constraints are suitable, the TIP algorithm produces a good deconvolution result — how this can be asserted is tackled in the following section.

4.4.4. Algorithm comparisons

In this sub-section, the performance of the TIP algorithm will be compared with existing methods found in the literature. Comparisons have been made here with: the algorithm described by Pakhomov and Losin [23], referred to as PL, an alternating projection algorithm; a regularisation-based approach from Sroubek and Milanfar [17], written as MCD; and a Bayesian algorithm found in Katkovnik et al. [16], written as MLE.

Fair comparison with the work of others, especially in image processing algorithms is a difficult or even impossible task. As has been previously stated, many algorithms require or can accept extra *a priori* information. By tuning these hyper-parameters, the results of the same algorithm can vary hugely in their performance on the same

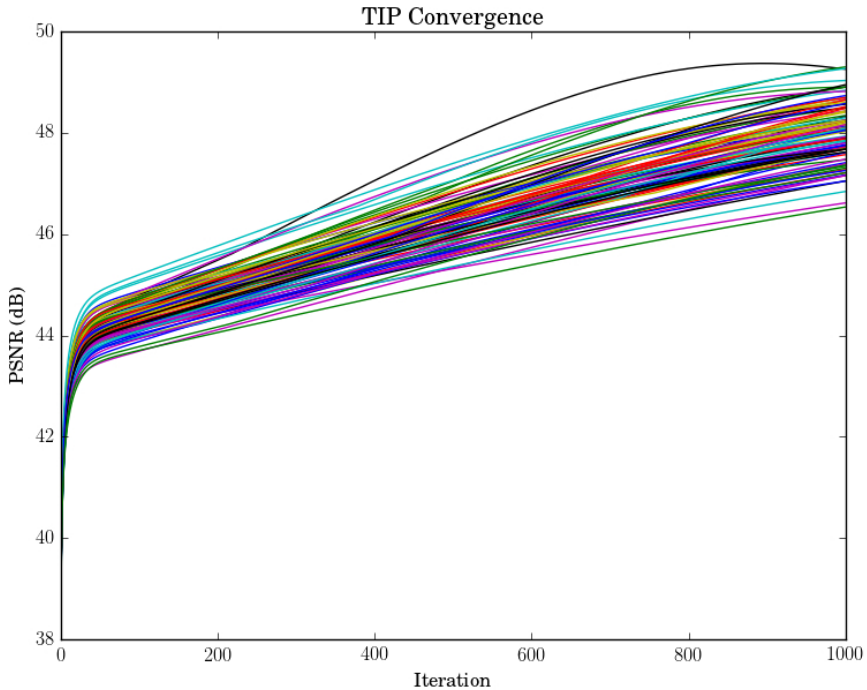


Figure 4.5: Demonstration of the convergence of the TIP algorithm by comparison of the PSNR of the estimated object at each iteration step. The algorithm shows empirical convergence in the majority of cases. Occasionally, the algorithm switches to another behaviour c.f. the top black line, the cause for this numerical instability is still unknown.

datasets. For these reasons, to make these comparisons as fair and scientific as possible, only algorithms that had an implementation available not written by the authors have been used. The exception here is the Pakhomov and Losin algorithm, an extension of which was used in the author's previous work [24, 25].

Care has been taken in this process to ensure the algorithms compared with performed as well as possible on the datasets used, by tuning of their hyper-parameters to the best of the author's knowledge and ability. The goal of these comparisons has been to show that with the same minimal *a priori* information for all the algorithms, i.e. the support size of the PSF, TIP performs better. This does not imply that the others are not excellent deconvolution algorithms or better than TIP under other conditions or extra *a priori*. Please note that some algorithms such as MLE have built in *a priori*, which makes the comparison even more difficult.

Solution quality

Returning to the image of the cameraman as an object, 16 images are generated with the additive Gaussian noise at one fourth $2^{14}/2^{16}$ of the signal level along with Poisson noise. To quantify the quality of the incident images with the aberrations a *blurred*

Table 4.2: Comparison between the PSNR for the images shown in Fig. 4.6. *BSNR is shown for the image.

Algorithm	Image*	PL	MLE	MCD	TIP
PSNR (dB)	0.23	12.7	10.7	12.1	24.8

signal-to-noise ratio (BSNR) can be defined as:

$$\text{BSNR} = 10 \log_{10} \left(\frac{\sum (S - \mu(S))^2}{\sum (W - \mu(W))^2} \right), \quad (4.18)$$

where S and W refer to the signal and the noise respectively, units of BSNR are decibels (dB). μ is the mean. This information is not accessible for the output images and therefore, to analyse these results quantitatively, one can compare the output PSNR. As further preparation, the images are apodized to remove the bright edges and the images are given to the four algorithms with no additional processing. The results of these deconvolutions for a sub-region are shown in Fig. 4.6.

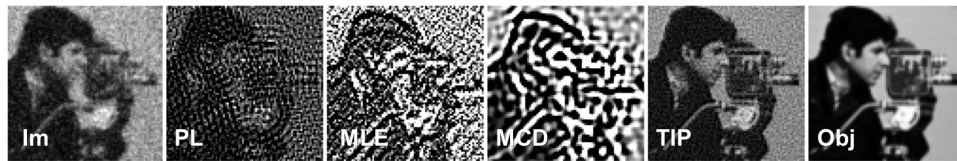


Figure 4.6: Comparison between the object reconstructions for different algorithms with the same *a priori* information. The sub-region of the first input image is shown on the left-hand side and the object on the right-hand side.

In these reconstructions one does not achieve the same result with each of the algorithms. The difference between these reconstructions lies in the algorithms' ability to be robust to the noise present in the images. In this example, the noise contributions have been added to a level to ensure that the other algorithms struggle and fail to correctly reconstruct the object. In this way, the superiority of the TIP algorithm for this task is hopefully demonstrated. It can be asserted without much argument that the TIP algorithm here produces the qualitatively and quantitatively better image, in a visual and in a PSNR sense respectively, see Table 4.2. The MLE and MCD solutions are corrupted by noise that destroys its dynamic range and the PL algorithm has strong sinusoidal components that result in interference-like effects in its reconstruction. The TIP reconstruction on the other hand contains a smoothness and fidelity to the object that is not seen in the other algorithms.

Effect of additive noise

Whilst in the previous section it was demonstrated on one dataset that the TIP algorithm performed better with regard to noise, it is necessary to engage with this point further.

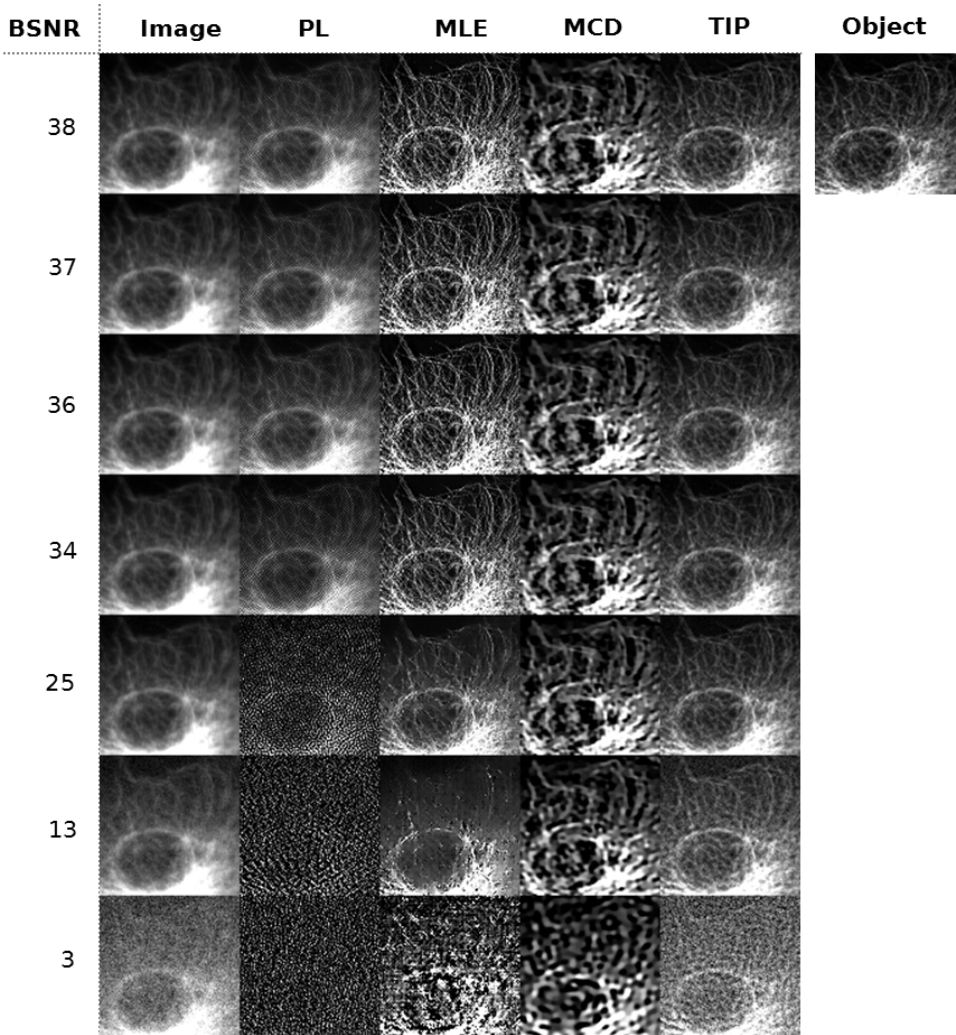


Figure 4.7: Comparison of algorithm performance vs. increasing noise level for four input frames with the same *a priori* information. The first column is the first image from the set i_1 . The second column is PL, the third MLE, fourth MCD, and the final column in the TIP algorithm. The object is shown in the top right hand corner.

A similar plot for the convergence have been made in the presence of noise showing similar behaviour and have been omitted for sake of brevity.

The other algorithms tested are very good blind multi-frame deconvolution algorithms, to show this one shall now compare over a range of BSNR values to show the point at which TIP becomes the better option. In each case, the *a priori* PSF support size is given as the same.

A set of simulated fluorescence microscopy images are used for this purpose, four

images with different aberrations. These are generated in the same manner as previously but are modified by changing the signal-to-noise ratio. Each of the aberrated images are generated so that the signal fills a full 16-bit range. To this a Poisson noise is added and then Gaussian noise is added with a standard deviation of increasing bit levels, i.e. $\sigma = 2^b$ where $b = 0, 1 \dots 15$. The result is then renormalised to use the full 16-bit range again, such that signal information is lost by casting to the nearest integer value. Explicitly, this is given by:

$$i_n = (2^{16} - 1) \frac{h_n * o}{\sum h_n * o} + \text{randp}(\lambda = (2^{16} - 1) * \frac{h_n * o}{\sum h_n * o}) + \text{randn}(\mu = 0, \sigma = 2^b),$$

$$i_n = (2^{16} - 1) \frac{i_n}{\sum i_n}. \quad (4.19)$$

As a result of this process a set of images was produced that have decreasing signal-to-noise ratio in such a way that the signal is encoded in a decreasing number of bits, i.e. 2^{16-b} . Thus essentially for the last set, the signal has a binary encoding, these values may also be converted easily into BSNR values.

The algorithms are run on these sets of four images for the different noise levels and the data is shown in Fig. 4.7. Here the first column shows the converted BSNR value for the bit encoding. The second corresponds to the first image in the series, the third to PL, the fourth to MLE, fifth MCD and the last to TIP. The even values of $b = 0, 2, \dots, 12$ have been represented here, discarding $b = 14$, in order to reduce the space, but what is displayed is sufficient to see the trends and performance of the algorithms. In the top right corner the object is shown for comparison with the solutions.

As with the previous section, one observes that the TIP algorithm is the most robust to the noise conditions and consistently produces the best reconstruction under all noise conditions when compared with the other algorithms. Even at the high signal-to-noise ratios the other algorithms fail to reproduce the object as seen in the figure; even though MLE that produces a sharp image, it does not accord as accurately as TIP with the object used to generate the images.

Telescope tests

Up to this point, the TIP algorithm has been shown to work on different simulated images under different noise conditions. As the final verification of the TIP methodology, one compares the performance of the algorithm with the other algorithms on experimental data from an amateur telescope (20cm diameter). These images are different from the model assumed in (4.1) as mostly in astronomical observation the aberration is not isoplanatic.

The object being observed is Jupiter and its moons through the turbulent atmosphere. The dataset comprises of 20 images acquired in a timelapse resulting a drift in the position of the object. This is corrected beforehand with cross-correlation and it is the same for all algorithms. After this registration procedure the images are processed by the PL, MLE, and the TIP algorithm using ≤ 10 iteration steps for

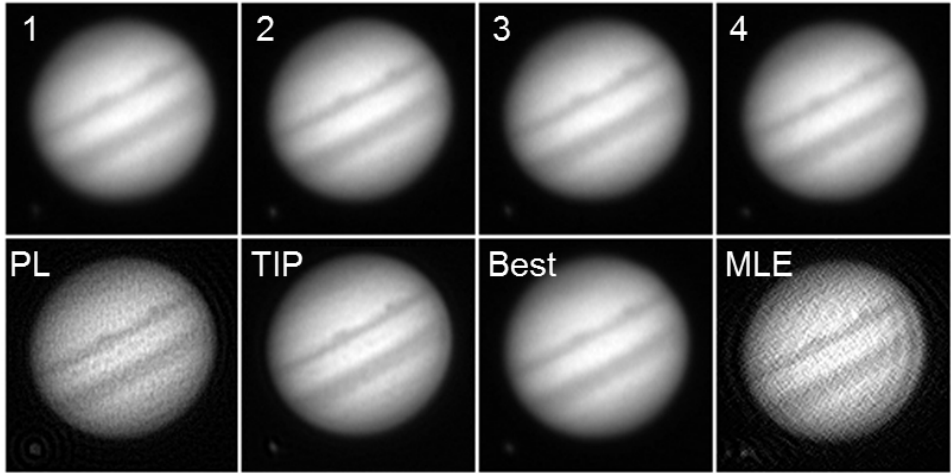


Figure 4.8: The performance of the algorithm on test images of Jupiter and its moon from a small amateur telescope. The top-row shows four frames from the acquisition; the bottom row shows the PL reconstruction, the TIP reconstruction, the best frame from the sequence, and the MLE reconstruction. The TIP algorithm performs better under these conditions than the other algorithms tested.

each. The results of the reconstructions are shown in Fig. 4.8 along with example frames from the sequence of images. A small region ($128 \times 128\text{px}$) of the original processed field-of-view ($512 \times 512\text{px}$) has been reproduced to allow the observation of the details. One common feature for all the algorithms is the amplification of the noise when processing images such as this. For this reason, the MLE algorithm was stopped once it started to diverge and produced worse estimates of the object. It is clear from this test that on this dataset the TIP algorithm performs better than the others and produces an improvement over the best or 'lucky' image of the sequence.

One concludes, the TIP framework produces the best results on this dataset, therefore, experimentally demonstrating the robustness of the algorithm to the sources of noise found in scientific imaging applications, that is those with low-light and low signal-to-noise ratios.

As a final rest, the results of the TIP algorithm is compared with MCD on experimental data. The dataset is acquired with a telescope through horizontal turbulence and is of a construction crane. Of this larger dataset, 16 frames are chosen when the object is severely distorted by the turbulence, but are sequential in time. One of the best images in the sequence is taken as a reference and is shown in Fig. 4.9. The first frame of the sequence is reproduced too along with the reconstructions for the MCD and the TIP algorithm. The algorithms are provided with the same *a priori* information, i.e. the PSF support is a box 9×9 pixels. The images have been apodized for the sake of the Fourier domain processing in both algorithms.

If one compares the results, the MCD solution is heavily filtered to suppress the effect of the noise in the images, it is clear that this involves information loss that has

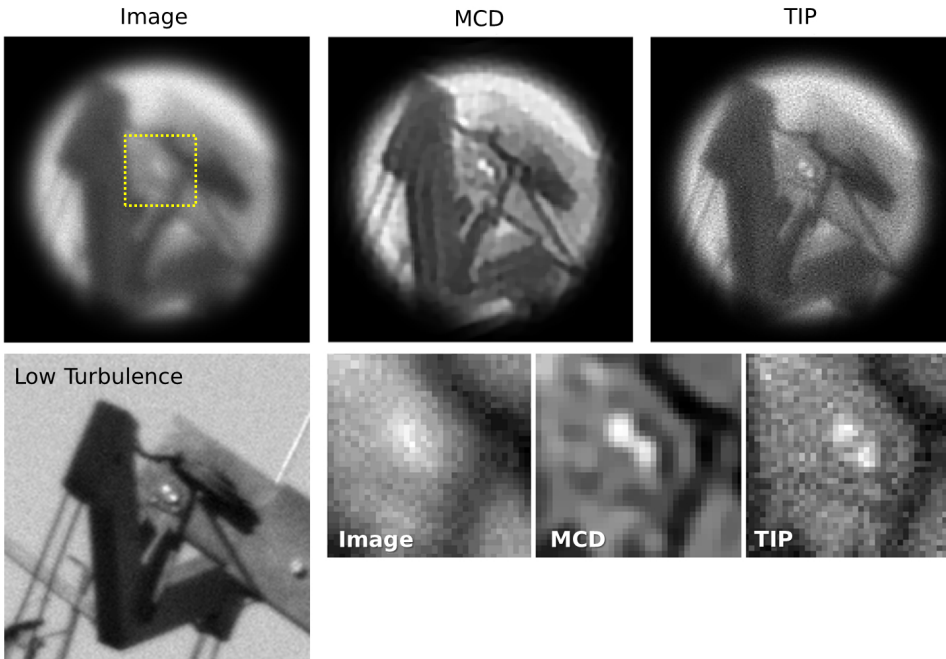


Figure 4.9: The performance of the algorithm on experimental images of a crane through horizontal turbulence. The top row shows the first image from the sequence of 16 frames with high turbulence, the middle the MCD solution and the right-hand side is the TIP solution. The second row shows a low turbulence frame, not included in the processing, and a zoomed region-of-interest outlined by the yellow box.

been restored in the TIP solution. The drawback of the TIP methodology is that there is a correlation with the noise, which may be reduced with more observation frames. The key result here is that features of the crane that are not visible in the unprocessed image sequence have been restored here, as can be seen with comparison with the low turbulence image.

4.5. Discussion

In this section, the motivation, limitations and strengths of the TIP algorithm will be explored and are provided as a contrast to the description given in Section 4.3. To begin, TIP does not yet fit into a mathematically neat and tidy framework; however, it is stressed that it is an ongoing piece of research to determine why the algorithm works as is observed in the experimental results. What can be discussed has been empirical discovered, but not yet rigorously proven mathematically.

TIP was designed to act as an alternative to adaptive optics in wide-field microscopic imaging. In this end application, near real-time deconvolution of the images is desired and one assumes that it possible to acquire more frames at will, but there is some cost associated with this. For this reason, TIP is designed to work on im-

ages of low signal-to-noise ratio extended objects, where the temporal dynamics of the medium are much faster than the object's and where an upper bound on the size of the PSF can be estimated. Furthermore, the PSF distortion is assumed to be caused by the presence of non-uniform media. TIP was not designed to treat motion blur, for example, and will not work when there are large displacements of the object. In fact for optimal performance, images should be pre-registered before processing with TIP.

The application gives rise to two *a priori* that have been used in TIP. Firstly, one can be reasonably certain that most of the energy of the PSF is contained within a small region determined by the optics and the phase aberration statistics. The residual outside this region can be safely regarded as having a negligible effect on the final image. This is a highly advantageous *a priori* as it reduces the number of unknowns within the optimisation problem dramatically. Secondly, the temporal dynamics is assumed to be non-existent under the period of acquisition, this is justifiable since the frame rate of cameras can run much faster than many dynamical process found in nature.

What these two *a priori* assumptions correspond to mathematically is a constraint of finite support on both the object and the PSFs. The support for the object is along the temporal dimension and the support for the PSF is along the spatial dimension. The motivation for finite support has been physically justified above, however, in terms of signal processing this has an intrinsic problem that all finite-supported functions are not bandlimited, whereas in fact, the image and PSFs are bandlimited. In practice, one finds if the support is sufficient the PSF has decayed such that there is no hard edge and no ill-effect is observed.

The authors hope that the algorithm will be useful in other imaging modalities, where it has been impossible for the authors to currently test it on. The version of the algorithm used in the experiments in this chapter, both implemented in Matlab and Python, can be found with examples in Code 1 [26]. It may be noted that since the image spectra are produced from the images by discrete Fourier transforms (DFTs) zero-padding may be used to reduce any edge effects. Moreover, it is often helpful to apodise the images optically or computationally to further reduce these limited domain problems and the noise amplification at high spatial frequencies. Apodisation is spatial finite support for the object and arises from a consequence of the finite information content in an image without extra *a priori*.

To start addressing the limitations, the TIP algorithm is specifically and exclusively a multi-frame (MF) algorithm. It does not work with a single-frame (SF), that is the case of $N = 1$. The reason that it does not work is that it is design to work in situations where one has minimal *a priori* information. One provides only the PSF support information to the algorithm; this implies that all the other necessary information must be present in the multiple frames acquired. TIP cannot interpolate, extrapolate or supplement the information in the datasets due to external *a priori* provided by the user. This naturally imposes limitations on the performance of the algorithm, leading to datasets where the algorithm will not be successful in finding the correct $\{\hat{H}_n, \hat{O}\}$.

In Figure 4.10, it is demonstrated that the TIP algorithm, starting from a δ -function

PSF has no information to generate the true PSF, therefore, it remains as a δ -function. The output object is then the same as the input image, however, one observes when extending the dataset by three more frames to be MF, the algorithm is able to extract the object information better. It should be noted that this SF solution found, does satisfy the constraints but is not the correct solution.

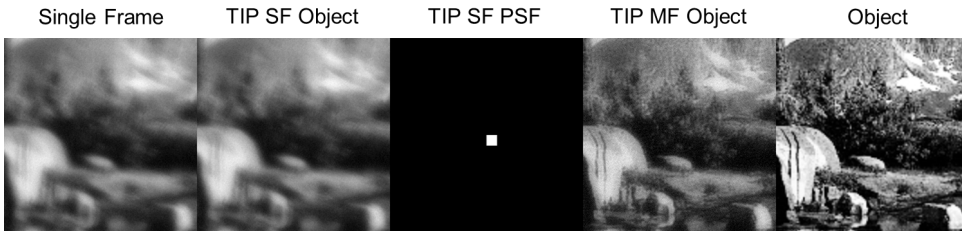


Figure 4.10: A demonstration that single-frame use of the TIP algorithm yields the trivial δ -function PSF due to lack of information in the dataset. Images have been cropped.

This is the first and primary limitation of the algorithm, $N > 1$. All the other limitations of the algorithm can be related to this first one, that is in the information content of the dataset. This condition may be formalised; for the algorithm to work optimally, the sum OTF spectrum must cover all frequencies within the bandlimit of the system and have no common zeros:

$$\sum_{n=1}^N |H_n(\vec{v}_m)| > 0 \quad \forall |\vec{v}_m| \leq v_{\max}, \quad (4.20)$$

where v_{\max} is the bandlimit of the signal. If these conditions are not met, the algorithm will not be able to separate the zeros of the OTFs from the zeros of object spectrum, resulting in a poor estimate of the object, as extra zeros in the spectrum correspond to missing information. In this case, more frames should be added to the dataset. The number of frames N required for this condition to be met is dependent on the PSF support size chosen, the temporal aberration statistics, and the signal-to-noise ratio. It is not easy to quantify this relationship, therefore, when used experimentally one can simply acquire more images until the information content is high enough to produce a good result. Although, it should be noted that if there is a static component of the aberration, not removed by the temporal dynamics, then TIP can never remove this static component.

Another case where the algorithm will not perform well is with sparse images, an example of this is stellar images. Here one is looking at point sources of differing intensity. Due to the simplicity of the object spectrum, the TIP algorithm struggles under these conditions to separate the zeros between the spectra. To demonstrate this, a comparison is made with some data found on the IDAC website [27]. The bandwidth of the object is much greater than the OTF bandwidth and TIP cannot restore this information in the manner of some other deconvolution algorithms such as

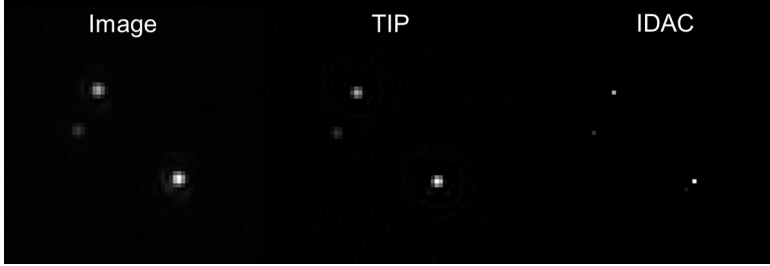


Figure 4.11: An example deconvolution problem where the TIP algorithm does not perform better than another algorithm IDAC. This stellar deconvolution problem of 9 frames from [27] cannot be reduced to δ -functions with the TIP algorithm.

4

IDAC. This leads us to another limitation of the TIP algorithm, the following condition must be met:

$$\|\{H_m(\vec{v}_m)\} \geq \epsilon > 0\| \gg \|\{O(\vec{v}_m)\} \geq \epsilon > 0\|, \quad (4.21)$$

where ϵ is some small threshold applied to the spectra. Another limitation this implies is that TIP cannot super-resolve features beyond the optical systems bandlimit as the OTF is zero in this region.

Many of the strengths of TIP have been discussed throughout the chapter and what is placed here will serve as a clarifier of important points. Firstly, the quality of the solution, in a PSNR sense, produced by the TIP algorithm mainly arises from lack of noise amplification due to the choice of \mathcal{P}_3 and \mathcal{P}_4 projections — this is the “tangential projection.” The reason for this robustness to noise arises since the algorithm in its operation indirectly filters the noise by reduction of its normal component. In this sense, the reconstructed images $\hat{O}\hat{H}_n$ produced from this pair of \hat{O} and \hat{H}_n with the aforementioned mutual fidelity can be seen as de-noised versions of the input images I_n , reconstructed with the minimum possible *a priori* knowledge. They could be used further as an input for any other algorithm making use of other *a priori* information. There is no process that can remove the tangential component without further *a priori* about the noise.

Secondly, TIP’s operations are simple and fast. Both in the sense of requiring ≈ 10 iterations before producing a usable estimate; but also in the number of floating point operations required. For example, on a sufficiently small number of pixels it is possible to run this algorithm for real-time image acquisition. The unoptimised Python or MATLAB implementation used to generate the figures in this chapter processed at an average speed of $2.2 \times 10^{-7} MNK$ seconds, *i.e.* per pixel per iteration — for example $2.2 \times 10^{-7} \times 256 \times 256 \times 4 \times 10 = 0.58$ seconds. Even with larger images, the speed may be greatly increased if only a sub-section of the image is used to identify the PSFs before deconvolving the whole dataset using the identified optimal linear filter; this possibility depends on the SNR.

Finally, whilst the convergence of the algorithm has not yet been proved, the TIP algorithm is not seen to diverge empirically in the majority of cases tested. This

has been attested to by the measurements that have been made in this chapter, see Section 4.4.3. The solution is stable under a high number of iterations (up to a 1000 have been tested) or the addition of more input frames, which for TIP only serves to increase the quality of the reconstruction by boosting the overall SNR.

To conclude, in this chapter the TIP algorithm has been presented as a multi-frame blind deconvolution algorithm that uses minimal *a priori* information. It has been found to have several key advantages when compared with other algorithms under these conditions and this comes in the form of: the quality of final solution (Section 4.4.4), its robustness to noise (Section 4.4.4), and its real-world applicability (Section 4.4.4).

This technique is, however, not perfect and improvements are possible, especially, with regard to the final image reconstruction once the point spread functions have been elucidated. Whilst the process of tangential projections provides the optimum point-spread functions these can still be effected by the tangential noise component, therefore, it would be possible to find a better non-blind deconvolution method than that is currently used in the algorithm. This would remove or at least reduce the correlation with the noise that is still sometimes present in the final reconstruction, this may be seen in Fig. 4.8 and Fig. 4.9.

The authors hope that further research will yield a satisfying mathematical proof of the operation and convergence of the algorithm to augment this chapter's empirical results along with further experimental validation of this technique for the correction of phase aberrations in scientific imaging applications.

References

- [1] D. Wilding, O. Soloviev, P. Pozzi, G. Vdovin, and M. Verhaegen, *Blind multi-frame deconvolution by tangential iterative projections (tip)*, *Optics Express* **25**, 32305 (2017).
- [2] R. W. Gerchberg and W. O. Saxton, *A practical algorithm for the determination of phase from image and diffraction plane pictures*, *Optik* **35**, 237–246 (1972).
- [3] J. R. Fienup, *Phase retrieval algorithms: a comparison*, *Applied optics* **21**, 2758 (1982).
- [4] R. A. Gonsalves, *Phase retrieval and diversity in adaptive optics*, *Optical Engineering* **21**, 215829 (1982).
- [5] R. G. Paxman, T. J. Schulz, and J. R. Fienup, *Joint estimation of object and aberrations by using phase diversity*, *JOSA A* **9**, 1072 (1992).
- [6] G. Ayers and J. C. Dainty, *Iterative blind deconvolution method and its applications*, *Optics letters* **13**, 547 (1988).
- [7] T. J. Schulz, *Multiframe blind deconvolution of astronomical images*, *JOSA A* **10**, 1064 (1993).

- [8] L. P. Yaroslavsky and H. J. Caulfield, *Deconvolution of multiple images of the same object*, *Applied Optics* **33**, 2157 (1994).
- [9] T. Zhang, H. Hong, and J. Shen, *Restoration algorithms for turbulence-degraded images based on optimized estimation of discrete values of overall point spread functions*, *Optical Engineering* **44**, 017005 (2005).
- [10] C. R. Vogel, T. Chan, and R. Plemmons, *Fast algorithms for phase diversity-based blind deconvolution*, *Adaptive Optical System Technologies* **3353**, 994 (1998).
- [11] D. Turaga and T. E. Holy, *Image-based calibration of a deformable mirror in wide-field microscopy*, *Applied optics* **49**, 2030 (2010).
- [12] P. M. Johnson, M. E. Goda, and V. L. Gamiz, *Multiframe phase-diversity algorithm for active imaging*, *JOSA A* **24**, 1894 (2007).
- [13] N. Wiener, *Extrapolation, interpolation, and smoothing of stationary time series*, Vol. 7 (MIT press Cambridge, MA, 1949).
- [14] P. Jansson, *Deconvolution of Images and Spectra* (Academic Press, 1997).
- [15] J. Idier, ed., *Bayesian approach to inverse problems* (Wiley, 2008).
- [16] V. Katkovnik, D. Paliy, K. Egiazarian, and J. Astola, *Frequency domain blind deconvolution in multiframe imaging using anisotropic spatially-adaptive denoising*, in *Signal Processing Conference, 2006 14th European* (IEEE, 2006) pp. 1–5.
- [17] F. Sroubek and P. Milanfar, *Robust multichannel blind deconvolution via fast alternating minimization*, *IEEE Transactions on Image Processing* **21**, 1687 (2012).
- [18] S. Chaudhuri, R. Velmurugan, and R. Rameshan, *Blind deconvolution methods: A review*, in *Blind Image Deconvolution* (Springer, 2014) pp. 37–60.
- [19] H. H. Bauschke, P. L. Combettes, and D. R. Luke, *Phase retrieval, error reduction algorithm, and fienup variants: a view from convex optimization*, *JOSA A* **19**, 1334 (2002).
- [20] D. R. Luke, *Finding best approximation pairs relative to a convex and prox-regular set in a hilbert space*, *SIAM Journal on Optimization* **19**, 714 (2008).
- [21] G. Li, C. Wen, and A. Zhang, *Fixed point iteration in identifying bilinear models*, *Systems & Control Letters* **83**, 28 (2015).
- [22] T. F. Chan and C.-K. Wong, *Convergence of the alternating minimization algorithm for blind deconvolution*, *Linear Algebra and its Applications* **316**, 259 (2000).

- [23] A. Pakhomov and K. Losin, *Processing of short sets of bright speckle images distorted by the turbulent earth's atmosphere*, Optics Communications **125**, 5 (1996).
- [24] M. Loktev, G. Vdovin, O. Soloviev, and S. Savenko, *Experiments on speckle imaging using projection methods*, in *SPIE Optical Engineering+ Applications*, edited by J. J. Dolne, T. J. Karr, V. L. Gamiz, S. Rogers, and D. P. Casasent (International Society for Optics and Photonics, 2011) pp. 81650M–81650M–10.
- [25] M. Loktev, O. Soloviev, S. Savenko, and G. Vdovin, *Speckle imaging through turbulent atmosphere based on adaptable pupil segmentation*, Optics letters **36**, 2656 (2011).
- [26] D. Wilding, O. Soloviev, P. Pozzi, G. Vdovin, and M. Verhaegen, *Iterative Projections (TIP) Source Code*, <https://osapublishing.figshare.com/s/d4afb41640ffb9904f55> (2017), [Online; accessed 07-August-2017].
- [27] J. Christou and K. Hege, *Iterative Deconvolution Algorithm in C (IDAC)*, <http://cfao.ucolick.org/software/idac/> (2000), [Online; accessed 07-August-2017].



5

Correcting the Image Part Two

*I can see clearly now, the rain is gone,
I can see all obstacles in my way
Gone are the dark clouds that had me blind
It's gonna be a bright, bright sun-shiny day.*

Johnny Nash

Chapter Abstract

Three-dimensional microscopy suffers from sample-induced aberrations, that reduce the resolution and lead to misinterpretations of the object distribution. In this chapter, the resolution of a three-dimensional fluorescent microscope is significantly improved, by introducing an amplitude diversity, in the form of a binary amplitude mask, positioned in several different orientations within the pupil, followed by computer processing of the diversity images. The method has proved to be fast, easy to implement and cost-effective in high-resolution imaging of *casper fli:GFP* zebrafish.

This chapter has been published in *Pupil mask diversity for image correction in microscopy*, Opt. Express **26**, 12 (2018) [1]

5.1. Introduction

Imaging fluorophores inside large three-dimensional samples with sub-cellular resolution is of a great interest in life sciences, however the inherent optical inhomogeneity of biological tissues distorts the image. Aberrations, arising from spatially variant phase delays throughout the sample, reduce the image contrast and scramble both the excitation and the fluorescent light, resulting in images that misrepresent the real fluorophore distribution.

These misrepresentations, in the fluorescent imaging arm, may be corrected only by first elucidating the error and then either by physically compensating for the phase delay using adaptive optics (AO) [2] or by computationally reconstructing the distribution, known as deconvolution [3].

Whilst light-sheet fluorescence microscopy (LSFM) [4, 5] is a technique that has been specifically developed for imaging large three-dimensional samples, the aberrations, scattering and absorption only generally allow for the use of lower numerical apertures (NA) that dampen the effect of aberrations at the cost of resolution. Despite this, sample-induced fallaciousness is present in unprocessed LSFM image stacks and researchers tend to acquire a number of datasets from different “views” and computationally merge them together [6]. To further improve the image quality these datasets may also be deconvolved with the measured system point-spread functions (PSFs) [7].

Adaptive optics (AO) has been employed more recently to correct for these aberrations in both detection [8] and excitation in Chapter 3, where it proceeds by a process of wavefront sensing and correction. In microscopy specifically, there has been two methodologies proposed for the sensing of aberrations. The first directs light to a sensor, such as a Shack-Hartmann sensor [9]. This approach requires the use of a “guide star” [10] and is better suited to scanning techniques rather than wide-field. The second method is an indirect measurement via the optimisation of the image quality and is preferred in wide-field imaging because using a wavefront sensor on an extended source is problematic.

Image optimisation requires the quantification of image quality in the form a metric. The choice of such a metric in wide-field microscopy is problematic and often sample and technique dependent. The optimisation of the adaptive optical element’s (AOE) control inputs, therefore, does not always lead to the image with optimal fidelity to the fluorophore distribution. The reasons for this is that in these microscopes the light source is never truly confined to a single-plane and the aberration is spatially variant.

These two points imply that the light received at the camera is a superposition of light from different regions within three-dimensional sample that would require different control inputs to correct them. As a result, it would take at least $N + 1$ frames [11] where N is the number of degrees of freedom of the AOE, to compensate the image in a single region of the sample with a specific aberration. In the lingo of AO these regions are called *isoplanatic patches*.

Given the effect of photo-bleaching and photo-toxicity, it is often better to perform deconvolution on such wide-field images to provide a better estimation of the object

when the point spread function (PSF) is known even approximately. In the presence of unknown aberrations, however, the PSF is unknown and deconvolution with the incorrect PSF will result in a poorly estimated object and unintended artefacts. A *blind* single-frame deconvolution [12] is an ill-conditioned mathematical problem with multiple solutions and therefore, cannot be done reliably in the presence of unknown aberrations without substantial *a priori* information. As a result, deconvolving an LSFM image stacks with a measured system PSF will not yield the true fluorophore distribution because of the presence of aberrations.

In order to deconvolve in complex three-dimensional samples correctly, with aberrations, it is necessary to either: (1) correctly identify the point-spread function by using diversity — this produces a multi-frame blind deconvolution problem [13] that is better conditioned and solutions can be more reliably found via a plethora of bilinear optimization algorithms [14]; (2) or correct for the aberrations using adaptive optics such that the PSF is known to be a diffraction-limited Airy pattern before deconvolving.

In this chapter, we develop an extremely simple and efficient implementation of the first method. By combining physical perturbation of the optical system, done by a rotating amplitude mask, alongside the computational processing of the resultant images, an image stack is corrected for sample-induced aberrations. To the authors' knowledge, whilst phase diversity has been used for astronomy [15], horizontal imaging [16], ophthalmic imaging [17], to calibrate deformable mirrors [18], and with amplitude diversity in the wavefront sensing [19]; there has been no successful attempt to apply this general sort of diversity in microscopy. The reasons for this may be that it has been difficult to identify the point-spread functions and obtain a well-conditioned deconvolution without noise-amplification at low signal-to-noise ratios (SNR).

An outline of the chapter: first an overview of the theory is given, then the description of the experimental methodology, the results from multiple *casper fli:GFP* zebrafish imaging experiments and to end a short discussion of the approach.

5.2. Methodology for Aberration Correction

An understanding of the technique may be derived from elementary imaging theory. In an adaptive optics system with control inputs x , the relationship between the formed image $i(x)$ and the pupil function $P(x) = A(x) \exp(j\phi(x))$, where $A(x)$ is the aperture's amplitude function and $\phi(x)$ its phase function, may be modelled by the following convolution operation:

$$i(x) = |\mathcal{F}\{P(x)\}|^2 * o + w, \quad (5.1)$$

where w is the noise and o is the unknown fluorophore distribution. Normally, the goal in AO is to find x^* such that one has $i(x^*) = |\mathcal{F}\{A(x^*)\}|^2 * o$ — the diffraction-limited image. From an imaging point of view, it may be noted that x^* itself is not important, but instead the fluorophore distribution o . It is possible to find an estimate of o without finding x^* by solving a mathematical optimisation problem. For control inputs x , the following problem may be posed:

$$\min_{h(x), o} \|i(x) - h(x) * o\|_2, \quad (5.2)$$

where only $i(x)$ is known and $h(x) = |\mathcal{F}\{P(x)\}|^2$. This is a many-to-one problem since there are many $h(x)$ and o that may produce the same $i(x)$. Its inverse is an ill-posed problem; however, if enough is known *a priori* one can solve this problem and crucially in an AO system one can acquire images with different x , adding diversity and therefore, reducing the number of solutions that satisfy the equation.

To understand why this is necessary, one must consider that in the presence of aberrations, the OTF $H(x) = \mathcal{F}^{-1}\{h(x)\}$ has points which are heavily modulated, implying that the system no longer transmits a set of spatial frequencies $\{\nu_\varphi\}$. In this case, $I(x) = \mathcal{F}^{-1}\{i(x)\}$ contains no information about the object $O = \mathcal{F}^{-1}\{o\}$ at these frequencies and no computational process can hereby restore this information. Furthermore, all image registration processes have additive noise both due to the sensor and the quantum nature of light, which is clearly prevalent in low light applications such as fluorescence microscopy. The image spectrum $I(x)$ may then be regarded as the sum of the true image spectrum $I_r(x)$ and the noise spectrum $W = \mathcal{F}^{-1}\{w\}$:

$$O = \frac{I_r(x) + W}{H(x)}, \quad (5.3)$$

in these spectral regions, destructive noise-amplification occurs as can be seen by:

$$|H(\nu_\varphi)| \rightarrow 0 \Rightarrow |O(\nu_\varphi)| \rightarrow \left| \frac{0 + W}{0} \right| = \infty. \quad (5.4)$$

Clearly, very large or infinite frequency components are non-physical and come from the inverse relationship — by adding the perturbations to the aperture one may move these zeros and extra information about the object may be included in the estimate by using multiple diverse observations.

In the notation the x shall be dropped and a subscript m used to denote a frame acquired under a different x value. The process begins by acquiring the first frame I_1 , which also becomes the first estimate for the object $\hat{O}^{(1)}$. For all subsequent frames acquired within the iterative loop, the k^{th} step for the m^{th} image, where $1 \leq m \leq k$, the Fourier relationship is:

$$I_m = \hat{H}_m^{(k)} \cdot \hat{O}^{(k)} + W_m, \quad (5.5)$$

The estimate of the OTFs $\hat{H}_m^{(k)}$ are updated using the previous estimate for the object spectrum $\hat{O}^{(k-1)}$:

$$\hat{H}_m^{(k)} = \mathcal{P}_{\mathcal{H}} \left\{ \frac{I_m}{\hat{O}^{(k-1)}} \right\}, \quad (5.6)$$

where $\mathcal{P}_{\mathcal{H}}$ is a projection operator onto the space of real-valued non-negative PSFs of a particular spatial extent. With this new estimate of the OTFs an estimate for the object spectrum may be obtained by back-projection using a window of the last n measurements:

$$\hat{O}^{(k)} = \alpha \mathcal{P}_{\mathcal{O}} \left\{ \overbrace{\frac{\sum_{m=k-n}^k I_m \times \bar{\hat{H}}_m^{(k)}}{\sum_{m=k-n}^k |\hat{H}_m^{(k)}|^2}}^{\hat{O}^{(k)}} \right\} + (1 - \alpha) \hat{O}^{(k-1)}, \quad (5.7)$$

where $0 < \alpha < 1$ is a feedback parameter. The PSF and thus the image is perturbed in the next step and this allows the algorithm to begin with a realistic starting point for O and H . The choice of Eq. (5.7) and Eq. (5.6) are due to noise propagation and discussion of the particular form of operators \mathcal{P}_H and \mathcal{P}_O are but may be found in Chapter 4. The form of the algorithm has been altered from Chapter 4 to run recursively on new data, hereby, it has been called the recursive Tangential Iterative Projections (rTIP) algorithm in this use. For this reason a more systematic representation has been given in Table 5.1. Here the steps of the algorithm along with concise descriptions have been recorded.

The feedback parameter's function in Eq. 5.7 is to bias the solution towards the new estimate ($\alpha > 0.5$) or the previous one ($\alpha < 0.5$). Depending on the window size, one may be more certain of the previous solution, based on many frames, than the new one based on only a couple of measurements. It need not be static, as shown in Step 5 in the Table 5.1, where α is a measure of the average relative difference between the new initial estimate $\tilde{O}^{(k)}$ and the last $\hat{O}^{(k-1)}$. This term provides a penalty for new estimates that differ from the previous ones and slows down the process of aberration correction, but reduces noise amplification.

Table 5.1: Steps of the rTIP algorithm with their descriptions in schematic form. After the second acquisition the steps 1 to 5 are repeated with every subsequent acquisition to update the object estimate $\hat{O}^{(k)}$.

Step/Projection	Process	Description
Startup 1	$\hat{O}^{(1)} = I_1$	First Frame
Startup 2	$\hat{O}^{(2)} = \sum_{m=1}^2 I_m/2$	Average
Step 1	$\tilde{H}_m^{(k)} = \frac{I_m}{\hat{O}_n^{(k-1)}}$ for $n - W \leq m \leq N$	Single-frame linear deconvolution
Step 2	$\hat{h}_m^{(k)} = \mathcal{F}\{\tilde{H}_m^{(k)}\}$ $\tilde{h}_m^{(k)}(\mathbf{x}) = 0$ if $\mathbf{x} \notin \mathbb{X}$ $\tilde{h}_m^{(k)} = 0$ if $\hat{h}_m < 0$ $\sum \tilde{h}_m^{(k)} = 1$ $\hat{H}_m^{(k)} = \mathcal{F}^{-1}\{\tilde{h}_m^{(k)}\}$	Fourier Transform Finite Support Constraint Non-negativity Threshold Normalisation Inverse Fourier Transform
Step 3	$\tilde{O}^{(k)} = \frac{\sum_{m=n-W}^n \tilde{H}_m I_m}{\sum_{m=n-W}^n \tilde{H}_m ^2}$	Multi-frame linear deconvolution
Step 4	$\tilde{o}^{(k)} = \mathcal{F}\{\tilde{O}^{(k)}\}$ $\tilde{o}^{(k)} = 0$ if $\tilde{o}^{(k)} < 0$ $\sum \tilde{o}^{(k)} = 1$ $\tilde{O}^{(k)} = \mathcal{F}^{-1}\{\tilde{o}^{(k)}\}$	Fourier Transform Non-negativity Threshold Normalisation Inverse Fourier Transform
Step 5	$\alpha = 1 - \frac{\sum \tilde{O}^{(k)} - \hat{O}^{(k-1)} }{\sum \tilde{O}^{(k-1)} }$ $\hat{O}^{(k)} = \alpha \tilde{O}^{(k)} + (1 - \alpha) \hat{O}^{(k-1)}$	Feedback Parameter Feedback Step

5.3. Experimental Design

A light-sheet fluorescence microscope has been realized in the configuration shown in Fig. 5.1, the excitation light is provided by a 488nm laser (100mW Sapphire LP, Coherent Inc., U.S.) and polarization optics (WPH10M-488 and GT5-A, Thorlabs, U.S.) to produce linearly polarized light for the spatial light modulator (SLM) (512x512, Meadowlark Optics, U.S.). The beam of the laser is split to multiple setups and therefore, is run giving 9mW into the LSFM microscope path, where with the efficiency of the SLM due to the grating width gives around 1mW at the back aperture of the objective.

The SLM is conjugated to the back aperture of an NA= 0.3 objective lens (UMPLFLN 10x Olympus, Japan) via a beam expander (AC508-200-A-ML and AC508-200-A-ML, Thorlabs, U.S.). The light-sheet is formed by using a cylindrical lens pattern applied to the SLM that reduces the focal power of the objective in one direction. Orthogonal detection of the fluorescence light is done with a NA= 0.5 imaging objective (UMPLFLN 20x Olympus, Japan), via the rotating actuator (PRM1/MZ8/TDC001, Thorlabs, U.S.) close to the back aperture with a 3D printed acrylonitrile butadiene styrene (ABS) double-wedge (Fig. 5.2(d), Ultimaker 3, the Netherlands) through a tube lens (AC254-200-A-ML, Thorlabs, U.S.) onto the imaging camera (Orca Flash v2, Hamamatsu Photonics, Japan) with a emission fluorescence filter (MF525-39, Thorlabs, U.S.).

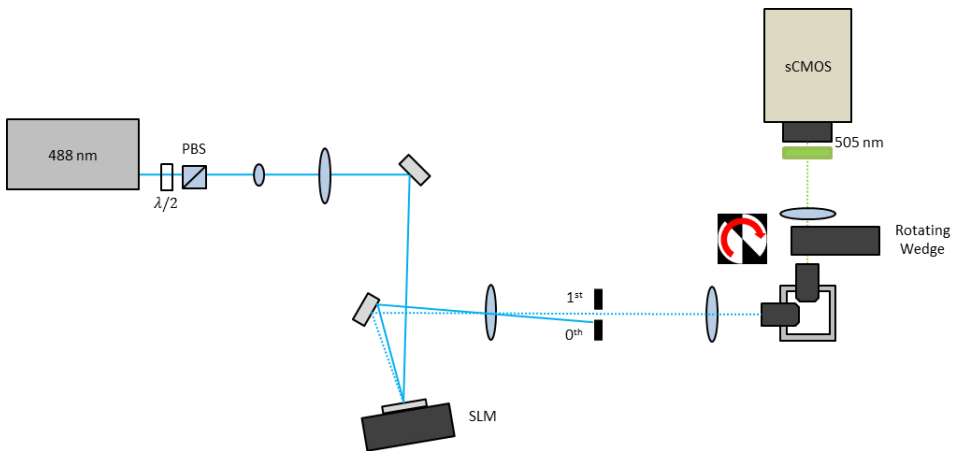


Figure 5.1: The experimental setup used for the imaging. The incident light path has an SLM for the excitation beam shaping and in the detection path a rotating pupil mask is placed close to the back aperture of the objective.

To design the pupil mask simulations of many different types of pupil masks were tried from random binary masks to spirals and wedges. The wedge design was chosen for its following properties: it was easy to manufacture and mount; in a 360° rotation of the mask all parts of the pupil would be transmitted; the diversity added by the mask empirically seemed to satisfy the condition of recovering lost frequencies

$\sum_m H_m(\nu_\varphi) > 0$; and it was easy to change the diversity added by adjustment of the wedge angle. In this way, a set of wedges with different angles were produced and tested experimentally. The wedge with the best performance for a particular set of imaging conditions could then be chosen.

A wedge angle of 45° was found to be the best pupil mask, balancing between diversity generated and light loss. The sample used was a para-formaldehyde fixed *casper fli:GFP* zebrafish (*danio rerio*) mounted in 0.5% agarose in a 1×1 mm square capillary tube (Vitrotubes™, VitroCom, U.S.) aligned with the LSFM axes. Three-dimensional acquisition is done by moving the sample through the light-sheet with a servo-motor stage (USB Stage, Picard Industries, U.S.) followed by post-processing registration to adjust for any sample drift.

5.4. Imaging Results

A $N = 8$ acquisition proceeds by acquiring a single z-stack, rotating the wedge 45° and then acquiring the next stack until the wedge has been rotated through the entire 360° range. With a perfect double-wedge there would be degeneracy in the dataset, however, this is not the case with the design used due to imperfections in manufacturing and lack of perfect centring on the pupil around ± 1 mm. The resulting images at each z position have 8 frames with different diversities. These may be processed sequentially after three-dimensional registration using the methodology described in Section 5.2 and a resultant series of estimates based on increasing the number of frames may be yielded. Approximations of the aperture shapes used for each of the images is shown by Fig. 5.2(c).

By taking one of the planes (at $z = 75 \mu\text{m}$ depth) the restoration process can be demonstrated in Fig. 5.2(a), where the frames of the dataset, *i.e.* normal frames from the microscope are compared with the successive fluorophore estimates. In this figure a 256×128 px region-of-interest (ROI) of the original 2048×2048 px images is shown. It can be observed that the reconstruction sharpness and contrast improves with increasing number of frames, but not with the raw images.

A 360×198 px ROI at $z = 135 \mu\text{m}$ depth from the dataset without the mask is also shown in Fig. 5.2(b), where it can be seen that the introduction of the mask does, as expected, lead to a loss in image quality through loss in signal in the first masked frame, however, by continuing the acquisition process a better result is yielded. This improvement can be more clearly seen by taking the line profile (LP) shown in Fig. 5.2(e). The LP is plotted for no mask, frame 1 and frame 8 of the iterative processing. This plot highlights the recovery of high spatial frequencies and image contrast between the first and the last frame, and the appearance of features lost by the optical aberrations in the original LSFM image shown by the red arrow.

The restoration process may then be repeated either plane-by-plane, in smaller ROIs to combat anisoplanatic aberrations, or as a full three-dimensional deconvolution. All of these methods will yield a final single three-dimensional dataset. Since the aberration is spatially variant in LSFM, the plane-by-plane method is preferred, allowing the aberration to change between each plane along the direction orthogonal to the

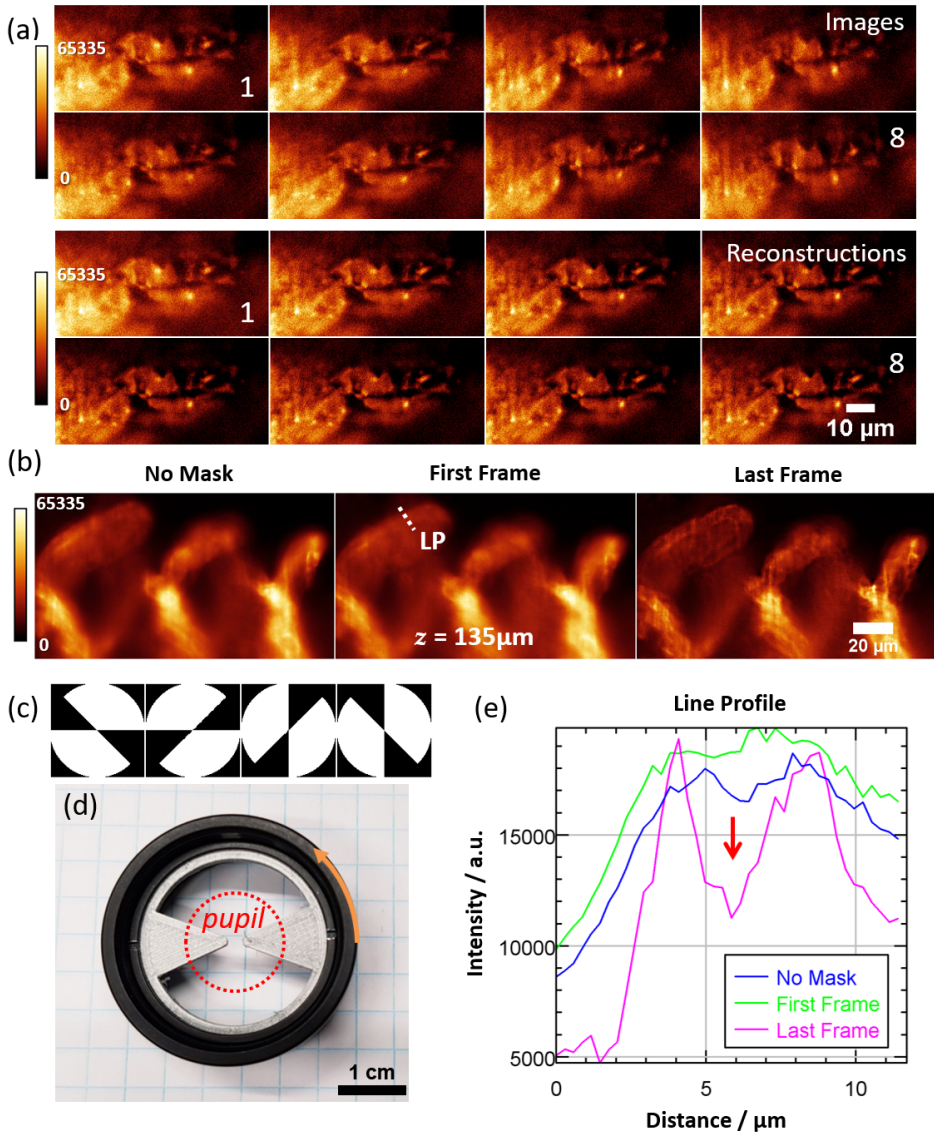


Figure 5.2: (a) the evolution of the image acquisition and reconstruction for a plane 75 μm inside the zebrafish (b) a ROI at plane 135 μm with no mask compared with the first object reconstruction and the last. (c) the wedge positions for images 1-4. (d) the experimental wedge with the pupil size overlaid. (e) the line profile labelled LP in (b). The red arrow shows a feature not present in the original LSFM image that is now clearly resolved. All images are normalised to a 16-bit range minimum to maximum with the colour-scale as shown.

plane. The PSF is expected to vary with depth z , but also with position across the light-sheet x , especially axially; therefore, xy processing and yz processing are tried.

The maximum intensity projection (MIP) of the unprocessed LSFM data and the processed set is shown in Fig. 5.3(a) showing the increased contrast of the processed datasets. Fig. 5.3(b) and (c) give an insight into the effect of the processing in the z -direction or the x -direction. It can be seen that the xy plane-by-plane processing does not improve the z -sectioning ability as expected, however, when processing the yz slices the axial resolution can be seen to be improved. This effect is most clearly seen in the line profile found in Fig. 5.3(c).

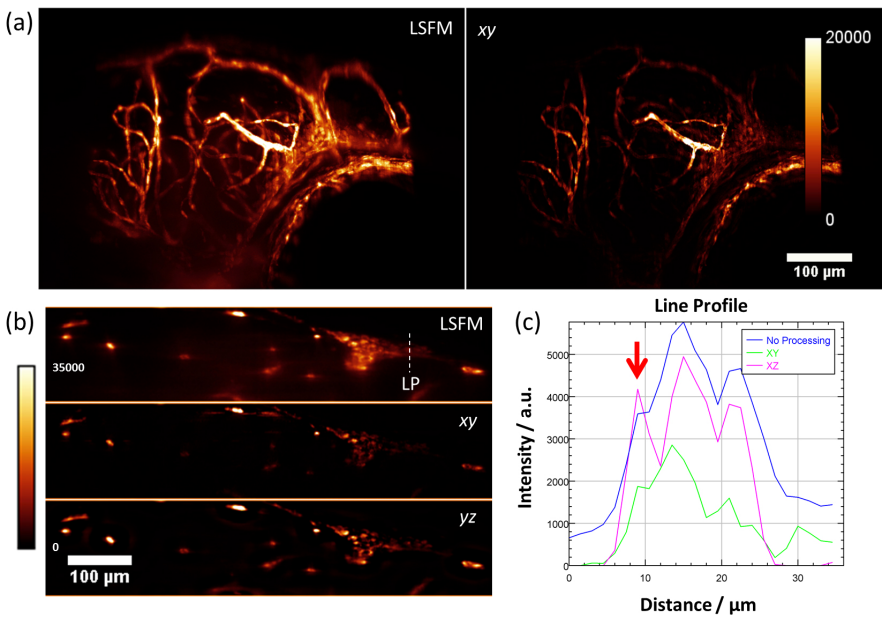


Figure 5.3: (a) A xy maximum intensity projection of the three-dimensional dataset of the zebrafish larvae head with the standard LSFM (8 datasets) and the diversity processed set plane-by-plane in the xy direction. (b) A slice through the zebrafish in the yz -plane showing the comparison between xy processing and yz processing. (c) A plot of the line profile in (b). All images are normalised to a 16-bit range minimum to maximum with the colour-scale as shown.

Through these experiment it is shown that by adding a simple AOE it is possible to improve the images from a LSFM. This occurs because the active modulation of the OTF removes the zeros in the summed image spectrum ensuring that the object information may be extracted algorithmically. Unwanted noise amplification does not occur due to both the combination of the physical and computational process used (Section 5.2).

5.5. Discussion

The benefits of this new approach may be summarised at this point: firstly, it is not necessary to determine what are the control settings that optimise the image, this means that the amount of expertise required to use adaptive optics well is reduced dramatically; secondly, the method requires less frames thus incurring less photo-bleaching and toxicity than would be required by model-free or model-based optimisation of the images with most devices used for microscopy. Thirdly, it is possible to go beyond the limitations of the AOE, therefore, cheaper and less technical devices may be used for the same effect. Finally, the technique finds the spatially variant PSFs from the data and therefore, takes into account sample-induced aberrations instead of just the system ones, reducing the probability of yielding a solution that misrepresents the fluorophore distribution.

This is not to state that this technique is perfect, since one of the benefits of physically optimizing the PSF is that it improves the signal-to-noise ratio (SNR) of the images. Aberrations through the loss of SNR alone can cause a dramatic reduction in image quality especially in non-linear imaging modalities. It is therefore, a valid criticism that reducing light collection efficiency is to be avoided. The reason for making the trade-off here is that diversity can restore the lost spatial frequencies and therefore, aberrations can be corrected.

Furthermore, the speed of the algorithm is linearly proportional to the number of pixels used. For CPU it can process at $2.5\mu\text{s}$ per pixel (Intel i7 8-core, 32 GB RAM), meaning for the datasets in this chapter of $(2048 \times 2048 \times 100)$ px \times 8 z-stacks, the total processing time is around 140 minutes. This is not an unreasonable for blind deconvolution on LSFM data, but slow for practical imaging. The problem has parallelism and the speed can be increased by an order of magnitude by processing on a GPU. For a single 2D plane of 8 images on the GPU (nVidia GTX980), it takes 6.9 seconds to have a corrected reconstruction, which is faster than performing image optimisation on the LSFM data in the author's experience.

The limitations to the correction depend on the signal-to-noise ratio and are difficult to quantify experimentally. Some numerical work has been on this question in Chapter 4. One can imagine the aberration as providing another source of noise in the imaging process. As a result, the aberration size, its order, the brightness of the fluorophores and quality of the detection system all combine to limit the total dynamic range of the correction. As an intuitive example, a bright sample would be able to be corrected at a higher aberration level than a dimmer sample if it had the same SNR.

It should be noted that this type of pupil mask is not the only possible option. A transmissive element, such as a pyramid, could also be used in the case where photons are too precious to lose by collecting all the light paths. Or if a phase element is used such as a deformable mirror, the technique may also be used in parallel with optimisation-based approaches to obtain the corrected image faster. To do this, however, it is preferred to use an optimisation algorithm that does not rely on a coordinate search since for best results one requires the root mean square phase diversity (r.m.s.) to be less than the r.m.s. phase aberration, such an algorithm may be found in Ver-

straete *et al.* [20]. In this hybrid-case, the bonus is that the physical Strehl ratio and thus the SNR ratio improves, which may be useful in low-light applications and on light-sensitive samples.

To conclude, in this chapter a new method for applying adaptive optics in the detection path of a wide-field microscope has been presented for the purpose of obtaining a more accurate representation of the fluorophore distribution. It relies on the principle of changing the aperture between stack or image acquisitions, hereby changing the PSF of an optical system so that it is possible to computationally extract the object distribution through bilinear optimisation. The technique provides a faster, more cost effective solution to the problem of aberration correction imaging in wide-field microscopy when compared with existing methods, however, it does suffer from some of the common drawbacks of computationally-based adaptive optics such as there is no physical increase in the signal-to-noise ratio and the scaling of the problem with image size.

References

- [1] D. Wilding, P. Pozzi, O. Soloviev, G. Vdovin, and M. Verhaegen, *Pupil mask diversity for image correction in microscopy*, *Opt. Express* **26**, 14832 (2018).
- [2] M. J. Booth, *Adaptive optical microscopy: the ongoing quest for a perfect image*, *Light: Science & Applications* **3**, e165 (2014).
- [3] J. G. McNally, T. Karpova, J. Cooper, and J. A. Conchello, *Three-dimensional imaging by deconvolution microscopy*, *Methods* **19**, 373 (1999).
- [4] A. Voie, D. Burns, and F. Spelman, *Orthogonal-plane fluorescence optical sectioning: Three-dimensional imaging of macroscopic biological specimens*, *Journal of microscopy* **170**, 229 (1993).
- [5] J. Huisken, J. Swoger, F. Del Bene, J. Wittbrodt, and E. H. Stelzer, *Optical sectioning deep inside live embryos by selective plane illumination microscopy*, *Science* **305**, 1007 (2004).
- [6] J. Swoger, P. Verveer, K. Greger, J. Huisken, and E. H. Stelzer, *Multi-view image fusion improves resolution in three-dimensional microscopy*, *Optics express* **15**, 8029 (2007).
- [7] P. J. Verveer, J. Swoger, F. Pampaloni, K. Greger, M. Marcello, and E. H. Stelzer, *High-resolution three-dimensional imaging of large specimens with light sheet-based microscopy*, *Nature methods* **4**, 311 (2007).
- [8] C. Bourgenot, C. D. Saunter, J. M. Taylor, J. M. Girkin, and G. D. Love, *3d adaptive optics in a light sheet microscope*, *Optics express* **20**, 13252 (2012).
- [9] B. C. Platt and R. Shack, *History and principles of shack-hartmann wavefront sensing*, *Journal of Refractive Surgery* **17**, S573 (2001).

- [10] X. Tao, B. Fernandez, O. Azucena, M. Fu, D. Garcia, Y. Zuo, D. C. Chen, and J. Kubby, *Adaptive optics confocal microscopy using direct wavefront sensing*, *Optics letters* **36**, 1062 (2011).
- [11] H. Yang, O. Soloviev, and M. Verhaegen, *Model-based wavefront sensorless adaptive optics system for large aberrations and extended objects*, *Optics express* **23**, 24587 (2015).
- [12] G. Ayers and J. C. Dainty, *Iterative blind deconvolution method and its applications*, *Optics letters* **13**, 547 (1988).
- [13] L. P. Yaroslavsky and H. J. Caulfield, *Deconvolution of multiple images of the same object*, *Applied Optics* **33**, 2157 (1994).
- [14] W. H. Press, S. A. Teukolsky, W. T. Vetterling, and B. P. Flannery, *Numerical Recipes 3rd Edition: The Art of Scientific Computing* (Cambridge University Press, 2007).
- [15] A. Pakhomov and K. Losin, *Processing of short sets of bright speckle images distorted by the turbulent earth's atmosphere*, *Optics Communications* **125**, 5 (1996).
- [16] M. Loktev, G. Vdovin, O. Soloviev, and S. Savenko, *Experiments on speckle imaging using projection methods*, in *SPIE Optical Engineering+ Applications*, edited by J. J. Dolne, T. J. Karr, V. L. Gamiz, S. Rogers, and D. P. Casasent (International Society for Optics and Photonics, 2011) pp. 81650M–81650M–10.
- [17] G. Chenegros, L. M. Mugnier, F. Lacombe, and M. Glanc, *3d phase diversity: a myopic deconvolution method for short-exposure images: application to retinal imaging*, *JOSA A* **24**, 1349 (2007).
- [18] D. Turaga and T. E. Holy, *Image-based calibration of a deformable mirror in wide-field microscopy*, *Applied optics* **49**, 2030 (2010).
- [19] V. Korkiakoski, C. U. Keller, N. Doelman, M. Kenworthy, G. Otten, and M. Verhaegen, *Fast & furious focal-plane wavefront sensing*, *Applied optics* **53**, 4565 (2014).
- [20] H. R. G. W. Verstraete, S. Wahls, J. Kalkman, and M. Verhaegen, *Model-based sensor-less wavefront aberration correction in optical coherence tomography*, *Optics Letters* (2015).

6

Conclusions & Future Outlook

This thesis has focused on novel methodologies for the correction and improvement of imaging in fluorescence microscopy. Specifically, the modality that has been used due to its wide-field optical sectioning ability is the light-sheet fluorescence microscope. As outlined in the introduction, this type of microscope allows for high-speed and high-resolution imaging inside of large three-dimensional samples.

Due to the inherent optical inhomogeneity of such samples, however, these images are distorted by aberrations on both the optical paths of this microscope. Moreover, the design of the system in this configuration is not optimal for imaging since the distribution of the excitation light is also physically inhomogeneous over the microscope's field-of-view.

To address these problems, this thesis has looked at three distinct improvements that can be made to this microscope. The first was the *Shaping of Illumination* that was covered in Chapter 2; the second improvement was the *Correcting the Illumination* in Chapter 3; and finally the fluorescence detection path was treated in *Correcting the Image* found in Chapters 4 & 5. Hereafter is a summary of accomplishments and the potential for future work.

Shaping the Illumination The purpose of this work focused on the fundamental properties of light that allowed the extension of the depth-of-focus in such away that the illumination became uniform over the lateral field-of-view of the microscope, which is orthogonal to the illumination path. The generation of this kind of shaped beam or light-sheet with a spatial-light modulator or a pupil phase mask is a simple and effective solution for researchers who wish to improve their average axial resolution over their field-of-view.

Over the course the thesis work, there has been developed a high complex optical system called the lattice light-sheet microscope [1] that aims to address the very same problem. The pupil filter methodology is simpler and more elegant solution and if used

with multi-photon excitation, as is an ongoing piece of research, could potentially have much smaller side-lobes and less out-of-focus excitation.

It has come to the attention of the author during the time of the thesis that development of this line of enquiry would be appreciated by the scientific community and therefore, suggestions for future work would be that this work be extended to imaging with a scanning system as well as the stationary light-sheet. The solutions provided can also be extended to produce longer beams for large fields of view. This work should also be combined with the correction of the light-sheet as outlined in the following section.

Correcting the Illumination It had always been clear that aberrations affected the shape of the incident excitation light and caused a spreading in the light-sheet from a diffraction-limited case. In the light-sheet microscope this causes a broadening and inhomogenisation of the illumination profile. In this case, the signal-to-noise ratio of the imaging goes down and the three-dimensional distribution of fluorescence is severely degraded as both out-of-focus light increases and the appearance of side-lobes affect the recorded fluorescence distribution.

To combat these problem a sensing system was implemented to find the aberration information contained in the epi-fluorescent light from the excitation path. This light that was normally not used in the imaging process could instead be used for the purpose of improving the images, this is a rare example in optics where something is gained at very little cost. Due to the type of adaptive optical element, however, it was not possible to apply feedback control on the illumination, which would be superior, but it was found that even a simple feedforward system was able to produce significant improvements in the imaging quality in the axial direction.

For directions of future work, this kind of *epi* adaptive optics system could be implemented using a deformable mirror instead of a spatial light modulator. This would give the possibility to do feedback control on the incident light allowing continuous correction of the light-sheet in different positions in the sample.

Alternatively, as sketched in the author's recent work [2], it has been shown how a sensor-less approach may be used to correct for aberrations in the light-sheet by encoding a spatial frequency into the fluorescence images. This has the potential when combined with the pupil filters to be an easy-to-use methodology for adaptive optics in light-sheet microscopy and may be worth further and fuller development.

Correcting the Image It was discovered during the research for this thesis that the methods available for the correction of images in wide-field microscopy were not suitable for application in biological imaging. The reason for this is that the modality of wide-field whilst allowing highly parallel acquisition, *i.e.* all pixels are acquired together, does this at the cost of allowing a great degree of cross-talk or blending between these pixels. In this sense, it is very hard for a computer to be able to distinguish what is a good image from a bad image.

On the other hand, an incoherent imaging system is well understood and modelled

by a straightforward convolution of a kernel and the object. What is not so straightforward is the inverse process because this involves inversion and is highly susceptible to noise artefacts. By combining multiple frames it is possible to remove this effect by converting it into a multi-frame deconvolution problem as can be done in astronomy.

In microscopy, the aberrations are not usually dynamic on a timescale that is critical for the adaptive optics system. It was possible then to use it to apply physical perturbations to the optical system to generate diversity. This diversity, either phase or amplitude, could be then used to identify the hidden aberration using a computer to perform the deconvolution.

The author developed a new algorithm, called TIP, for processing these images in a fast and timely way so that it could be done in parallel with the acquisition of the microscopy images and allowing the correction of aberrations in the sample in a fraction of the time that would usually be required for standard adaptive optics.

The correction, however, is computational and does not increase the signal-to-noise ratio of the acquired frames that would be of greater benefit to the user. The next steps in this research is to be able to acquire the phase distribution of the aberration and not simply the shape of the PSF. This requires the solving of an additional phase retrieval problem that can also be solved in the TIP framework [3]. This would allow the measurement of the wavefront in a couple of frames and allow for closed-loop feedback to reduce the aberration. It would not be as fast as using a wavefront sensor, but would allow it be retrieved from the images rather than through indirect optimisation.

Integration of Approaches The biggest piece of work for the future is the integration of all of these individual pieces of work into a whole. Whilst the approach of testing and experimenting with new approaches is best done by isolating these parts to avoid cross-talk and ambiguity, now that it has been shown that they individually function as expected; the next step is combine all of them together into a single technique. From this point of view, it is important to show that the whole is better than the sum of its parts, that by combining these individual elements it is possible to produce a far superior system than without integration.

A final point is, to do adaptive optics control properly one needs to “close the loop.” The sensors in the system need to be able to feedback to the actuators. In many of approaches that have been used in this thesis a method for feedback was not possible at the time. The correction of the illumination for example, could have included a mirror instead of an SLM, which would have allowed the effect of the correction to be sensed. On the other hand, if a sensor-less adaptive optics approach had been devised for the illumination or the fluorescence, then it would have been possible to continually adapt the adaptive optics to compensate for the aberrations. Thankfully, these approaches and directions of research are still possible to pioneer.

The End

References

- [1] B.-C. Chen, W. R. Legant, K. Wang, L. Shao, D. E. Milkie, M. W. Davidson, C. Janetopoulos, X. S. Wu, J. A. Hammer, Z. Liu, B. P. English, Y. Mimori-Kiyosue, D. P. Romero, A. T. Ritter, J. Lippincott-Schwartz, L. Fritz-Laylin, R. D. Mullins, D. M. Mitchell, J. N. Bembenek, A.-C. Reymann, R. Böhme, S. W. Grill, J. T. Wang, G. Seydoux, U. S. Tulu, D. P. Kiehart, and E. Betzig, *Lattice light-sheet microscopy: Imaging molecules to embryos at high spatiotemporal resolution*, *Science* **346** (2014), 10.1126/science.1257998, <http://science.sciencemag.org/content/346/6208/1257998.full.pdf> .
- [2] D. Wilding, P. Pozzi, O. Soloviev, G. Vdovin, R. Fiolka, and M. Verhaegen, *Hybrid adaptive and computational light-sheet fluorescence microscopy*, (2018) pp. 10502 – 10502 – 7.
- [3] D. Wilding, G. de longh, O. Soloviev, P. Pozzi, G. Vdovin, and M. Verhaegen, *Rapid identification of coherent pupil functions from multiple intensity measurements*, in *European Conference on Biomedical Optics* (Optical Society of America, 2017) p. 104160G.

Awards & Scholarships

2008	Churchill College Scholarship
2009	Churchill College Scholarship
2010	Churchill College Scholarship

Research Skills & Interests

Numerical Optimisation	Optical Design	Deconvolution
Adaptive Optics	Fluorescence Microscopy	Sample Preparation
Phase Diversity	Wavefront Sensing	Phase Retrieval
Python	MATLAB	C/C++
CUDA	Parallel Computing	Labview

Teaching Skills & Experience

2015 – 2016	MSc Thesis Supervision
Student:	Gijs de Jongh
Thesis:	<i>Identification and control of light propagation in optical waveguides</i>
2016 – 2017	MSc Thesis Supervision <i>cum laude</i>
Student:	Guillermo Arto Sanchez
Thesis:	<i>Online Computational Imaging Reconstruction</i>
2014 – 2018	Teaching Assistant
Courses:	<i>Control for High Resolution Imaging & Adaptive Optics Design Project</i>
	<ul style="list-style-type: none"> ◦ Setting and marking homework assignments ◦ Contributing to course and laboratory notes ◦ Giving seminars ◦ Teaching laboratories

Others Skills & Experience

Languages English (native), Dutch (intermediate)

Personal Information

Date of Birth	21-07-1988
Place of Birth	Wigan, United Kingdom.
Nationality	British

List of Publications

Below is a list of publications that have been compiled during the period of work on this thesis:

Journal Publications

1. *Pupil filters for extending the field-of-view in light-sheet microscopy*, **D Wilding**, P Pozzi, O Soloviev, G Vdovin, CJ Sheppard, M Verhaegen, *Optics letters* **41** (6), 1205-1208 11 (2016)
2. *Holographic imaging with a Shack-Hartmann wavefront sensor*, H Gong, O Soloviev, **D Wilding**, P Pozzi, M Verhaegen, G Vdovin, *Optics express* **24** (13), 13729-13737 5 (2016)
3. *Adaptive illumination based on direct wavefront sensing in a light-sheet fluorescence microscope*, **D Wilding**, P Pozzi, O Soloviev, G Vdovin, M Verhaegen, *Optics express* **24** (22), 24896-24906 4 (2016)
4. *High speed wavefront sensorless aberration correction in digital micromirror based confocal microscopy*, P Pozzi, **D Wilding**, O Soloviev, H Verstraete, L Bliet, G Vdovin, M Verhaegen, *Optics Express* **25** (2), 949-959 3 (2017)
5. *Blind multi-frame deconvolution by tangential iterative projections (TIP)*, **D Wilding**, O Soloviev, P Pozzi, G Vdovin, M Verhaegen, *Optics express* **25** (24) (2017)
6. *Optimal model-based sensorless adaptive optics for epifluorescence microscopy*, P Pozzi, O Soloviev, **D Wilding**, G Vdovin, M Verhaegen, *PLoS one* 13.3 (2018): e0194523.
7. *Pupil mask diversity for image correction in microscopy*, **D Wilding**, P Pozzi, O Soloviev, G Vdovin, M Verhaegen, *Opt. Express* **26** (12), 14832-14841 (2018)

Conference Publications

1. *Light-sheet optimization for microscopy*, **D Wilding**, P Pozzi, O Soloviev, G Vdovin, M Verhaegen, *Adaptive Optics and Wavefront Control for Biological Systems II* 9717 1 (2016)
2. *Adaptive optics in digital micromirror based confocal microscopy*, P Pozzi, **D Wilding**, O Soloviev, G Vdovin, M Verhaegen, *Proc. of SPIE Vol 9717, 971706-1* (2016)
3. *Rapid identification of coherent pupil functions from multiple intensity measurements*, **D Wilding**, G de Longh, O Soloviev, P Pozzi, G Vdovin, M Verhaegen, *European Conference on Biomedical Optics*, 104160G (2017)

4. *Phase diversity based object estimation in light-sheet fluorescence microscopy*, **D Wilding**, P Pozzi, O Soloviev, G Vdovin, M Verhaegen, Bio-Optics: Design and Application, BoTu2A. 2 (2017)
5. *Model based wavefront sensorless adaptive optics in confocal microscopy with reflective pinhole*, P Pozzi, **D Wilding**, O Soloviev, G Vdovin, M Verhaegen, Bio-Optics: Design and Application, BoTu2A. 3
6. *Hybrid adaptive and computational light-sheet fluorescence microscopy*, **D Wilding**, P Pozzi, O Soloviev, G Vdovin, R Fiolka, M Verhaegen, Proc. of SPIE 10502, Adaptive Optics and Wavefront Control for Biological Systems IV, 1050212 (2018)
7. *Practical guidelines for implementing adaptive optics in fluorescence microscopy*, **D Wilding**, P Pozzi, O Soloviev, G Vdovin, M Verhaegen, Proc. of SPIE 10502, Adaptive Optics and Wavefront Control for Biological Systems IV, 105021F (2018)
8. *Use of digital micromirror devices as dynamic pinhole arrays for adaptive confocal fluorescence microscopy*, P Pozzi, **D Wilding**, O Soloviev, G Vdovin, M Verhaegen, Proc. SPIE 10546, Emerging Digital Micromirror Device Based Systems and Applications X, 105460D (2018)
9. *Adaptive optics two-photon light-sheet microscopy*, **D Wilding**, R Fiolka, Frontiers of Microscopy (2018)